



University of Sussex

**A University of Sussex DPhil thesis**

Available online via Sussex Research Online:

<http://sro.sussex.ac.uk/>

This thesis is protected by copyright which belongs to the author.

This thesis cannot be reproduced or quoted extensively from without first obtaining permission in writing from the Author

The content must not be changed in any way or sold commercially in any format or medium without the formal permission of the Author

When referring to this work, full bibliographic details including the author, title, awarding institution and date of the thesis must be given

Please visit Sussex Research Online for more information and further details



# **Ion trap cavity system for strongly coupled cavity - QED**

**Elisabeth Christina Brama**

Submitted for the degree of Doctor of Philosophy

University of Sussex

September 2012

# Declaration

I hereby declare that this thesis has not been and will not be submitted in whole or in part to another University for the award of any other degree.

Signature:

Elisabeth Christina Brama

UNIVERSITY OF SUSSEX

ELISABETH CHRISTINA BRAMA, DOCTOR OF PHILOSOPHY

ION TRAP CAVITY SYSTEM FOR STRONGLY COUPLED CAVITY - QEDSUMMARY

The combination of an ion trap with a high finesse optical cavity is an ideal system for the investigation of strong coupling cavity quantum electrodynamics, and allows the observation of a number of interesting quantum phenomena. To achieve the small mode volumes required without impairing the ion trapping small traps with a short ion electrode distance are needed. Two microscopic linear rf ion traps have been developed and built to accommodate experimental cavities of lengths of several 100 microns.

The first trap design, the 'sandwich' trap, was successfully used to trap  $^{40}\text{Ca}^+$  - ions for several hours. It was characterised extensively including a measurement of the heating rates of the ions in the trap. Spectroscopy measurements of the cooling transition, as well as the two repumping transitions were carried out.

The second trap design, the 'alumina' trap, also successfully trapped  $^{40}\text{Ca}^+$  - ions, and a full characterisation of this trap was made. The experimental cavity was installed at a preliminary cavity length distance of 3.7 mm. The cavity characteristics were examined. Finally the trapped ions were overlapped with the cavity mode by adjusting the trap minimum position along the trap axis via dc voltages and the vertical position of the cavity.

To progress further a locking scheme for the cavity length as well as a single-photon detection setup are necessary. To achieve strong coupling a reduction of the cavity length will have to be made.

# Acknowledgements

Simply put this thesis would not have materialised without the help and support of many people. First of all I want to express gratitude to Wolfgang Lange for giving me the chance to work in his lab and to be part of such exciting research. I know for a fact that not everyone would have given me this chance, not least because it was never in question that I would spend a large amount of my energy pursuing the dream of racing the Hawaii Ironman triathlon. His unwavering support, patience, and help with what must have seemed simple questions to him still amazes me. It was deeply upsetting when Wolfgang died in early April this year. Not only was he a brilliant and enthusiastic physicist he also had a kind heart and an open ear for anyone. He was funny and outrageous and I doubt that anyone could have disliked him even if they tried. Thank you Wolfgang for the time we had with you, rest in peace!

My supervisor Matthias Keller was instrumental in guiding my work at every stage of the project. Without his help and wealth of knowledge this work would not have been possible. Much of the work covered in this thesis happened in collaboration with Anders Mortensen, who worked on the experiment with me for the first 2 years of my time within the group, and who was always quick to help progress things along with his experience and ideas. I also want to thank Nic Seymour-Smith, Alex Wilson, Dan Crick, Fedja Orucevic and Hiroki Takahashi for their assistance and many fruitful discussions.

A special mention has to go to my fellow PhD student Andrew Riley-Watson for being on the very same page as me when it came to once again being completely overwhelmed by physics and how seemingly everyone else 'got it' apart from us. 'Too stupid!' is a phrase I will not forget quickly.

Progress in our lab would have been much slower without the help of a very capable mechanics work shop, in particular John Knight and Alan Butler 'next' door who were always ready to help.

And finally I want to thank my parents, without whom I would not be the person I am today, and who made me believe in never giving up on my goals, and my friends, who have supported me throughout the last few years, and made it possible for me to continue in particular in the light of everything that life has thrown at me in the last 9 months.

# Contents

<b>List of Tables</b>	<b>viii</b>
<b>List of Figures</b>	<b>xii</b>
<b>Introduction</b>	<b>1</b>
<b>1 Ion Traps</b>	<b>4</b>
1.1 Introduction . . . . .	4
1.2 Ion Trap Theory . . . . .	4
1.3 Linear Paul Trap . . . . .	5
1.3.1 Ion Motion . . . . .	9
1.4 Pseudopotential Approximation . . . . .	11
1.4.1 Ion Motion within the Pseudopotential Approximation . . . . .	12
1.5 Non Ideal Trap . . . . .	13
1.5.1 Trap Efficiency and Anharmonicity . . . . .	13
1.5.2 Excess Micromotion . . . . .	14
<b>2 Doppler Cooling</b>	<b>16</b>
2.1 Introduction . . . . .	16
2.2 Doppler Cooling . . . . .	17
2.2.1 Optical Bloch Equations of a Two-Level Atom . . . . .	18
2.2.2 Radiation Pressure . . . . .	22
<b>3 Experimental Apparatus</b>	<b>25</b>
3.1 Setup Overview . . . . .	25
3.2 Lasers . . . . .	28
3.3 Detection and Imaging . . . . .	30
3.4 The Ion Traps . . . . .	34
3.4.1 The 'Sandwich' Trap . . . . .	34

---

3.4.2	The 'Alumina' Trap . . . . .	39
3.4.3	Micromotion Compensation . . . . .	50
<b>4</b>	<b>Spectroscopy of Single <math>^{40}\text{Ca}^+</math> Ions</b>	<b>58</b>
4.1	Introduction . . . . .	58
4.2	Theory . . . . .	58
4.2.1	Line Profile . . . . .	59
4.3	Measurements . . . . .	61
4.3.1	Repumper Spectroscopy and Initial Intensity Settings . . . . .	62
4.3.2	Cooling Transition Spectroscopy . . . . .	64
4.3.3	Cooling Transition Spectroscopy with Variations in Repumper Power . . . . .	66
4.3.4	Repumper Spectroscopy for Variations in Repumper Power . . . . .	67
<b>5</b>	<b>Heating Rate Measurement</b>	<b>70</b>
5.1	Introduction . . . . .	70
5.2	Spectrum of an Ion with Intermittent Cooling . . . . .	72
5.3	Heating Rates . . . . .	78
5.3.1	Experimental Procedure . . . . .	79
5.3.2	Results . . . . .	80
5.4	Conclusions . . . . .	82
<b>6</b>	<b>Coupling Ions and Cavity Mode</b>	<b>84</b>
6.1	Introduction . . . . .	84
6.2	Theory . . . . .	84
6.2.1	Optical Bloch Equations in a $\Lambda$ System . . . . .	84
6.2.2	Fabry-Pérot Cavities . . . . .	89
6.2.3	Ion-Cavity Coupling . . . . .	91
6.3	The Experimental Cavity surrounding the 'Alumina' Trap . . . . .	96
6.3.1	Experimental Setup . . . . .	96
6.3.2	Cavity Characterisation . . . . .	98
6.3.3	Stabilising the Cavity . . . . .	100
6.4	Cavity Parameters of the 'Alumina' Cavity . . . . .	106
6.5	Locating the Ions within the Cavity Mode . . . . .	107
6.5.1	Preliminary Results . . . . .	108
6.6	Conclusions . . . . .	112

---

<b>7</b>	<b>Conclusions and Outlook</b>	<b>113</b>
7.1	Conclusions . . . . .	113
7.2	Outlook . . . . .	115
7.2.1	Single Photon Source . . . . .	116
7.2.2	Two Ion Entanglement . . . . .	116
7.2.3	Quantum Networking . . . . .	118
	<b>Bibliography</b>	<b>120</b>

# List of Tables

3.1	Relative size of anharmonic contributions to the radial ponderomotive (rf) and axial (dc) confinement of the 'sandwich' trap . . . . .	38
3.2	Relative size of anharmonic contributions to the radial (ponderomotive) and axial (dc) confinement of the 'alumina' trap . . . . .	50
4.1	Summary of the repumper linewidths for the different power combinations of the repumpers laser beams . . . . .	69

# List of Figures

1.1	Diagram of a linear Paul trap . . . . .	6
1.2	Stability diagram for a linear Paul trap . . . . .	9
1.3	Stability diagram for a linear Paul trap for small $a$ and $q$ . . . . .	10
1.4	Trace of the radial ion motion in a linear Paul trap (1D) . . . . .	13
2.1	The basic principle of laser cooling . . . . .	17
2.2	2 level scheme . . . . .	18
2.3	The radiation pressure as a function of atomic velocity . . . . .	24
3.1	Photograph of the experimental chamber . . . . .	26
3.2	Photograph of the sub D connector vacuum flange . . . . .	27
3.3	Schematic of the vacuum chamber . . . . .	28
3.4	$^{40}\text{Ca}^+$ level scheme . . . . .	29
3.5	Schematic of the double pass AOM setup . . . . .	32
3.6	Schematic of the fluorescence detection setup . . . . .	33
3.7	Drawings of the 'sandwich' trap electrodes . . . . .	35
3.8	Photographs of the 'sandwich' trap assembly . . . . .	36
3.9	Radial cross-section of the pseudo-potential of the 'sandwich' trap . . . . .	37
3.10	Oven flux . . . . .	40
3.11	Technical drawings of the trap electrodes of the 'alumina' trap . . . . .	41
3.12	The solid works assembly of the alumina trap structure . . . . .	42
3.13	Photograph of the cavity base structure . . . . .	43
3.14	Technical drawing of the x-shaped stainless steel mounting structure for the 'alumina' electrodes . . . . .	43
3.15	Photograph of trap alignment tools . . . . .	44
3.16	Photograph of the alignment process . . . . .	44
3.17	Microscope picture of the trap electrodes with dimensions - side view . . . . .	45

3.18	Microscope picture of the trap electrodes with dimensions - axial . . . . .	45
3.19	Photograph of the assembled trap without cavity mirrors . . . . .	46
3.20	Electronic connections to the 'alumina' trap . . . . .	47
3.21	Autotransformer circuit diagram . . . . .	47
3.22	Radial cross-section of the pseudopotential of the 'alumina' linear trap . . . . .	49
3.23	Profile of the pseudopotential in the horizontal and vertical direction ('alumina' trap) . . . . .	49
3.24	Radial secular frequency as a function of dc voltage in the 'alumina' trap . . . . .	50
3.25	Axial secular frequency as a function of dc voltage in the 'alumina' trap . . . . .	51
3.26	Linewidth for small and large micromotion . . . . .	52
3.27	Modulation of ion fluorescence due to micromotion . . . . .	53
3.28	Micromotion compensation: Fluorescence amplitude for individual lasers . . . . .	55
3.29	Micromotion compensation: Two laser graph . . . . .	55
3.30	Average direction of stray fields in the 'sandwich' trap . . . . .	56
4.1	Optics and laser setup for spectroscopy and heating rate measurements . . . . .	62
4.2	Cooling fluorescence: Dependence on 850 nm repumper power . . . . .	63
4.3	Cooling fluorescence: Dependence on 854 nm repumper power . . . . .	63
4.4	Cooling fluorescence: Dependence on 850 nm repumper wavelength . . . . .	64
4.5	Cooling fluorescence: Dependence on 854 nm repumper wavelength . . . . .	64
4.6	Spectroscopy: Cooling transition, power dependent . . . . .	65
4.7	Cooling transition linewidth: Dependence on cooling laser power . . . . .	66
4.8	Cooling transition spectroscopy: Dependence on repumper power . . . . .	66
4.9	850 nm repumper spectroscopy . . . . .	68
4.10	854 nm repumper spectroscopy . . . . .	68
5.1	The fluorescence level dependence on the ion spectrum . . . . .	70
5.2	Ion fluorescence as a function of time, with the recooling laser switched on at $t=0$ . . . . .	71
5.3	Fluorescence spectra $S(\delta)$ calculated from equation (5.14) for different sets of parameters . . . . .	76
5.4	Calculated spectra $S_{\text{cooled}}$ for a cooled ion (blue) and $S_{\text{heated}}$ for a heated ion at a temperature of 1 K (red) . . . . .	77
5.5	Relative change $R = (S_0/S_\infty - 1)$ of fluorescence in the first bin after recooling starts, as a function of bin-size . . . . .	78

5.6	Fluorescence spectrum of the Doppler cooled ion, obtained under steady-state conditions . . . . .	80
5.7	Measured values for the relative fluorescence change $R = (S_0/S_\infty - 1)$ after 500 ms of heating . . . . .	81
5.8	Measured temperature of the ion as a function of heating time . . . . .	82
6.1	Simplified level scheme cavity-assisted Raman transition in $^{40}\text{Ca}^+$ . . . . .	85
6.2	Cooling fluorescence dependence on repumper intensity . . . . .	86
6.3	Theoretical cooling fluorescence spectrum for the three-level $\Lambda$ structure of the $^{40}\text{Ca}^+$ ion . . . . .	88
6.4	Fabry-Pérot cavity . . . . .	89
6.5	Hermite-Gaussian transverse modes . . . . .	90
6.6	Level scheme for a two-level atom coupled to a cavity containing $n$ photons . . . . .	93
6.7	Level scheme for a three-level atom coupled to a cavity containing $n$ photons . . . . .	94
6.8	Schematic of the experimental cavity and piezos . . . . .	97
6.9	Cross section through the 'Alumina' trap structure . . . . .	98
6.10	Using sidebands to determine cavity linewidth . . . . .	100
6.11	Schematic of the proposed setup for locking the experimental cavity to a sideband of the cesium reference laser . . . . .	101
6.12	Proportional feedback lock . . . . .	104
6.13	Revised cavity locking scheme . . . . .	105
6.14	Cavity length stabilisation . . . . .	105
6.15	The relationship of the ion cavity coupling strength $g_0$ , the cavity decay $2\kappa$ and the atomic decay rate $\Gamma$ with decreasing cavity length . . . . .	106
6.16	Experimental setup schematic for coupling ions and cavity mode . . . . .	107
6.17	Analysis of CCD recordings of ion fluorescence while repumping via the cavity - Low and medium intensity . . . . .	109
6.18	Analysis of CCD recordings of ion fluorescence while repumping via the cavity - High intensity . . . . .	110
6.19	Dc electrode geometry . . . . .	111
6.20	Ion position within the cavity mode for different axial dc voltages . . . . .	111
7.1	Single photon detection setup . . . . .	115
7.2	Two ions inside an optical cavity . . . . .	117
7.3	Schematic of transferring the quantum state between two ions in a cavity . . . . .	118

7.4 A scheme for mapping quantum states . . . . . 118

# Introduction

Before Planck's 1901 hypothesis that black-body radiation is emitted in discrete energy packets it was widely accepted that light was a wave. The wave theory had a firm theoretical footing in Maxwell's electro-magnetic wave equations, and the corpuscle theory proposed by Newton in the early years of the field of optics had long been abandoned. Four years later, in 1905, Einstein picked up on Planck's idea and used it to explain the photo-electric effect. Both these events laid the foundation for a reconsideration of the wave theory but it wasn't until the birth of quantum mechanics in the 1920s, and subsequently the explanation of atomic structure, that a formal theory of the quantisation of light was developed, most notably with the publication of Dirac's work on a quantum theory of radiation in 1927.

However, the lack of experimental techniques to manipulate individual atoms slowed down the progress in the field of quantum optics. Only with the development of the laser in 1960 did this change rapidly and the renewed interest in the field proved fruitful. The first experimental confirmation of the quantum nature of light came in 1977 when Kimble, Dagenais, and Mandel demonstrated photon antibunching [1].

Early experiments were carried out using low density atom beams. Consequently the length of available measurement time was limited and the random nature of the atoms' movement imposed additional statistics on the measurements. The development of the quadrupole ion trap by Paul in 1958 [2] provided a solution to this, allowing to isolate a single particle from its environment. When this technique was later combined with laser cooling it became possible to cool trapped ions to the Lamb-Dicke regime enabling experiments testing decoherence effects and spectroscopic measurements.

## **Strong Coupling Cavity Quantum Electrodynamics**

Cavity quantum electrodynamics (cavity QED) studies the interaction of matter and light confined to a cavity. The strong coupling regime, where the ion-cavity interaction dominates over decay processes which cause decoherence, and the radiative properties of the ion differ significantly from those of an ion in free space, is of particular interest. The dynamics of

such a system expose the quantum nature of light, and allow the observation of quantum effects, such as entanglement of ions and photons in a controllable manner. An experimental realisation of strong coupling reduces the system's decay processes while optimising the ion-cavity coupling. Compared to traveling atoms a trapped ion offers the advantage that the interaction time between ion and cavity is practically indefinite. The good localisation of the ion within the trap and thus the cavity mode is equally important as the use of a high finesse cavity with a small mode volume resulting in long photon lifetimes in the cavity and increased coupling between light field and ion, respectively. It is in fact the requirement of a small mode volume that poses the biggest challenge in the lab, because the dielectric mirror substrates can cause distortion of the trapping fields. It is therefore necessary to find a trap cavity combination for which trapping conditions are minimally affected by the close proximity of the mirrors to the trap centre.

### **Structure of this Thesis**

This thesis covers my work during my time within the ion trap cavity QED (ITCQ) group. It introduces the theory behind linear radio frequency ion traps (chapter 1), and explains the principles of Doppler laser cooling (chapter 2). All aspects of the experimental apparatus used to conduct the experiments are covered in chapter 3, apart from the experimental cavity which is introduced in chapter 6. Particular attention is given to the design, assembly, and characterisation of the two novel types of microscopic ion traps that we used. Chapter 4 presents the calcium spectroscopy measurements carried out, and introduces a less common re-pumping scheme that allows to treat the ion as a two-level system. The heating rate measurements carried out on the first of our ion traps are covered in chapter 5, presenting also a new theoretical model to analyse this type of data. The first steps to implement a cavity within the system were taken with the second trap, and first experimental data indicating the localisation of the ions within the cavity mode was obtained. This is detailed in chapter 6. Chapter 7 concludes this thesis, and gives an outlook on the future of the experiment.

Throughout the first two years I worked on the experiment with Anders Mortensen who had already assembled the 'sandwich' trap when I joined the group. I used this experimental setup to carry out the spectroscopy measurements. During this time we also carried out the extensive heating rate measurements, which we analysed with Wolfgang Lange's help resulting in a publication of the results ('Heating rates in a thin ion trap for microcavity experiments', Applied Physics B, June 2012, Volume 107, Issue 4, pp 945-954). The new trap was designed with Matthias Keller's help. After Anders left the group in the summer of 2010, I carried

out the work needed to observe the first ion signal in the new trap, characterised it, and implemented the cavity in the setup.

# Chapter 1

## Ion Traps

### 1.1 Introduction

The development of ion traps finally enabled scientists to suspend single charged particles of matter in free space for long periods of time so they could be studied in an isolated environment. Earnshaw's theorem states that creating a three dimensional electric field potential minimum using static fields alone is not possible, so alternative methods have to be employed. There are two approaches to solving this problem. The use of time-varying quadrupole fields (Paul trap), or alternatively a combination of static magnetic and electric fields can achieve stable trapping (Penning trap). Much of the technology used was originally developed to build a particle mass filter [2]. The first traps relied on ponderomotive forces for trapping in all three dimensions. The linear Paul trap combines a radio-frequency field for radial trapping with a dc potential along its axis. This type of trap was only experimentally realised in 1989 for the purpose of frequency standard applications [3], but seems much more intuitive in retrospect when one considers the development of ion trap technology from the particle mass filter.

### 1.2 Ion Trap Theory

If a particle is bound to any point in space by a force towards this point that increases linearly with the distance  $r$  of the particle to the point, that is

$$\vec{F} = -C\vec{r}, \quad (1.1)$$

where  $C$  is a constant of proportionality, its motion is harmonic.

A force of this form gives rise to a parabolic potential, which can be created by use of electric or magnetic multipole fields, or a combination of both. A quadrupole potential gives the force

distance relationship required. In cartesian coordinates an electrical quadrupole field takes the form

$$\Phi = \frac{\Phi_0}{2r_0^2} (\alpha x^2 + \beta y^2 + \gamma z^2) . \quad (1.2)$$

Gauss's law requires the divergence of any electrical force field to be zero in free space. To trap a particle a local minimum in the potential is necessary. However, at such a minimum all force field lines point towards this minimum position, resulting in a negative divergence. Thus trapping a charged particle in three dimensions using static electric fields only is not possible. This is known as the Laplace condition or Earnshaw's theorem,

$$\nabla^2 \Phi = 0 . \quad (1.3)$$

The Laplace condition imposes the constraint

$$\alpha + \beta + \gamma = 0 . \quad (1.4)$$

The two simplest solutions are sufficient to describe the two types of ion traps commonly used today. If  $-\alpha = \beta = 1$  and  $\gamma = 0$  we obtain the two dimensional case,

$$\Phi = \frac{\Phi_0}{2r_0^2} (y^2 - x^2) , \quad (1.5)$$

which was applied for the mass spectrometer, and is used in combination with a static electric field in the third dimension to form a linear Paul trap, such as described in this thesis.

If  $\alpha = \beta = 1$  and  $\gamma = -2$  the resulting potential is three dimensional, and it was this type of potential that was used in the first ion trap.

### 1.3 Linear Paul Trap

An example of a linear Paul trap is shown in 1.1. A time varying potential of amplitude  $U_{AC}$  is applied to two electrodes which are diagonally opposite to one another. A second pair arranged in the same way but mirrored with respect to the  $y-z$  plane is connected to ground. The ponderomotive potential arising between these electrodes provides the confinement in the the radial direction. The axial confinement is a result of holding four additional electrodes which are displaced from the trap centre in the axial direction at a potential  $+U_{DC}$ .

Considering the radial dimensions in such a trap only, it follows from the 2D solution (1.5)

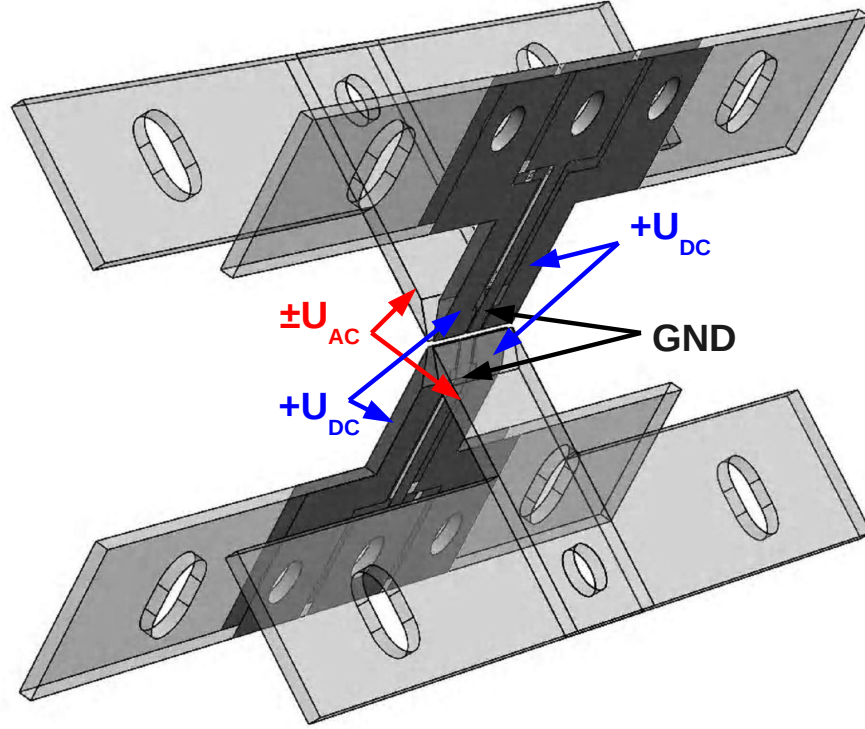


Figure 1.1: Example of a linear Paul trap. The trap is driven asymmetrically with the rf electrodes varying between  $+U_{AC}$  and  $-U_{AC}$ , while the centre electrode of the split substrates are kept at ground. The dc axial confinement is delivered via the four outer electrodes of the split substrates, which are held at  $+U_{DC}$ .

that the electric field exerted is

$$E = \frac{\Phi_0}{r_0^2} \begin{pmatrix} x \\ -y \\ 0 \end{pmatrix}. \quad (1.6)$$

For a constant potential  $\Phi_0$  this field will lead to the particle being bound harmonically in the  $y$  direction, while in the  $x$  direction the amplitude of the particle's motion will increase indefinitely. To achieve trapping in both  $x$  and  $y$  a potential of the form

$$\Phi_{\text{radial}} = \frac{1}{2r_0^2} \left( U_{DC}^{\text{radial}} + U_{AC} \cos \Omega_{RF} t \right) \begin{pmatrix} -x^2 \\ y^2 \\ 0 \end{pmatrix} \quad (1.7)$$

is used, which contains a dc component  $U_{DC}^{\text{radial}}$ , and an ac component  $U_{AC} \cos \Omega_{RF} t$  applied to two opposing electrodes, which oscillates with frequency  $\Omega_{RF}$ , swapping the plane in which

dynamic confinement exists periodically.

The axial dc electrodes exert a potential which at the centre of the trap, i.e. far away from the electrodes themselves, can be approximated as quadratic. Again, the Laplace conditions has to be fulfilled, and the resulting potential has the form

$$\Phi_{\text{axial}} = A \cdot U_{\text{DC}}^{\text{axial}} \left( z^2 - \frac{1}{2} (x^2 + y^2) \right), \quad (1.8)$$

where  $A$  is a geometrical factor to account for the deviation of the electrodes from the hyperbolic shape of an ideal trap. The axial dc voltages contribute to the potential in the radial direction, and the sum of the two potentials (1.7) and (1.8) must be used to derive the total electric field that a charged particle at the centre of the trap is subject to.

$$\vec{E} = -\vec{\nabla} \Phi_{\text{total}}(t) = \frac{1}{r_0^2} \left( U_{\text{DC}}^{\text{radial}} + U_{\text{AC}} \cos \Omega_{\text{RF}} t \right) \begin{pmatrix} x \\ -y \\ 0 \end{pmatrix} + A \cdot U_{\text{DC}}^{\text{axial}} \begin{pmatrix} -x \\ -y \\ 2z \end{pmatrix} \quad (1.9)$$

Note that equation (1.9) shows that there is no net force from the rf potential on an ion located at the centre of the trap.

The equations of motion of a particle moving in such a force field are

$$\ddot{x} + \frac{e}{m} \left( A \cdot U_{\text{DC}}^{\text{axial}} - \frac{U_{\text{DC}}^{\text{radial}} + U_{\text{AC}} \cos \Omega_{\text{RF}} t}{r_0^2} \right) x = 0 \quad (1.10)$$

$$\ddot{y} + \frac{e}{m} \left( A \cdot U_{\text{DC}}^{\text{axial}} + \frac{U_{\text{DC}}^{\text{radial}} + U_{\text{AC}} \cos \Omega_{\text{RF}} t}{r_0^2} \right) y = 0 \quad (1.11)$$

$$\ddot{z} - 2 \frac{e}{m} A \cdot U_{\text{DC}}^{\text{axial}} z = 0 \quad (1.12)$$

Equations (1.10), and (1.11) are Mathieu differential equations [4, 5], which have the canonical form

$$\frac{d^2 x}{d\tau^2} + (a - 2q \cos(2\tau)) x = 0. \quad (1.13)$$

By comparing equations (1.10) and (1.11) to (1.13) we can conclude

$$a_x = \frac{4e}{m\Omega_{\text{RF}}^2} \left( AU_{\text{DC}}^{\text{axial}} - \frac{U_{\text{DC}}^{\text{radial}}}{r_0^2} \right), \quad (1.14)$$

$$a_y = \frac{4e}{m\Omega_{\text{RF}}^2} \left( AU_{\text{DC}}^{\text{axial}} + \frac{U_{\text{DC}}^{\text{radial}}}{r_0^2} \right), \quad (1.15)$$

$$a_z = -\frac{8e}{m\Omega_{\text{RF}}^2} AU_{\text{DC}}^{\text{axial}}, \quad (1.16)$$

$$q_x = -q_y = \frac{2eU_{\text{AC}}}{mr_0^2\Omega_{\text{RF}}^2}, \text{ and} \quad (1.17)$$

$$q_z = 0, \quad (1.18)$$

with  $\tau = \Omega_{\text{RF}}t/2$ .

Knowing that a complete solution to equation (1.13) is the sum of two linear independent solutions, and using Floquet's theorem the general solution can be written as [6]

$$x_i(\tau) = \Gamma e^{\mu\tau} \Psi(\tau) + \Gamma' e^{-\mu\tau} \Psi(-\tau) \quad (1.19)$$

where the index  $i$  represents the two radial dimensions. Using Fourier's theorem this can also be written as

$$x_i(\tau) = \Gamma e^{\mu\tau} \sum_{n=-\infty}^{\infty} C_{2n} \exp(2ni\tau) + \Gamma' e^{-\mu\tau} \sum_{n=-\infty}^{\infty} C_{2n} \exp(-2ni\tau) \quad (1.20)$$

The coefficients  $C_{2n}$  depend on  $a$  and  $q$  only, and describe the amplitude of the ion motion.  $\mu = \alpha + i\beta$  and is an important parameter for characterising the types of solutions to the Mathieu equation. To trap ions the solutions have to be stable, i.e. the ion's motional amplitude has to be restricted, so we can immediately say that  $\alpha$  has to equal zero. There are four possible types of values  $\mu$  can take that depend solely on  $\beta$ :

1.  $\mu$  is a real number unequal zero. Either  $e^{\mu\tau}$  or  $e^{-\mu\tau}$  will increase without limit. The solutions are not stable.
2.  $\mu$  is a complex number, and the solutions are not stable.
3.  $\mu = in$  (for integer  $n$ ), and the solutions are periodic but unstable. These curves are of interest as they define the boundaries of regions of stability on an  $a$  versus  $q$  stability diagram.
4.  $\mu = i\beta$  where  $\beta$  is not a whole number. These solutions are stable and periodic, and define the criteria for stable trapping conditions.

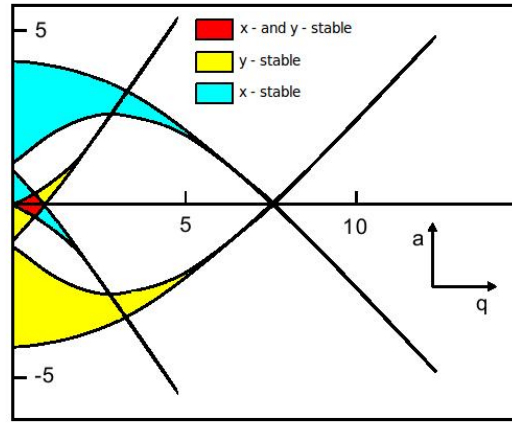


Figure 1.2: Stability diagram for a linear Paul trap [7]

Substituting  $i\beta$  for  $\mu$  in equation (1.20), and using trigonometric identities the equation of motion of an ion in the trap can be written as

$$x_i(\tau) = A \sum_{n=0}^{\infty} C_{2n} \cos((2n + \beta)\tau) + B \sum_{n=0}^{\infty} C_{2n} \sin((2n + \beta)\tau), \quad (1.21)$$

with  $A = \Gamma + \Gamma'$  and  $B = i(\Gamma - \Gamma')$ . Parameters  $A$  and  $B$  depend solely on the initial conditions of the system.  $\beta$  is a function of the  $a_i$  and  $q_i$ , and a general solution of the dependencies is only possibly numerically. Figure 1.2 shows a plot of the  $a_i$  versus  $q_i$  for both  $x$  and  $y$  direction. The boundaries of the regions of stability correspond to the solutions of the Mathieu equation that are periodic but unstable. It is obvious from figure 1.2 that the most interesting region for trapping arises for low values of  $a_i$  and  $q_i$  (red area). A more detailed plot is shown in figure 1.3.

### 1.3.1 Ion Motion

If we examine equation (1.21) in more detail we see that the ion carries out periodic motion around the trap centre. The frequency of this so-called secular motion can be identified from this equation as  $(2n + \beta)\tau$ . Using the definition of  $\tau$  the motional frequency of the ion is defined as

$$\omega_n = \frac{(2n + \beta)\Omega_{\text{RF}}}{2} \quad (1.22)$$

The amplitude of the secular motion expresses the energy of the ion, and hence cooling the ion will reduce its amplitude. The secular frequency is typically one order of magnitude smaller than the drive frequency.

As we noted in equation (1.9) an ion at the centre of the trap experiences no net force from

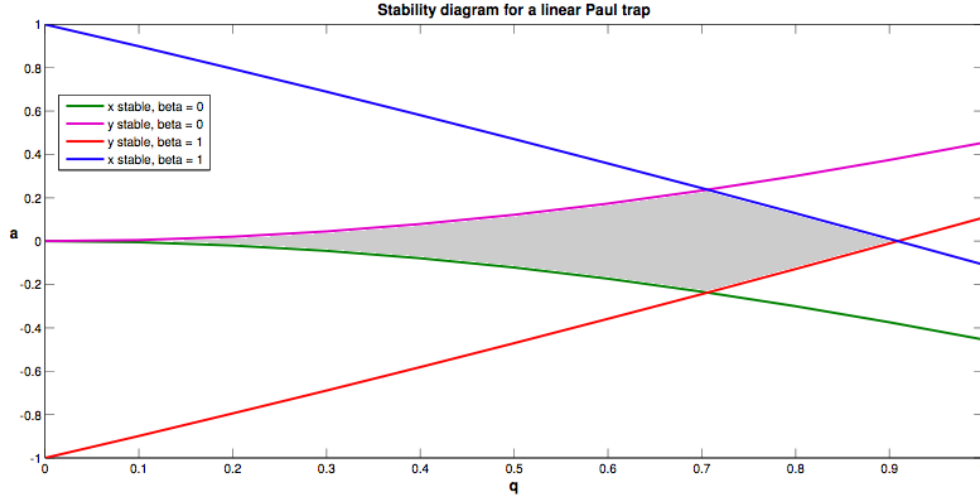


Figure 1.3: Stability diagram of a linear Paul trap for small  $a$  and  $q$ . The shaded area is the region of stability.

the rf field. However, equation (1.22) tells us that the ion confined in the trap carries out oscillations of some amplitude around the trap centre, i.e. it periodically leaves the trap centre, and hence experiences a force from the rf field. This is the cause of the so-called micromotion. For small  $a$  and  $q$   $\beta$  can be approximated by  $\beta = \sqrt{a + \frac{q^2}{2}}$  because the higher order oscillating terms of the solution to the equation of motion are negligible. Substituting into the equation of motion 1.13 and assuming  $a = 0$  for simplicity:

$$\frac{d^2x}{d\tau^2} + (2q \cos(2\tau)) x_0 = 0. \quad (1.23)$$

Further assuming the initial condition  $\frac{dx}{d\tau}(0) = 0$  the solution to 1.23 is

$$x(\tau) = x_0 \left( 1 + \frac{q}{2} \cos(2\tau) \right). \quad (1.24)$$

Since  $\tau = \Omega_{\text{RF}}t/2$  this equation describes motion of the ion at the trap drive frequency while located at a fixed position  $x_0$ , i.e. the micromotion.

## 1.4 Pseudopotential Approximation

The pseudopotential approximation is useful to understand the net effects of the rf trapping fields. It allows to extract trapping parameters like  $U_{AC}$ ,  $U_{DC}$  and conclude the corresponding secular frequencies. Furthermore it can be used for finite element simulations of a trap design to render its use viable. The results of these simulations for the traps described in this thesis are presented in chapter 3.

A particle subject to a high-frequency force field,  $\vec{F}(\vec{x}, t) = \vec{f}(\vec{x}) \cos(\Omega_{RF}t)$ , moves as if inside an effective potential

$$V_{\text{eff}} = \frac{\vec{f}(\vec{x}) \cdot \vec{f}(\vec{x})}{4m\Omega_{RF}^2}. \quad (1.25)$$

Following the derivation by Ghosh [6] the amplitude of the ion's motion in a quadrupole ion trap,  $x_i$ , is replaced by the sum of the secular motion amplitude and the micromotion amplitude as described in section 1.3.1:

$$x_i = X_i + \Delta_i. \quad (1.26)$$

The equation of motion of an ion in the rf field only was described earlier to have the form of a Mathieu differential equation (1.13). Making the assumptions that  $\Delta_i \ll X_i$ , and  $d\Delta_i/dt \gg dX_i/dt$  we can write

$$\frac{d^2\Delta_i}{d\tau^2} + (a_i - 2q_i \cos(2\tau)) X_i = 0. \quad (1.27)$$

If we restrict ourselves to the region where  $a \ll q$  and approximate the position due to the secular motion ( $X_i$ ) within one period of micromotion oscillation, integrating and substituting from equation (1.26) for  $\Delta$  gives

$$x_i = X_i - \frac{q_i X_i}{2} \cos(2\tau). \quad (1.28)$$

The equation of motion using these approximations is

$$\frac{d^2 x_i}{d\tau^2} + a_i X_i - \frac{a_i q_i X_i}{2} \cos(2\tau) - 2q_i X_i \cos(2\tau) + q_i^2 X_i \cos^2(2\tau) = 0. \quad (1.29)$$

The average acceleration of the ion during the cycle of secular motion is

$$\left\langle \frac{d^2 X_i}{d\tau^2} \right\rangle = \frac{1}{\pi} \int_0^\pi \frac{d^2 x_i}{d\tau^2} d\tau, \quad (1.30)$$

because the average of the acceleration  $\frac{d^2\Delta}{d\tau^2}$  is zero over one period of the drive frequency. Integrating and reverting to  $t$  results in

$$\frac{d^2 X_i}{dt^2} = -\frac{\Omega_{\text{RF}}^2}{4} \left( a_i + \frac{q_i^2}{2} \right) X_i. \quad (1.31)$$

Equation (1.31) is an equation of simple harmonic motion, and hence the factor in front of the  $-X_i$  can be identified as the secular frequency. We also know that the lowest order motional frequency from equation (1.22) is  $\omega_0 = \frac{\beta\Omega_{\text{RF}}}{2}$ , and so  $\beta_i = \sqrt{a_i + \frac{q_i^2}{2}}$ . If the rf field has no dc component,  $a_i$  is zero. Using the expression for  $q_i$  from equation (1.17) it follows that

$$\frac{d^2 X_i}{dt^2} = -\frac{e^2 U_{\text{AC}}^2}{2m^2 r_0^4 \Omega_{\text{RF}}^2} X_i. \quad (1.32)$$

With a little rearranging equation (1.32) can be shown to be of the form  $\vec{F} = -e\vec{\nabla}\Phi = m\vec{a}$ , with the gradient of the potential

$$\frac{dV_{\text{eff}}}{dX_i} = \frac{eU_{\text{AC}}^2}{2mr_0^4\Omega_{\text{RF}}^2} X_i, \quad (1.33)$$

where  $V_{\text{eff}}$  is a parabolic pseudopotential:

$$V_{\text{eff}} = \frac{eU_{\text{AC}}^2}{4mr_0^4\Omega_{\text{RF}}^2} X_i^2. \quad (1.34)$$

The depth of this potential is defined by the magnitude of the potential barrier that an ion faces when moving away from the centre of the trap.

### 1.4.1 Ion Motion within the Pseudopotential Approximation

It is possible to derive an equation for the secular ion motion from equation (1.31):

$$X_i = A_i \cos(\omega_n t), \quad (1.35)$$

where  $A_i$  is the amplitude of the oscillation. Going back to equation (1.27), and integrating we arrive at an expression for the micromotion

$$\Delta_i = -\frac{q_i X_i}{2} \cos(2\tau) \quad (1.36)$$

So the pseudopotential approximation gives rise to a simplified equation of motion [8]

$$x_i(t) = A_i \cos(\omega_n t + \phi_i) \left[ 1 - \frac{q_i}{2} \cos(\Omega_{\text{RF}} t) \right]. \quad (1.37)$$

$A_i$  and  $\phi_i$  are determined by the initial conditions, and  $\omega_n$  is the secular frequency of the ion

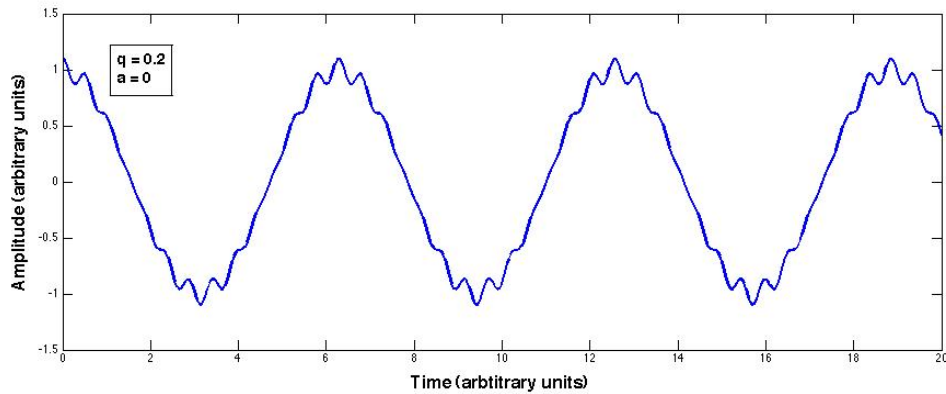


Figure 1.4: Trace of the radial ion motion in a linear Paul trap in one dimension. The slow oscillation is the secular motion. The micromotion has the same frequency as the trap drive and increases in amplitude as the ion moves out of the trap centre.

as defined in equation (1.22). The first oscillatory term describes the ion's secular motion, the second oscillatory term with a frequency equal to that of the trap drive is the intrinsic micromotion explained in section 1.3.1. The similarity between equations 1.24 and 1.37 is immediately obvious and confirms that for ion motion within the limit of low  $a$  and  $q$  the pseudopotential approximation achieves the same result as a more thorough calculation from first principles.

Figure 1.4 shows a plot of an ions radial motion in one dimension with both secular motion and intrinsic micromotion present. The sum of these two oscillation represents the total energy.

## 1.5 Non Ideal Trap

The analysis of the ion trap theory so far assumed an ideal trap, that is the electrode shape is hyperboloid. While this shape requires a cumbersome machining process, there are two further reasons why using electrodes of different shape is an advantage. Even if the electrodes where hyperbolic the trap exists in a non-ideal environment. In addition for the proposed experiments good optical access is vital. This is much easier to realise with non-hyperbolic electrodes.

### 1.5.1 Trap Efficiency and Anharmonicity

The trap efficiency  $\eta$  [9] describes how much the non ideal shape of the trap electrodes affects the rf voltage required for a given trapping potential. It is one for the ideal trap, and smaller than one for all other traps:

$$\eta \cdot U_{AC}^{\text{ideal}} = U_{AC}^{\text{real}} \cdot \quad (1.38)$$

It is equivalent to the ratio of the potential of an ideal trap to the hyperbolic part of the real potential :

$$\eta = \frac{2r_0^2 C_2}{U_{AC}}, \quad (1.39)$$

where  $C_2$  is the second order amplitude term from the power series expansion of the potential. The anharmonicity expresses the difference of the trap potential  $\Phi$  from that of a quadrupole potential, and is given in [10] as

$$f(x) = \left| \frac{\Phi - A_0 - A_2 x^2}{A_2 x^2} \right|. \quad (1.40)$$

In an ideal trap this factor vanishes for all values of  $x$ . For positions close to the trap centre, i.e.  $x \ll r_0$ ,  $f(x)$  is very small, and can be neglected. Furthermore, Alheit *et al.* [11] showed that the anharmonicity has no influence on trapping stability.

## 1.5.2 Excess Micromotion

In addition to the intrinsic micromotion there is also excess micromotion. However, in contrast to the intrinsic micromotion it can be eliminated. Three mechanisms contribute to excess micromotion [12].

Stray static electric fields are the most prominent cause by far. They can result from static charges on dielectric materials often used for insulating purposes close to the trap which can become charged for example from interaction with laser beams crossing the trap. Coating of metal surfaces with calcium from oven operation can also be a source. However, stray fields are also the easiest to compensate by using additional dc voltages, and the details of this compensation are covered in chapter 3. A stray electric field introduces the an additional displacement:

$$\Delta x_i = \frac{eE_i^{\text{Stray}}}{m\omega_i^2}, \quad (1.41)$$

and equation (1.37) has to be modified to

$$x_i(t) = \left[ \Delta x_i^{\text{Stray}} + A_i \cos(\omega_i t + \phi_i) \right] \left[ 1 - \frac{q_i}{2} \cos(\Omega_{\text{RFT}} t) \right]. \quad (1.42)$$

In addition to the intrinsic micromotion amplitude which varies as a function of the secular frequency, and additional motion at the trap drive frequency with constant amplitude is imposed by the stray field.

The two other causes of excess micromotion can also be eliminated, but since this requires adjustment of the trap's components this is much more difficult to facilitate retrospectively.

If the trap electrodes are badly adjusted with respect to one another in the axial direction, i.e. the electrodes are tilted with respect to the axis, an additional component to the rf field along the trap axis arises. This results in an oscillation along the trap axis that can not be compensated for. Bad adjustment in the radial direction only leads to a smaller trap efficiency. Finally a phase difference between two opposite rf electrodes to which the same rf field is applied introduces an additional term to the electric field and hence the equation of the ion position [12]:

$$x_i^{\text{Phase}}(t) \propto -\frac{1}{4}q_i r_0 \phi \sin(\Omega_{\text{RF}} t), \quad (1.43)$$

where  $\phi$  is the phase difference between the electrodes which can be assumed to be small such that  $\cos(\Omega_{\text{RF}} t \pm \frac{1}{2}\phi) \approx \cos \Omega_{\text{RF}} t \pm \frac{1}{2}\phi \sin \Omega_{\text{RF}} t$ . Note that this motion is  $\pi$  out of phase with the trapping field oscillation, and independent of the ion's position. Thus it can't be eliminated by moving the ion. A phase difference can be caused by a difference in the length of cables supplying the electronic signal to the electrodes, and a difference of the impedance between the electrodes. Since not only the electrode but also the cabling leading to the trap contribute to this impedance, shorter cables are advantageous.

## Chapter 2

# Doppler Cooling

### 2.1 Introduction

To achieve the deterministic coupling required for our experiments the ions need to be localised to within one wavelength of the optical transition of the ion. This is known as the Lamb - Dicke regime and defined by

$$x < \frac{\lambda}{2\pi}. \quad (2.1)$$

Thus the ion's motional amplitude and with that its temperature has to be reduced. For the wavelengths concerned in our experiments the Lamb - Dicke regime equates to temperatures in the mK range. During the trapping process the ion energy is typically of the order of Kelvin. Reduced temperatures also result in longer ion lifetimes in the trap as the ions have less energy to overcome the potential barrier of the trap.

There are a number of cooling techniques for trapped ions, many of which employ the damping forces of radiation, Doppler cooling being the most prominent member of this group. However, resistive cooling [13, 14], active feedback (stochastic) cooling [15], and collisional cooling [16] have all been successfully employed. Sympathetic cooling [17] combines collisional and laser cooling, polarisation gradient (Sisyphus) cooling [18] makes use of the AC Stark shift present during the atom light interaction. Which method is chosen depends on the initial conditions of the system, and the final temperature to be achieved.

While light forces on atomic particles were studied as early as the 1930s, the development of lasers was necessary to make use of these forces for cooling. Laser cooling was first proposed by Hänsch and Schawlow in 1975 [19] for the case of free particles, and in the same year for trapped ions by Wineland and Dehmelt [20]. In 1978 both Wineland and Dehmelt were involved in experiments that showed laser cooling of trapped atoms for the first time [21, 22].

## 2.2 Doppler Cooling

The basic mechanism of Doppler cooling is illustrated in figure 2.1. Every photon carries momentum  $\hbar k$  where  $k = 2\pi/\lambda$ . When a photon is absorbed by an atom it transfers this momentum, and, provided the atom is travelling towards the laser beam, slows it down. To

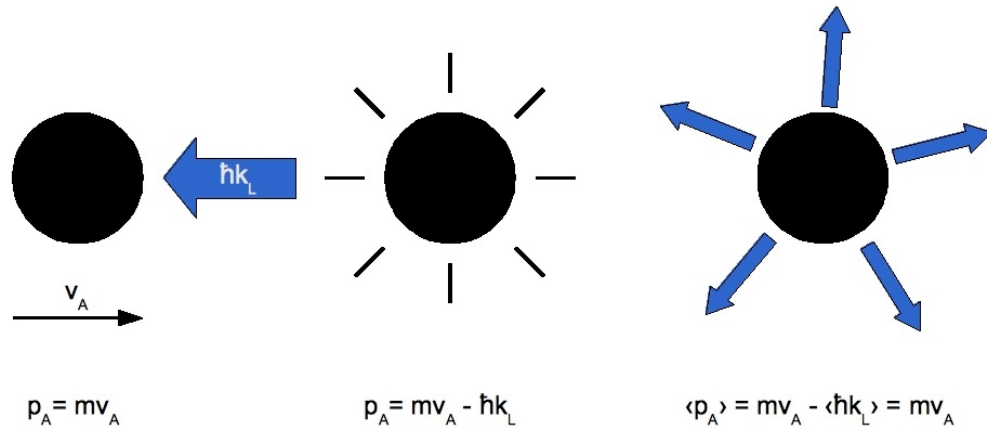


Figure 2.1: An illustration of the basic principle of laser cooling. An atom moving towards the right with velocity  $v_A$  absorbs a photon which carries momentum  $\hbar k_L$ . As the atom absorbs the photon its momentum changes to  $p = mv_A - \hbar k_L$ . The re-emission of absorbed photons is isotropic, and hence after multiple cycles of absorption and emission the average momentum change of the photon is  $\langle p_A \rangle = mv_A - \langle \hbar k_L \rangle = mv_A$  since  $\langle \hbar k_L \rangle = 0$ .

ensure that only atoms traveling towards the laser beam can absorb a photon the laser is slightly red detuned. For these atoms the light is Doppler shifted to resonance. Another reason for choosing a red detuned laser is that the finite linewidth of the atomic transition would mean that resonant light could excite atoms traveling in the same direction as the light, which would result in heating. While the absorption process is highly directional the re-emission of photons occurs in a random manner, and so on average over many absorption emission cycles imparts zero momentum on the atom. Hence there is a net cooling effect in the direction of the laser beam. The energy change per scattering event is small and corresponds to a change in atomic velocity of the order of cm/s. Assuming a calcium ion moves initially at 500 m/s, and we want to cool it to 1 mK (equivalent to 14 m/s), this equates to approximately 19 000 scattering processes.

To understand the principle of laser cooling it is necessary to examine the interaction between an atom and a light field in more detail.

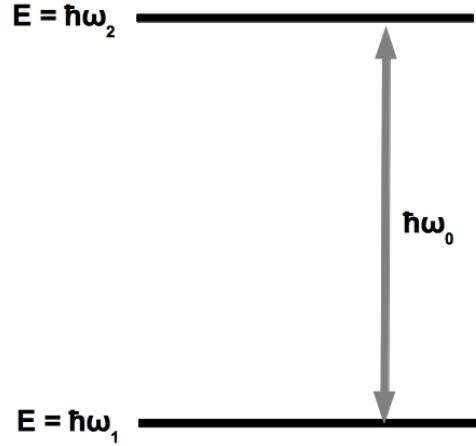


Figure 2.2: A diagram describing the energy of the two atomic levels concerned. Their energy difference is characterised by  $\omega_0$ .

### 2.2.1 Optical Bloch Equations of a Two - Level Atom

The interaction between the atom and a single mode laser light field can be described using the Bloch equations. The total Hamiltonian for a system consisting of a two-level atom with energy levels as given in figure 2.2 and an oscillating classical field is  $\hat{H} = \hat{H}_A + \hat{V}(t)$ , where  $\hat{H}_A$  is the atom's Hamiltonian and  $\hat{V}(t)$  is the light field. The time-dependent wavefunction of a two-level atom in a pure state excluding spontaneous emission is a linear combination of the two stationary states [23]:

$$\Psi(\vec{r}, t) = C_1(t) \psi_1(\vec{r}) e^{-i\omega_1 t} + C_2(t) \psi_2(\vec{r}) e^{-i\omega_2 t}, \quad (2.2)$$

where  $\omega_1$  and  $\omega_2$  are the frequencies associated with the atomic energy levels 1 and 2 respectively. If we substitute equation (2.2) into the time-dependent Schrödinger equation  $\hat{H}\Psi(\vec{r}, t) = i\hbar \frac{d\Psi}{dt}$ , multiply from the left with  $\psi_1^* e^{i\omega_1 t}$  and  $\psi_2^* e^{i\omega_2 t}$  respectively, and integrate, the results are

$$C_1 V_{11} + C_2 e^{-i\omega_0 t} V_{12} = i\hbar \frac{dC_1}{dt}, \quad (2.3)$$

for  $C_1$  and

$$C_1 e^{i\omega_0 t} V_{21} + C_2 V_{22} = i\hbar \frac{dC_2}{dt}, \quad (2.4)$$

for  $C_2$  where the  $V_{12}$  are the matrix elements  $\int \psi_n^* \hat{V} \psi_m d\vec{r}$ , and  $\hbar\omega_0$  energy difference between the two levels. The  $C(t)$  describe the occupation of the two atomic energy levels as a function of time.

$V$  is the field coupling operator:  $\hat{V} = -\hat{d} \cdot \vec{E}$ , where  $\hat{d} = -e\hat{r}$  is the quantum mechanical dipole operator and  $\vec{E}$  the electric field.  $\hat{V}$  has odd parity with respect to the electron coordinate so the matrix elements  $V_{mn}$  vanish if  $m = n$ . Only atomic states of opposite parity can be coupled by the dipole interaction. For an electromagnetic wave traveling along the z-axis the electric field is  $\vec{E} = \hat{e}E_0 \cos(\omega t - kz)$ , so we can write the matrix elements as

$$V_{12} = eE_0 r_{12} \cos(\omega t), \quad (2.5)$$

with  $n \neq m$  and  $r_{12} = \int \psi_1^* (\hat{r} \cdot e) \psi_2 d\tau$ . The transition dipole matrix element is defined as  $\mu_{12} \equiv er_{12}$ . By defining a new variable which contains all scalar quantities occurring in equation (2.5),  $\Omega_0 = \frac{\mu_{12}E_0}{\hbar}$ , which is known as the Rabi frequency, the expression simplifies to

$$V_{12} = \hbar\Omega_0 \cos(\omega t). \quad (2.6)$$

Returning to equations (2.3) and (2.4) we can now write these as

$$\hbar\Omega_0 \cos(\omega t) e^{-i\omega_0 t} C_2 = i \frac{dC_1}{dt} \quad (2.7)$$

$$\hbar\Omega_0^* \cos(\omega t) e^{i\omega_0 t} C_1 = i \frac{dC_2}{dt}, \quad (2.8)$$

with  $\omega_0$  the frequency of the atomic transition.

Up until now we have used the Schrödinger equation to describe the interaction between atom and light because the system could always be represented by a wave function. In preparation of introducing spontaneous emission in the next section, where this is no longer true and the use of probability distributions becomes necessary, the switch to the density matrix representation seems appropriate here.

Using the time-dependent form of the quantum state,  $\Psi_n(\vec{r}, t) = \psi_n(\vec{r}) e^{-i\omega_n t}$ , and using  $\psi_1$  and  $\psi_2$  as the basis states the matrix elements of the density operator,

$$\rho = \sum_{nm} c_{ni} c_{mi}^* |n\rangle \langle m|, \quad (2.9)$$

can be written as

$$\rho_{11} = |C_1|^2 \quad (2.10)$$

$$\rho_{22} = |C_2|^2 \quad (2.11)$$

$$\rho_{12} = C_1 C_2^* \quad (2.12)$$

$$\rho_{21} = C_2 C_1^* . \quad (2.13)$$

The diagonal terms are called populations as they describe the probability density of finding an atom in the ground or excited state. The off-diagonal terms are called coherences, and express the presence of superposition states. To find the time evolution of the populations and coherences we differentiate equations (2.10), (2.11), (2.12), and (2.13) with respect to time, and substitute equations (2.7) and (2.8) for  $\frac{dC_1}{dt}$  and  $\frac{dC_2}{dt}$  respectively. For near-resonant light at low intensities we can make the rotating wave approximation, that is we can neglect all terms in the Hamiltonian that oscillate at high frequencies because their contributions to  $\frac{d\rho_{22}}{dt}$  and  $\frac{d\rho_{12}}{dt}$  are small. Furthermore assuming  $\Omega_0^* = \Omega_0$  we can then write

$$\frac{d\rho_{22}}{dt} = i\frac{\Omega_0}{2} \left( e^{i\delta t} \rho_{21} - e^{-i\delta t} \rho_{12} \right) = -\frac{d\rho_{11}}{dt} \quad (2.14)$$

$$\frac{d\rho_{12}}{dt} = i\frac{\Omega_0}{2} e^{i\delta t} (\rho_{11} - \rho_{22}) = \frac{d\rho_{21}^*}{dt} , \quad (2.15)$$

where  $\delta = \omega - \omega_0$  is the detuning.

Equations (2.14) and (2.15) are the optical Bloch equations for a two-level atom without spontaneous emission. Solving these is straight forward as long as we choose the right initial conditions, i.e. the entire population is in the ground state, and the laser interaction is not present. In this case the solutions are

$$\rho_{22} = 1 - \rho_{11} = \frac{\Omega_0^2}{\Omega^2} \sin^2 \left( \frac{\Omega}{2} t \right) , \text{ and} \quad (2.16)$$

$$\rho_{12} = \rho_{21}^* = e^{i\delta t} \frac{\Omega_0}{\Omega^2} \sin \left( \frac{\Omega}{2} t \right) \left[ \delta \sin \left( \frac{\Omega}{2} t \right) + i\Omega \cos \left( \frac{\Omega}{2} t \right) \right] . \quad (2.17)$$

$\Omega = \sqrt{\delta^2 + \Omega_0^2}$  is the generalised Rabi frequency.

### Spontaneous Emission

Spontaneous emission gives expression to the fact that the atomic system is in principle coupled to all modes other than the laser radiation field, which are in the vacuum state. To account for this radiative loss of upper state population an additional factor is introduced into equation

(2.8):

$$\hbar\Omega_0^* \cos(\omega t) e^{i\omega_0 t} C_1 - i\gamma C_2 = i \frac{dC_2}{dt}. \quad (2.18)$$

The spontaneous emission rate is usually characterised by the Einstein  $A$  coefficient, more often referred to as  $\Gamma$ , which is related to the transition linewidth  $\Delta\nu = \Gamma/2\pi$ . If there is no light field present, equation (2.18) simplifies to

$$-i\gamma C_2 = i \frac{dC_2}{dt}, \quad (2.19)$$

which is easily solved to give  $C_2(t) = C_2(t=0)e^{-\gamma t}$ . From the probability of finding the atom in the excited state,  $|C_2(t)|^2$ , it follows that the number of atoms of an ensemble  $N$  in the excited state is  $N_2 = N_2^0 e^{-2\gamma t}$ , and hence  $A_{21} = 2\gamma = \Gamma$ .

Repeating the steps performed on equations (2.7) and (2.8) on this new time evolution equation results in a new set of density matrix elements. Differentiation with respect to time gives

$$\frac{d\rho_{22}}{dt} = -i \frac{\Omega_0^*}{2} e^{-i\delta t} \rho_{12} + i \frac{\Omega_0}{2} e^{i\delta t} \rho_{21} - 2\gamma \rho_{22}, \quad (2.20)$$

$$\frac{d\rho_{11}}{dt} = i \frac{\Omega_0^*}{2} e^{-i\delta t} \rho_{12} - i \frac{\Omega_0}{2} e^{i\delta t} \rho_{21} + 2\gamma \rho_{22}, \quad (2.21)$$

$$\frac{d\rho_{12}}{dt} = i \frac{\Omega_0}{2} e^{i\delta t} (\rho_{11} - \rho_{22}) - \gamma \rho_{12}, \quad (2.22)$$

$$\frac{d\rho_{21}}{dt} = -i \frac{\Omega_0^*}{2} e^{-i\delta t} (\rho_{11} - \rho_{22}) - \gamma \rho_{21}. \quad (2.23)$$

By introducing  $\tilde{\rho}_{12} = \rho_{12} e^{i\delta t}$  and  $\tilde{\rho}_{21} = \rho_{21} e^{-i\delta t}$  the oscillatory terms can be eliminated, and a new set of equations for the time evolution of the populations and coherences arises:

$$\frac{d\rho_{22}}{dt} = -i \frac{\Omega_0^*}{2} \tilde{\rho}_{12} + i \frac{\Omega_0}{2} \tilde{\rho}_{21} - 2\gamma \rho_{22} = -\frac{d\rho_{11}}{dt} \quad (2.24)$$

$$\frac{d\tilde{\rho}_{12}}{dt} = i \frac{\Omega_0}{2} (\rho_{11} - \rho_{22}) - \gamma \tilde{\rho}_{12} - i\delta \tilde{\rho}_{12} = \frac{d\tilde{\rho}_{21}^*}{dt}. \quad (2.25)$$

The steady state solutions to these equations are

$$\rho_{22} = \frac{\frac{1}{4} |\Omega_0|^2}{\delta^2 + \gamma^2 + \frac{1}{2} |\Omega_0|^2}, \text{ and} \quad (2.26)$$

$$\rho_{12} = e^{i\delta t} \frac{\frac{1}{2} \Omega_0 (\delta - i\gamma)}{\delta^2 + \gamma^2 + \frac{1}{2} |\Omega_0|^2}. \quad (2.27)$$

## 2.2.2 Radiation Pressure

The scattering rate is related to the transition linewidth and the upper state population by

$$\gamma_{\text{scatter}} = \Gamma_{12} \rho_{22}. \quad (2.28)$$

During an absorption process the atom feels a force which is related to the momentum transfer:  $\vec{F} = \frac{d\vec{p}}{dt}$ . But this is simply the change in momentum per scattering process, i.e. the momentum of one photon times the number of events per unit time,

$$\vec{F} = \hbar \vec{k}_L \gamma_{\text{scatter}}. \quad (2.29)$$

Substituting equation (2.28) and (2.26) the radiation pressure force is

$$\vec{F} = \frac{1}{2} \hbar \vec{k}_L \Gamma_{12} \frac{|\Omega_0|^2/2}{\delta^2 + \Gamma_{12}^2/4 + 1/2 |\Omega_0|^2}. \quad (2.30)$$

Defining the saturation parameter

$$S = \frac{\Omega_0^2/2}{\delta^2 + \Gamma_{12}^2/4}, \quad (2.31)$$

the expression simplifies to

$$\vec{F} = \frac{1}{2} \hbar \vec{k}_L \Gamma_{12} \cdot \frac{S}{1+S}. \quad (2.32)$$

The resonant Rabi frequency at saturation,  $S = 1$ , is  $\Omega_{\text{Sat}} = \sqrt{2} \Gamma_{12}/2$ . Combined with the definition of the light intensity and the Rabi frequency we can write

$$\frac{I}{I_{\text{Sat}}} = \frac{\Omega_0^2}{\Gamma_{12}^2/2}. \quad (2.33)$$

Substituting into equation (2.30) we arrive at

$$\vec{F} = \frac{1}{2} \hbar \vec{k}_L \Gamma_{12} \left[ \frac{I/I_{\text{Sat}}}{4\delta^2/\Gamma_{12}^2 + 1 + I/I_{\text{Sat}}} \right]. \quad (2.34)$$

If we now consider an atom propagating in the direction of the laser beam with velocity  $v$ , the frequency of the light source appears Doppler shifted to the red in the rest frame of the atom:

$$\omega_{\text{Atom}} = \left(1 - \frac{v}{c}\right) \omega = \omega - k_L v. \quad (2.35)$$

Similarly the net detuning in the rest frame of the atom is given by

$$\delta_{\text{Atom}} = \delta - k_L v. \quad (2.36)$$

We change equation (2.34) accordingly, and use scalar quantities for simplicity. We also know that the force will be in the direction of the laser beam:

$$F_{\pm} = \frac{1}{2} \frac{\hbar}{c} (\omega \mp k_L v) \Gamma_{12} \left[ \frac{I/I_{\text{Sat}}}{4(\delta \mp k_L v)^2 / \Gamma_{12}^2 + 1 + I/I_{\text{Sat}}} \right]. \quad (2.37)$$

$F_{\pm}$  are the forces depending on the positive and negative direction of the laser beam.

For negative detuning the net force is negative for positive atomic velocities and positive for negative atomic velocities, so the atoms are losing energy in the dimension defined by the laser beams regardless of their direction of travel.

Taylor expanding the radiation pressure force around zero let's us approximate  $F \simeq F_0 + \beta v$ , where

$$F_0 = \frac{1}{2} \frac{\hbar \omega \Gamma_{12}}{c} \left[ \frac{I/I_{\text{Sat}}}{4\delta^2 / \Gamma_{12}^2 + 1 + I/I_{\text{Sat}}} \right], \quad (2.38)$$

and

$$\beta = -4\hbar k_L^2 \frac{\delta}{\Gamma_{12}} \frac{I/I_{\text{Sat}}}{(4\delta^2 / \Gamma_{12}^2 + 1 + I/I_{\text{Sat}})^2}. \quad (2.39)$$

It follows that at low temperatures there are two components to the radiation pressure force. The first term,  $F_0$ , is constant and present regardless of the ion's motion. The second term is proportional to the ion's velocity. The one-dimensional motion of the ion subject to such a force can be described by a damped harmonic oscillator. The damping coefficient is then  $\beta$ , and the velocity dependent force reaches its maximum when  $\delta \equiv \Gamma_{12}/2$ .

The ions we cool are confined in the potential well of an ion trap and as such undergo simple harmonic motion. As a result the radiation pressure derived here for a free space atom is not the only force acting on the trapped ion. The ion trap setup does however simplify the experimental setup necessary for efficient cooling greatly in comparison to cooling free atoms. It is possible to use a single laser beam with components in all three axes of ion motion with the ion the being cooled for half of its secular oscillation period. In free space six lasers would be necessary. However, this implies that  $F_0$  is not balanced by a counter-propagating laser beam of equivalent intensity, and this has a constant effect on the ion position within the trap. This effect has implications for our heating rate measurements (chapter 5).

A plot of the radiation force is shown in figure 2.3. The presence of  $F_0$  is shown clearly for both  $F_+$  and  $F_-$ . For illustration purposes  $F_{\text{total}}$  is also shown, the case of two counter-propagating

laser beams of equal intensity for an atom in free space. This curve is symmetric about the origin.

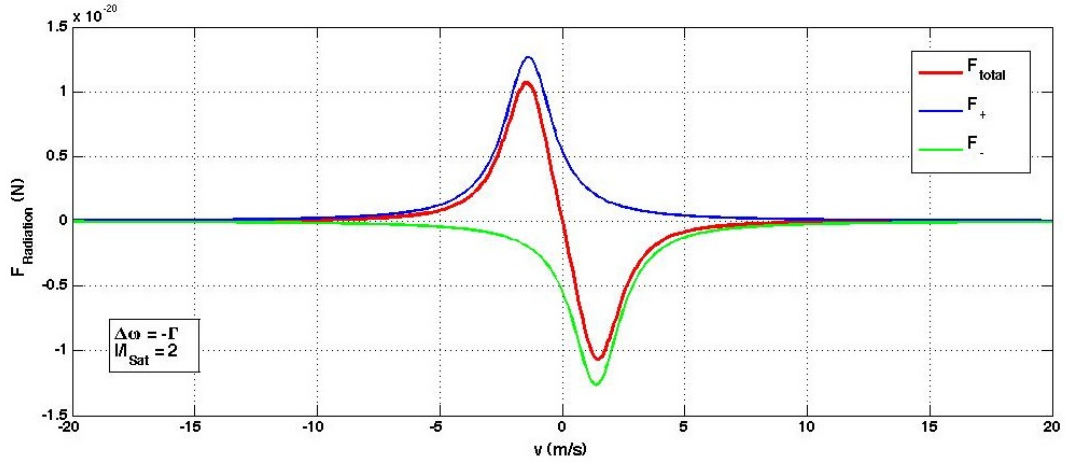


Figure 2.3: The radiation pressure as a function of atomic velocity for a red detuned laser.  $F_+$  and  $F_-$  are the forces for an atom moving towards and away from the laser beam respectively.  $F_{\text{total}}$  is the combination of the two, i.e. the case of two counter-propagating beams.

The net momentum change due to spontaneous emission is zero, but the momentum transfer per individual photon is finite and each emission creates a heating effect by the recoil it produces. The temperatures that can be reached with Doppler cooling is limited by this effect. The limit is defined by the condition that the heating rate,  $R_{\text{Heat}} = \gamma_{\text{Scatter}} \frac{(\hbar k_L)^2}{2m}$ , due to the momentum fluctuations equals the cooling rate,  $R_{\text{Cool}} = \langle Fv \rangle = \beta \langle v^2 \rangle$ . At low laser intensities the Doppler limit can be calculated [24]

$$T = \frac{\hbar \Gamma_{12}}{4k_B} \left( \frac{\Gamma_{12}}{2|\delta|} + \frac{2|\delta|}{\Gamma_{12}} \right). \quad (2.40)$$

As established earlier cooling is the most efficient when  $\delta = -\Gamma_{12}/2$  and hence

$$T_{\text{Doppler}} = \frac{\hbar \Gamma_{12}}{2k_B}. \quad (2.41)$$

The  $4^2S_{1/2} \rightarrow 4^2P_{1/2}$  transition which we use for cooling the trapped calcium ions has a linewidth of 22.3 MHz, which equates to a Doppler limit of 533  $\mu\text{K}$ .

The treatment in this chapter covered a two-level system only. In addition to the cooling transition a calcium ion excited to the  $4^2P_{1/2}$  level also decay into the metastable  $3^2D_{3/2}$  state (lifetime  $\sim 1\text{ s}$ ). These two competing processes occur with ratio of 1:13. Thus efficient cooling requires pumping the population from the  $3^2D_{3/2}$  level back into the cooling cycle. More details on the possible repumping scheme can be found in chapter 4.

## Chapter 3

# Experimental Apparatus

### 3.1 Setup Overview

An ion trap and experimental cavity form the central piece of the experimental setup. They are enclosed within a vacuum chamber. All other components of the experiment, the optics and the detection system are outside of vacuum. Overviews of the specific setups used for each experimental measurement can be found in the corresponding sections of this thesis. In general every experiment was set up with two cooling laser beams for cooling the ions in all three degrees of freedom and establishing micromotion compensation voltages, laser light to facilitate repumping, and two lasers for the photo-ionisation of calcium.

#### Vacuum Chamber

The vacuum chamber is made from stainless steel. The experimental chamber (figure 3.1), which contains the trap and cavity, has four rectangular windows sealed with indium and held in place by atmospheric pressure. The large windows allow very good optical access from all horizontal directions. Vertical access from above is granted via a round flange mounted window. All windows are anti-reflection coated for UV and IR wavelengths.

The experimental chamber is bolted to a cross-shaped structure with 4 CF-40 feed-through flanges. One each is used for the rf, dc and piezo control, ion gauge, and oven current. An ion pump and a sublimation pump are attached below the cross structure. A T-piece branches off towards a gate valve, and the other pumping stages.

To ensure a good vacuum it is necessary to choose components that have low out-gassing rates, and to avoid their contamination. All parts and tools used were cleaned in an ultrasound bath prior to assembly. Once cleaned powder-free Latex gloves were used in handling them. Before experiments began the trap was also baked in situ. Due to the Indium window seals we

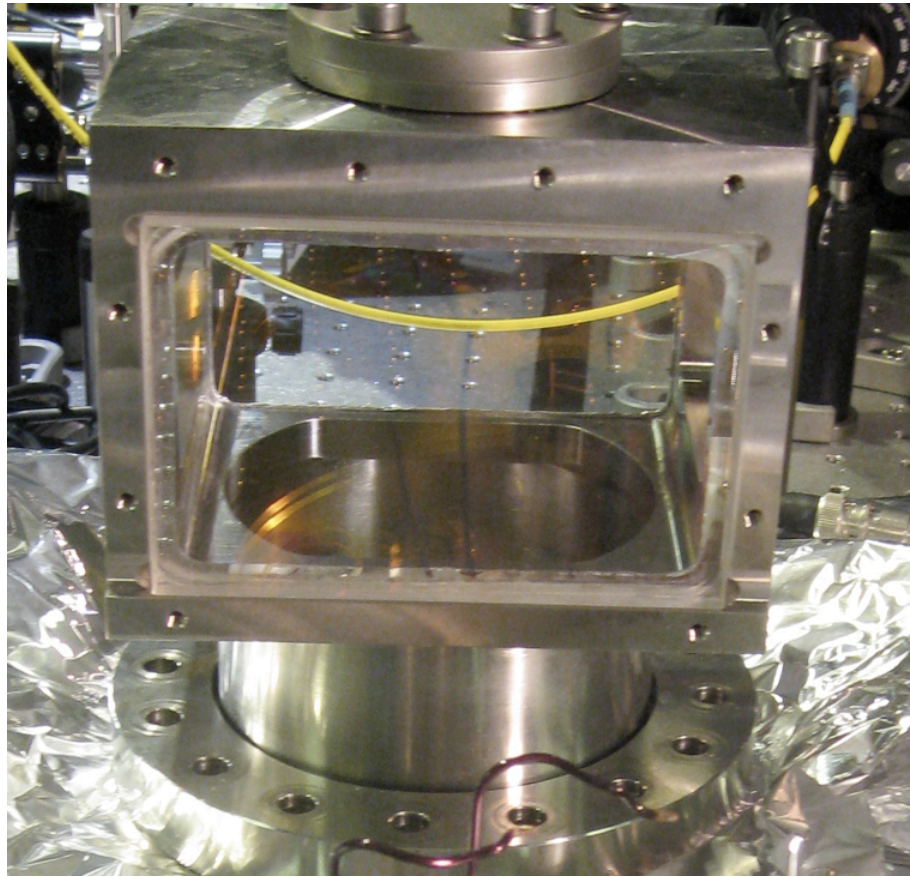


Figure 3.1: A photo showing the experimental chamber.

were restricted in the temperature range (Melting point  $156^{\circ}\text{C}$ ). We baked the chamber for a week at a temperature of  $140^{\circ}\text{C}$ .

### **Vacuum Pump System**

Our experiments require ultra high vacuum (UHV) conditions. High pressure results in background gas molecules colliding with the trapped ions, and thus shorten ion life times in the trap. To achieve a pressure in the low  $10^{-11}$  mbar two stages of pumping are necessary. A schematic of the chamber including the pumping stages can be seen in figure 3.3. The first stage is the roughing pump which achieves  $10^{-3}$  mbar. A turbo molecular pump reduces the pressure further to  $10^{-10}$  mbar. The experimental chamber can be isolated from these pumping stages via a gate valve. An ion gauge measures the pressure close to the experimental chamber. The ion pump and the sublimation pump below the experimental chamber are used to maintain the low pressure within the main experimental chamber once a pressure low enough for efficient trapping has been achieved. Turbo and roughing pump stages can be switched off when the gate valve is closed.

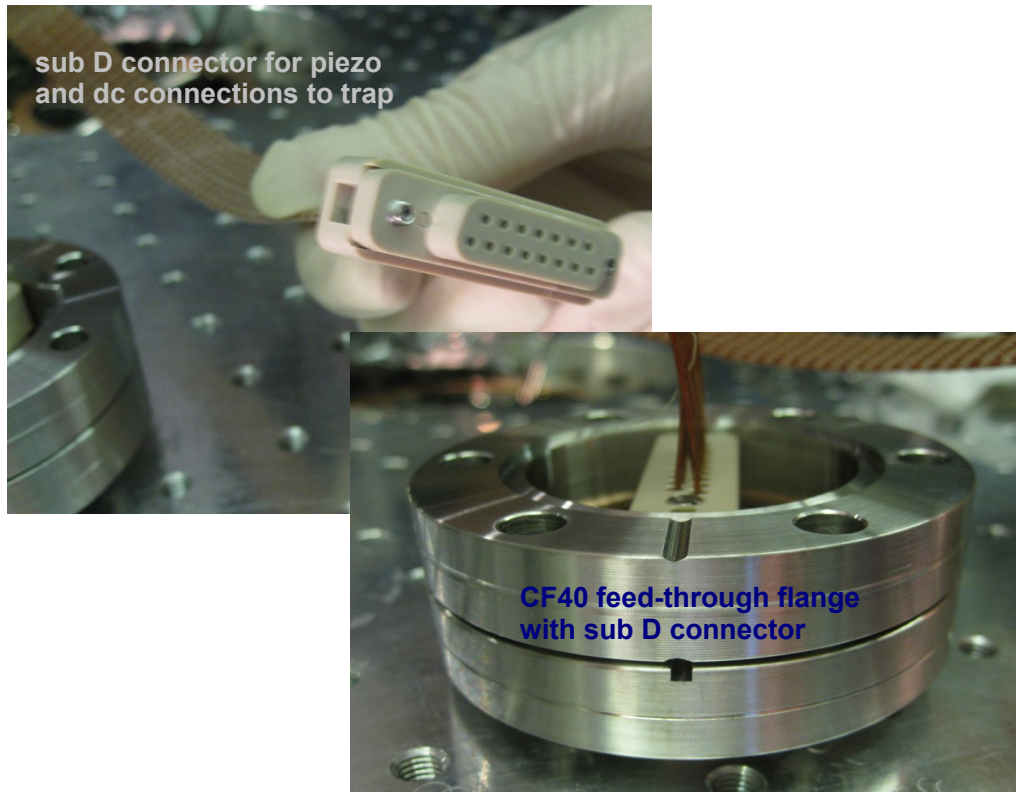


Figure 3.2: The CF40 flange with the sub D connector that is used to supply the the piezo and dc voltages to the trap.

### Calcium oven

The calcium oven is an approximately 2 cm long tantalum tube of 1.02 mm thickness clamped shut at one end. One short tantalum wire each is spot welded to either end of the tube. The tube is filled with grated calcium, and held in place near the trap with a mounting structure made from Macor. Running a current of 1-2 A through the wire and tube causes the oven to heat resistively to a few hundred degree Celsius and eject calcium atoms. The atomic beam passes through a collimator hole before interacting with the two ionisation lasers near the trapping region. The ionisation of neutral calcium is performed first by resonantly exciting neutral calcium from the  $4s^2 \ ^1S_0$  ground-state to the  $4s4p \ ^1P_1$  excited state using a laser at 422 nm and then ionising the atom from this state using 389 nm laser light [25].

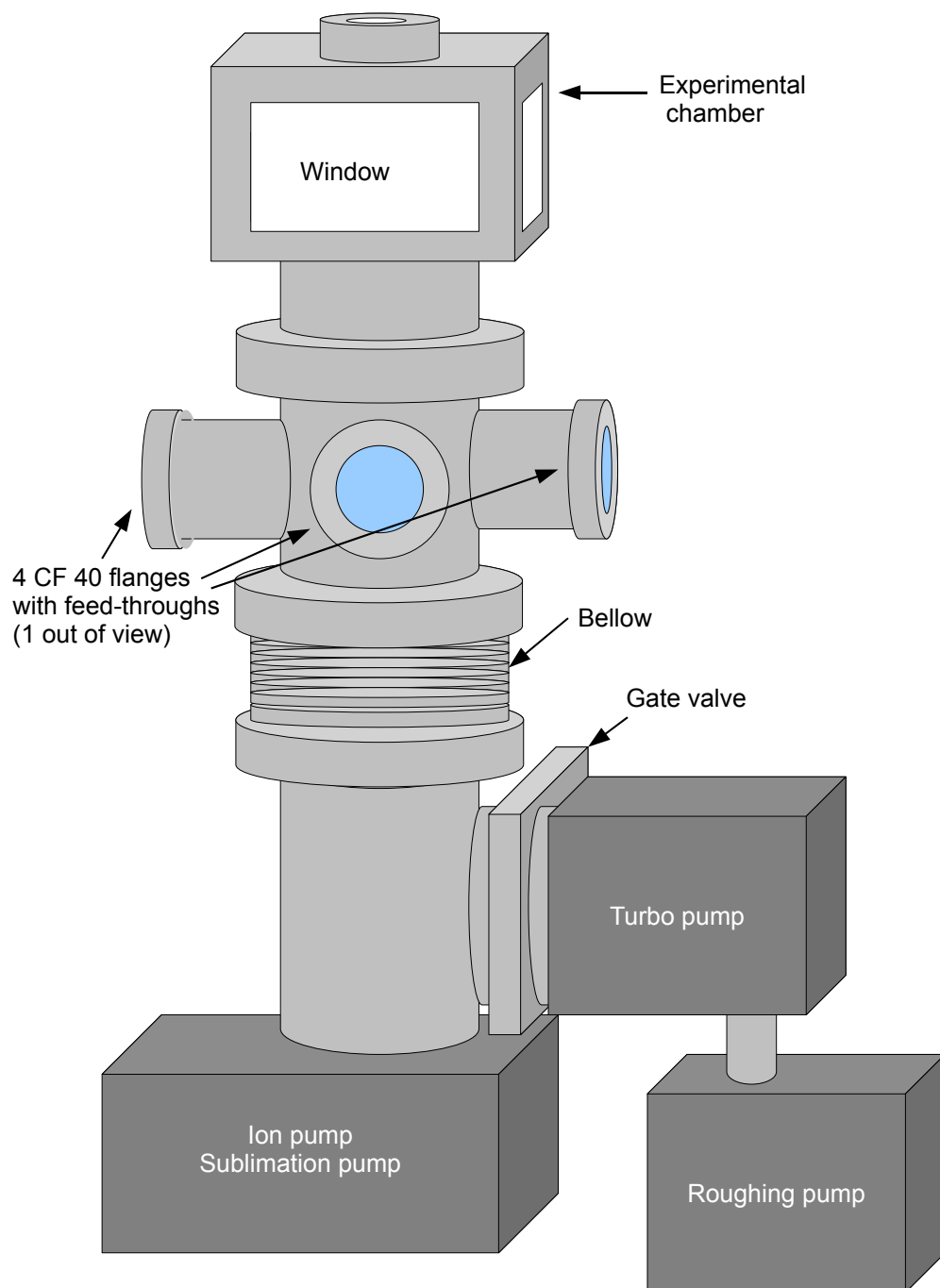


Figure 3.3: A schematic of the vacuum chamber including the arrangement of the pumping stages.

## 3.2 Lasers

Figure 3.4 shows the calcium transitions relevant for our experiments. The 397 nm light for laser-cooling is generated by a commercial frequency doubled laser system (Toptica, SHG

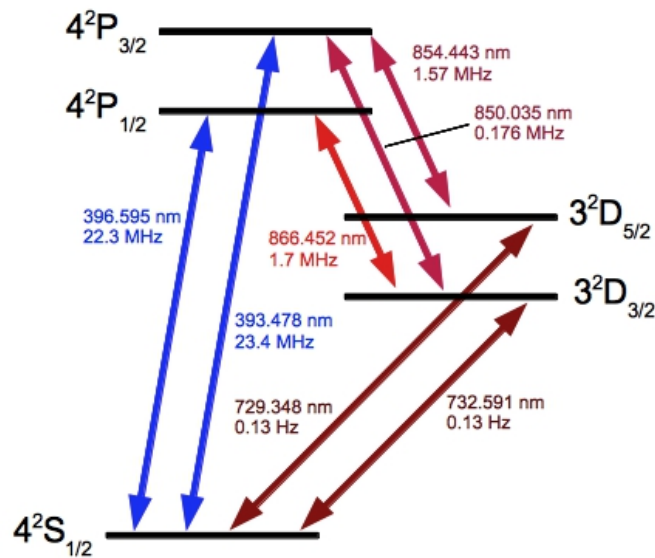


Figure 3.4: A simplified  $^{40}\text{Ca}^+$  level scheme with the transitions relevant to our experiments

110). Its fundamental frequency is stabilised against frequency drifts using a scanning cavity lock which is described in detail elsewhere [26]. For absolute optical frequency reference, the scanning cavity lock utilises a diode laser system at 894.6 nm, locked to a tunable cavity with a Pound-Drever-Hall scheme, which in turn is stabilised to the caesium D1 line using polarisation spectroscopy. The scanning cavity laser lock provides an overall absolute stability of better than 100 kHz at 397 nm.

The 850 nm, 854 nm, and 866 nm repumping lasers, and the 423 nm and 389 nm photo-ionisation lasers are extended cavity diode lasers using a ruled, blazed diffraction grating in the Littrow configuration [27]. They are frequency stabilised through slow feedback from a computer controlled wavelength-meter (High Finesse WS-7).

All laser light is delivered to the vacuum chamber through single-mode polarisation-maintaining optical fibres. Firstly, this is a very convenient method to provide light to different optical tables within the lab. Secondly, the fibres spatially filter the beam so their output is approximately Gaussian.

The cooling laser, the repumper laser, and the first stage ionisation laser are split into several beams. Changing the polarisation of the light using a half wave plate before it passes a polarising beam splitter allows to control the power in each beam. The amount of power within each of the individual beams is controlled using the first order diffracted and retroreflected beam from an acousto-optic modulator (AOM). Within an AOM diffraction occurs as a result of a sound wave traveling through a crystal within the AOM. A voltage controlled oscillator

(VCO) receives an analog voltage between 0 V and 1 V providing an rf voltage to the AOM. Because the sound wave is traveling the light is shifted by the sound wave frequency as it passes through the AOM. In our setup the double pass configuration results in a total shift of 400 MHz. The rise and fall time of the AOMs in use is 10 ns, and the response time 150 ns. Figure 3.5 shows a schematic of our setup.

At the experimental chamber the beams typically pass another lens to focus the beam at the trap centre. This is important to minimise scatter from the trap electrodes, and the increase in intensity at the ion position allows us to work with less overall power in the beams. The repumper beam is overlapped with one of the cooling beams through a long-pass dichroic mirror. We typically use two steering mirrors to align the laser beams with the ion position. To make searching for a first ion fluorescence signal more systematic the final mirror for the combined beams is mounted on a piezo controlled tilting stage. This way we can control the mirror position by providing a voltage to the piezo via digital-to-analog converters (DACs) that are interfaced to a PC.

### 3.3 Detection and Imaging

Figure 3.6 shows a diagram of the imaging system. The ion fluorescence from the cooling transition is collected with Nikon objective lens with a magnification of five which is mounted on a xyz micrometer stage. At the position of the image created by the Nikon lens skimmers eliminate light from outside the focal plane. The signal is then passed through a matched lens pair with a magnification of two, giving a total magnification of ten at the point of detection. A flipper mirror gives the choice of either detecting with an Andor 'Luca' S EMCCD camera or a photomultiplier tube (PMT). The 'Luca' S camera has a chip size of  $658 \times 496$  pixels, and a pixel size of  $10 \mu\text{m}$ . With a 10x total magnification it is thus possible to observe  $658 \mu\text{m}$  of the trapping region in width. The central electrode of the 'alumina' trap is 1 mm wide, so this allows us to observe even large ion strings at a typical ion-ion distance of 22 microns. In the vertical the electrode-electrode distance is much less than the distance we can observe with the camera ( $496 \mu\text{m}$ ). Provided the skimmer is fully opened it is possible to look at the trap electrodes and use its features such as the slits to align the imaging system in the horizontal and vertical. By obtaining a focussed image of the tip of electrode closest to the camera and then moving the objective with the micrometer to half the electrode separation is also possible to pre-align the focus to the ion position before an ion signal is present for optimisation. For both traps the detection system was set up perpendicular to the trap axis. For the 'sandwich' trap the detection system was mounted in the horizontal, while for the 'alumina'

trap is was mounted vertically to look at the trap from above. For measurement purposes we insert a narrow bandpass filter closely to the detection devices to block out light more than 5 nm away from 397 nm. For laser beam alignment purposes it is useful to remove this filter so scatter from all laser beams on the trap electrodes can be observed with the camera.

Fluorescence count rates on the PMT for a single ion at resonance and with laser power at saturation were approximately 3 kHz in our setup.

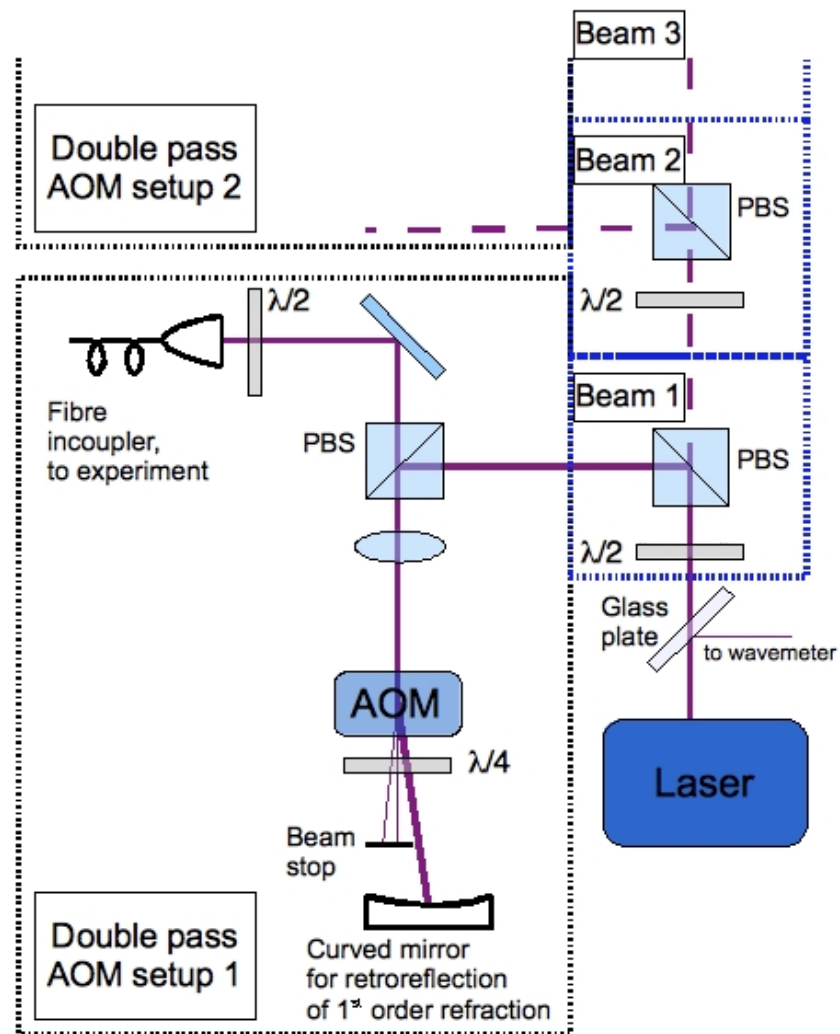


Figure 3.5: A diagram showing the splitting of the laser power into several beams. Double pass AOM setups allow us to control the intensity of each beam as well as switch them off via electronic control. The frequency shift due to diffraction is 400 MHz.

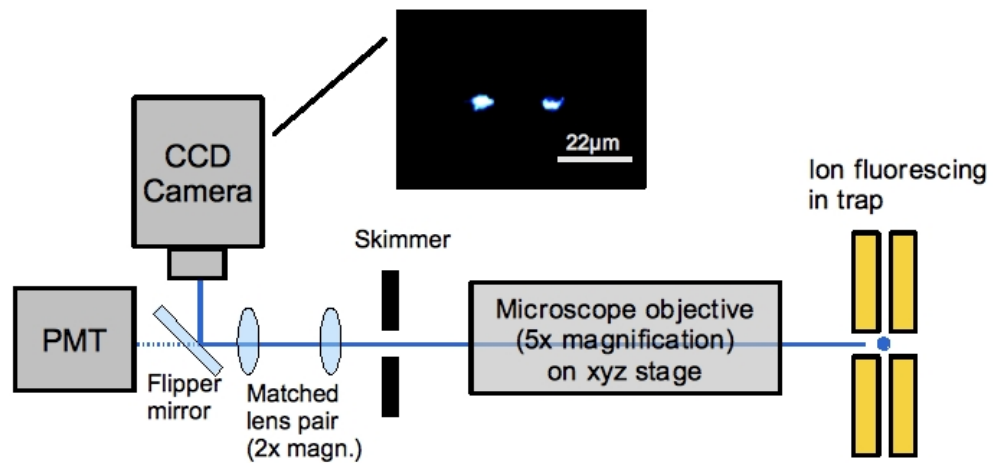


Figure 3.6: The trap imaging system. A 5x magnification microscope objective collects fluorescence from the trapping region, producing an image at the skimmer. This helps to cut out stray light from outside the focal plane. A matched lens pair then images this image onto either a CCD camera or a PMT depending on whether the flipper mirror is in place or not.

## 3.4 The Ion Traps

The experiments reported on in this thesis used two different linear Paul traps. Both traps have scales of the order of hundreds of microns and their development was based on the linear traps used at the MPQ in Garching. In previous experiments when reducing the mode volume of the cavity the dielectric material of the mirrors perturbed the trapping fields and resulted in ion loss [28]. In order to reduce the overlap between the electric rf-field and the cavity mirrors, a small trap with a well-confined rf-field is required, which fits between two closely spaced mirrors. This is the reason for designing a trapping structure with ultra-thin electrodes, carefully designed to be suitable for strongly coupled cavity-QED experiments with trapped ions. Unlike other traps of this order of magnitude neither of the two traps are microfabricated, they have been assembled manually.

### 3.4.1 The 'Sandwich' Trap

The design of this trap is based on a linear ion trap as described in reference [29]. Perpendicular to the trap axis, the ions are confined by an rf-potential applied to four electrodes. The desired small thickness of the trap is achieved by using thin metal sheets made from highly conductive oxygen free (HCOF) copper with thickness of  $125\ \mu\text{m}$ . To confine the ions along the trap axis, dc-electrodes at positive potential are located between the rf-electrodes (see figure 3.7.) They are also made from HCOF copper sheet with a thickness of  $100\ \mu\text{m}$  and a width of 1 mm. The layers are insulated from one another by a  $75\ \mu\text{m}$  thick Kapton foil. In order to avoid dielectric material in the close vicinity of the ions, the Kapton foil is recessed by 1mm from the trapping region. There are 8 dc-electrodes along the trap axis with a separation of 1.5 mm, forming 7 trapping zones between adjacent electrode pairs (separation 1 mm). The total distance between the rf-electrodes is  $250\ \mu\text{m}$  and the entire stack of electrodes is  $500\ \mu\text{m}$  thick, so that it can be fitted inside an optical cavity of  $500\ \mu\text{m}$  length. Sandwiching the different layers leads to a high mechanical stability of the structure.

#### Assembly

Even though the numerical simulations have shown that the trap design is robust against misalignment of the electrodes, great care has been taken to optimise alignment of the dc-electrodes. Instead of inserting the dc-electrodes separately in between the rf-electrodes, the set of 8 dc-electrodes have been machined out of one copper sheet with all electrodes still being interconnected in a stable comb structure. The entire trap is assembled by staggering the electrode layers together and aligning this electrode sandwich by pushing the layers against

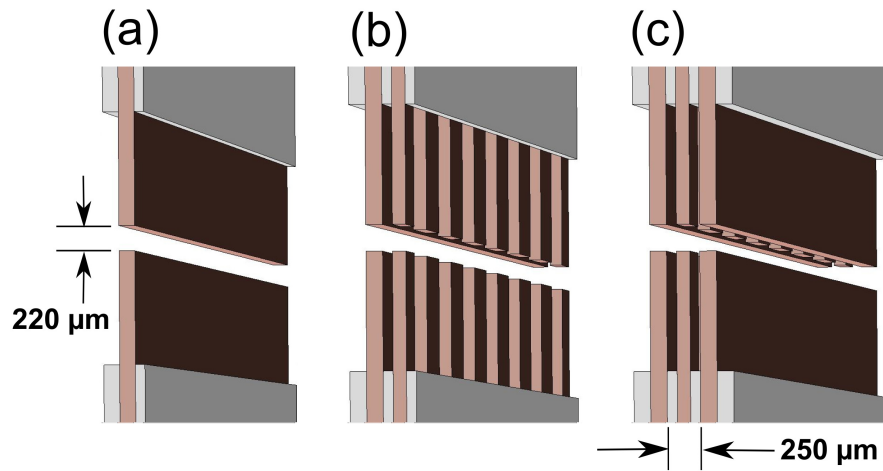


Figure 3.7: Drawings of the trap electrodes (brown) and the Kapton foil (grey) incrementally showing the different electrode layers. Figure (a) shows the rf-electrodes at one side. The vertical spacing between the electrodes is  $220\ \mu\text{m}$ . The copper foil strips used for axial ion confinement are added in in figure (b). In between each pair of neighbouring electrode strips is a separate ion trapping zone. In figure (c) the remaining two rf-electrodes have been added to show the full electrode structure.

a mechanical stop. Two of these electrode assemblies are mounted opposite each other, forming an rf-trap with a vertical electrode separation of  $220\ \mu\text{m}$ . This is warranted by temporarily inserting a mechanical stop of the appropriate thickness. The assembly is then clamped together by a Kapton insulated metal clamp as shown in Fig. 3.8. The alignment is controlled using a microscope. After the trap has been assembled and clamped together, the dc-electrodes are separated by removing the connecting bridge. With the design of the trap electrodes and the alignment procedure, the separation of upper and lower part of the trap is constant to better than  $10\ \mu\text{m}$  over the entire trap length of the trap (20 mm). The transverse spacing of the electrode layers is constant to within  $3\ \mu\text{m}$ . The machining of the thin metal foils for the trap construction must not exert any force on the foil in order to avoid deformation of the electrodes. For this reason, we have employed wire eroding. However, the surface quality of the machined parts of about  $10\ \mu\text{m}$  rms is worse compared to standard milling which may give rise to an increased heating rate [30].

### Electronic Connections

An rf-generator resonantly drives an LC-circuit containing the trap electrodes, supplying them with up to 100 V at a frequency of 22.68 MHz. The rf-voltage is applied to two diagonally opposed rf-electrodes with the other two electrodes kept at rf-ground. Dc-voltages for confinement of the ions along the trap axis are controlled by computer using a D/A-card. In order to suppress rf pick-up, the dc-electrodes are grounded through capacitors which are

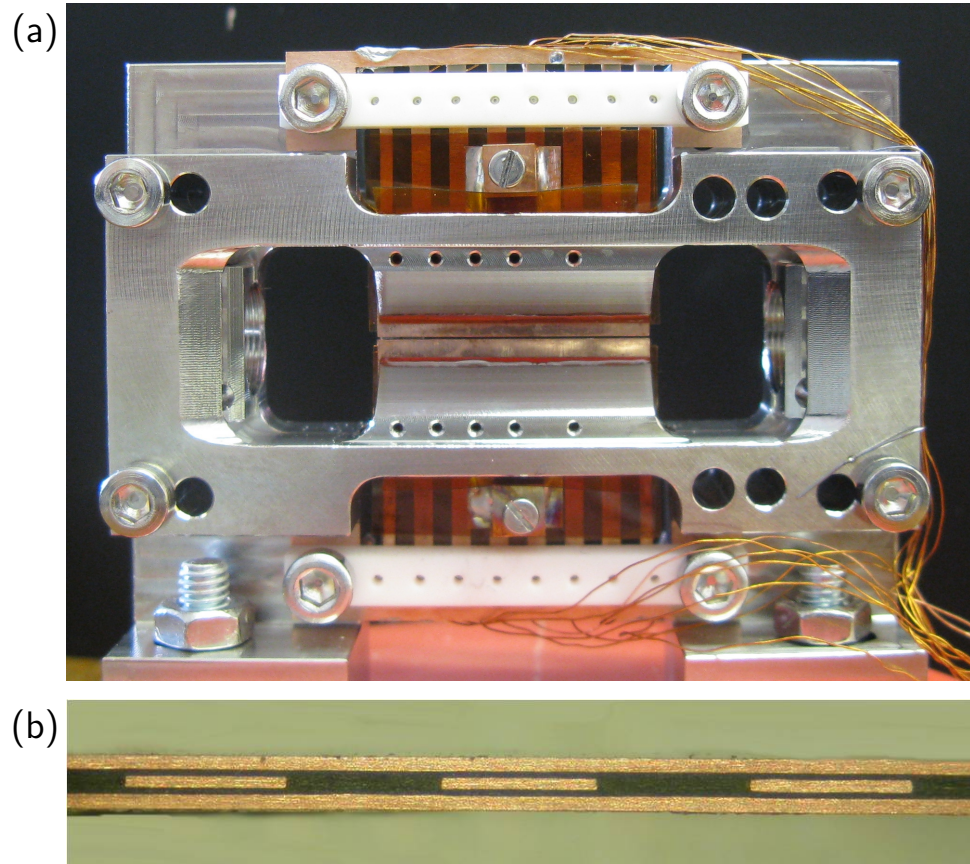


Figure 3.8: (a) Photograph of the trap assembly from the side, showing the narrow slit between the electrodes. At the upper and lower edge, the electrical connectors are visible. (b) Top view of the lower electrode assembly, showing three dc-electrodes in the central layer, sandwiched between the two rf-electrodes.

soldered directly to the electrodes. An important issue in ion traps are radial stray electric fields, which push the ions off the rf-field minimum, making them undergo a driven motion at the rf-frequency (micromotion, see chapter 1). To avoid this, any dc-fields perpendicular to the trap axis are carefully compensated by adding dc-voltages to the rf-electrodes through RC-circuits. Each of the four dc-offsets is controlled individually through the D/A-card.

### Trap Characteristics - Simulations

We have characterised the performance of the trap by numerically calculating the trapping potentials with a finite element code (FEMLAB). FEMLAB calculates the static electrode potentials at the intersection points of a mesh spanning across the space between the electrodes. By using the pseudopotential approximation discussed in chapter 1.4 it is possible to calculate the trap potentials. The pseudopotential, which determines the motion of the ion in the plane perpendicular to the trap axis, is shown in Fig. 3.9 for typical experimental parameters. By substituting the expression for  $q$  (equation (1.17)) and setting  $\alpha = 0$  the fundamental secular

frequency of an ion-trap (equation (1.22)) can be expressed as

$$\omega_r = \eta \frac{eU_{AC}}{\sqrt{2}m\Omega_{RF}r_0^2}. \quad (3.1)$$

Here  $e$  and  $m$  are the charge and mass of the ion,  $U_{AC}$  is the amplitude of the potential applied to the rf-electrodes,  $\Omega_{RF}$  is the rf-frequency and  $r_0$  is the shortest distance between the ion and the electrode ( $166 \mu\text{m}$  in our case). In order to quantify the deviation of the radial trapping potential from an ideal quadrupole potential, the trap efficiency  $\eta$  is employed, specifying the ratio of the actual secular frequency and the secular frequency in a corresponding ideal quadrupole trap with symmetric parabolic electrodes. The numerically obtained trap efficiency for our geometry is  $\eta = 0.75$ .

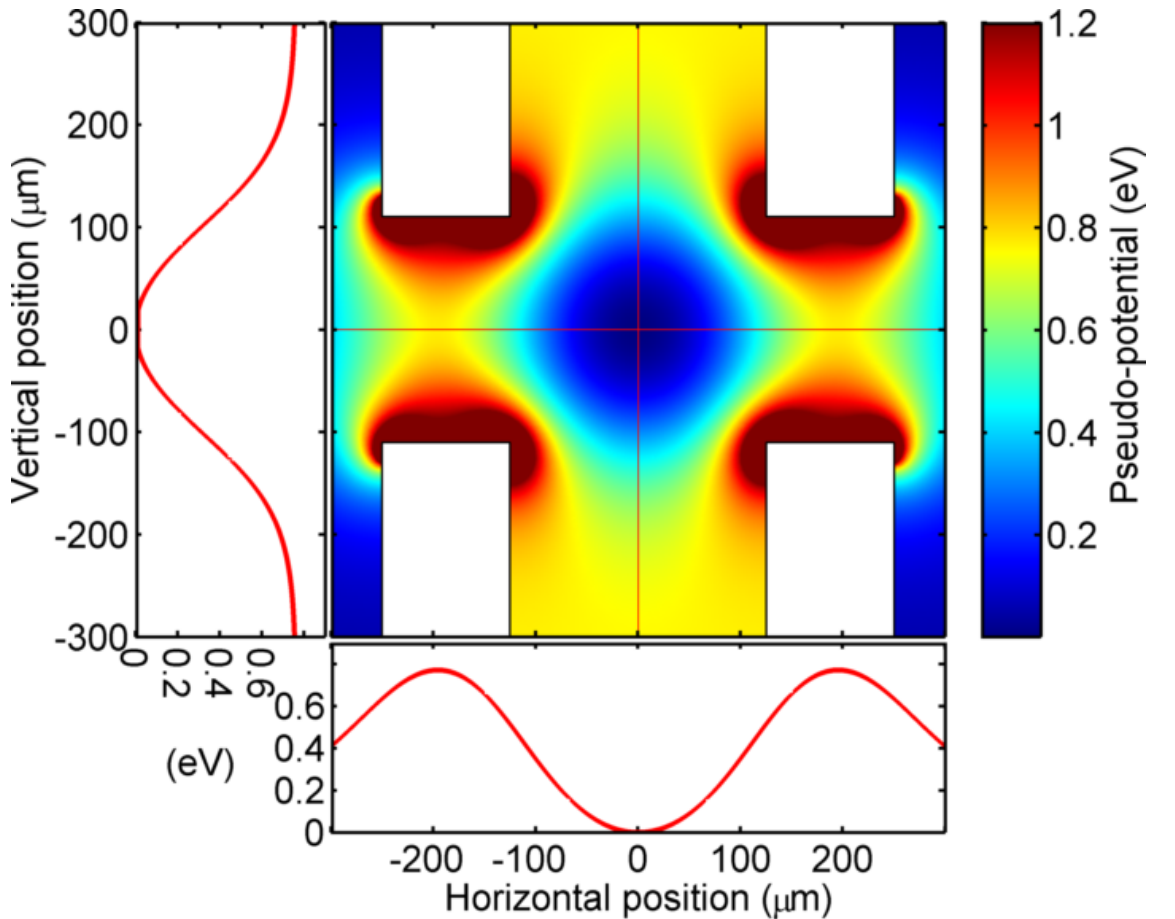


Figure 3.9: Radial cross-section of the pseudo-potential of the linear trap in the at the trap center for  $U_{AC} = 20 \text{ V}$ , obtained from a finite element calculation by averaging the potential over one rf-cycle. Profiles of the pseudo-potential in the vertical and horizontal direction are shown at the edge of the two-dimensional plot.

The anharmonicity of the ponderomotive potential can be characterised by decomposing the potential in a Taylor expansion and comparing the amplitudes with the harmonic term. These ratios perpendicular to the electrode plane (horizontal,  $x$ ) and parallel to the electrode

radial (x) confinement	radial (y) confinement	axial confinement
$C_4 r^2/C_2 = 7 \cdot 10^{-4}$	$C_4 r^2/C_2 = 6 \cdot 10^{-4}$	$C_4 z^2/C_2 = 9 \cdot 10^{-4}$
$C_6 r^4/C_2 = 8 \cdot 10^{-6}$	$C_6 r^4/C_2 = -7 \cdot 10^{-6}$	$C_6 z^4/C_2 = 3 \cdot 10^{-7}$
$C_8 r^6/C_2 = -8 \cdot 10^{-9}$	$C_8 r^6/C_2 = -2 \cdot 10^{-8}$	$C_8 z^2/C_2 = 1 \cdot 10^{-10}$

Table 3.1: Relative size of anharmonic contributions to the radial ponderomotive (rf) and axial (dc) confinement.  $C_n$  is the coefficient of the  $n$ -th term in the Taylor expansion of the pseudopotential or potential. The anharmonicity in each direction was evaluated at a distance  $r_0 = 10 \mu\text{m}$  and  $z_0 = 10 \mu\text{m}$ , corresponding to the scale of a two-ion crystal in the axial direction for our experimental parameters.

plane (vertical,  $y$ ) are summarised in table 3.1.

Similarly, we have analysed the axial confinement and compared it with an ideal harmonic potential. From the harmonic term of the Taylor expansion the confinement strength can be derived to be  $120 \text{ kHz} \sqrt{U_{\text{DC}}}$ , which is in agreement with our measurement.

An important issue for use of the trap in conjunction with a transverse optical cavity is the influence of the dielectric mirrors on the trapping potential. We have numerically determined the pseudopotential in the presence of mirrors with  $\epsilon_r = 3.75$  at the minimum separation of  $500 \mu\text{m}$ . The resulting change in the radial frequency was 0.5% compared to the case without mirrors. This confirms that the trap meets the design criterion of resilience against dielectric materials in close proximity to the trap.

### Trap Characteristics - Measurements

By applying a small modulation voltage to one of the rf-electrodes or one dc-electrode it is possible to probe the confining potential of the ion trap. Observing a dip in the fluorescence of the ions while scanning of the modulation frequency indicates a motional resonance of the trap. Using this method for different amplitudes  $U_{\text{AC}}$  of the rf-voltage, we found that stable trapping is obtained for radial secular frequencies in the range of  $\nu_r = 0.8 - 5 \text{ MHz}$ . For weaker radial confinement, the trapping time as well as loading efficiency is decreased.

In the experiments presented in this thesis that use the 'sandwich' trap, a radial secular frequency of  $\nu_r = 1.5 \text{ MHz}$  was chosen, corresponding to an rf-drive amplitude  $V_{\text{ac}} = 14.5 \text{ V}$ . Axial confinement of the ion between two adjacent electrode strips (see Fig. 3.7 (b)) is obtained by applying a positive bias potential of  $20 \text{ V}$  to the strips, resulting in an axial trapping frequency of  $575 \text{ kHz}$ .

### 3.4.2 The 'Alumina' Trap

This trap was designed as a replacement of the 'sandwich' trap. To use the 'sandwich' trap for cavity QED experiments the ions have to be shuttled from the production to the experimental region. This mechanism had been employed successfully with the larger scale trap in Garching that the design of the 'sandwich' trap was based on and is commonly used as a precaution to avoid coating the cavity mirrors with a layer of calcium as the hot atoms escape the oven. The simplest approach to move an ion from one trapping region (Figure 3.7) to another is to temporarily set the voltage between the two trapping regions to 0V and then return it to its previous value. Using this method we attempted to shuttle ions to the region next to the production region in the 'sandwich' trap. A variety of different trapping parameters were tried and the trap regions observed with the camera. Unfortunately this was unsuccessful and the ions were usually lost during these attempts. Suspecting that the switching of voltages manually was neither precise nor fast enough, we built some fast switching circuitry. We also used a programmable function generator to be able to more precisely control the timing of the switching and its relative phase to the ions' secular motion. Again, these attempts were not successful. Finally, we suspected another possible source of the problem in the inhomogeneity in the trapping potential due to the surface quality of the electrodes and their alignment relative to one another. This may have resulted in the net potential at the position of the dc electrode separating the regions when this electrode is set to 0V not being zero and therefore preventing the ions from crossing over into the second trapping region. If this was the case then it was possible that the ions' energy was not enough to cross the remaining potential barrier. To test this we tried two things. Firstly we added a driving period to the switching protocol to excite the ion at the secular resonance frequency. Secondly we temporarily applied negative dc voltages to the separating electrode before switching it to 0V and then back to its original value. Again, we failed to record an ion signal in the second trapping region.

We concluded that for traps of micrometer scale any additional steps necessary to arrive at an ion cavity system that can be used for experiments should be eliminated. This was one of the key considerations for the design of the 'alumina' trap. In contrast to the 'sandwich' trap, where the oven was mounted parallel to the cavity mirror position (perpendicular to the trap axis), in the 'alumina' trap it sits below the trap subtending an angle of approximately  $45^\circ$  with both the trap (z) axis and the y axis (see figure 3.12). The oven is currently placed on the Macor base such that its opening is 5 mm from the collimator hole which measures  $200\ \mu\text{m}$ . The inner diameter of the tantalum tube used to construct the oven is  $860\ \mu\text{m}$ . This setup and the resulting angular distribution of the atom flux are shown in figure 3.10. Only atoms

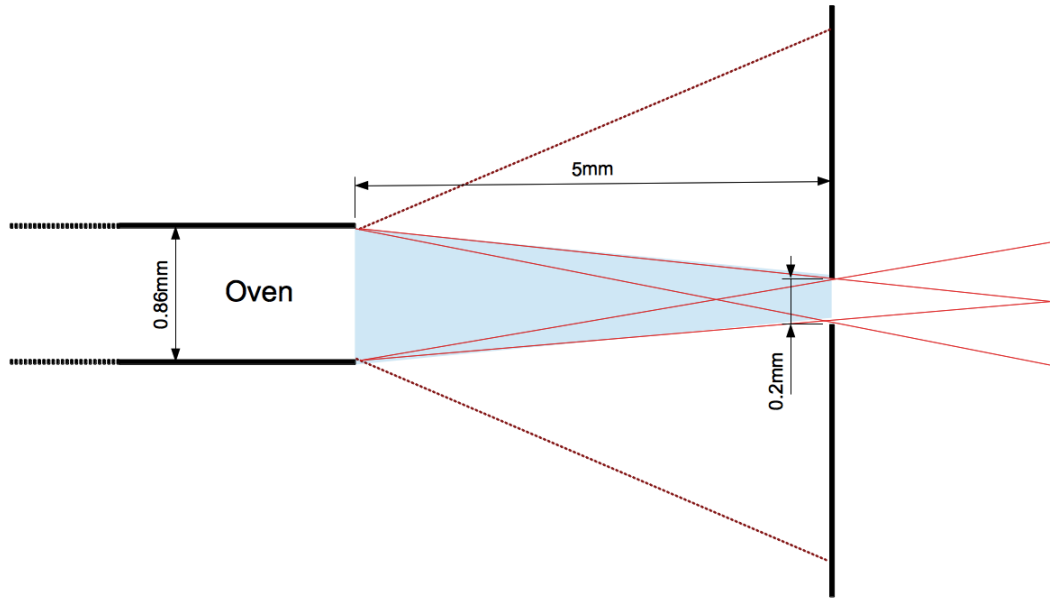


Figure 3.10: A diagram showing the dimensions of the oven aperture, distance between oven aperture and collimator and collimator size of the current setup

from the front of the oven will escape from the aperture as during assembly the oven was filled almost to the edge with calcium, so it is safe to assume that the volume of mobile calcium atoms is restricted to the first few millimetres of the tube only. The angular distribution of the atom flux is proportional to  $\cos \alpha$  where  $\alpha$  is the angle of emergence. For our current oven diameter this results in an angle of approximately  $25^\circ$ . The diameter of the atomic beam at a distance  $l$  behind the collimator coming from an oven with an aperture of diameter  $b_1$  combined with a collimator with a hole of diameter  $b_2$  placed in front of the oven aperture at a distance  $a$  is given in [31] as

$$d = 2 \left( (a + l) f - \frac{b_1}{2} \right), \quad (3.2)$$

where  $f = \left( \frac{b_1/2 + b_2/2}{a} \right)$ . The collimator is 15 mm from the trap centre, which results in a beam diameter of 3.4 mm in the current setup. This is just marginally smaller than the mirror separation. It is obvious that a beam of this width cannot be used once the cavity length is reduced to the intended  $500 \mu\text{m}$ . A beam width of  $400 \mu\text{m}$  can be achieved by halving the size of the pinhole, reducing the oven aperture to 0.2 mm and increasing the distance between oven and collimator from 5 to 15 mm. While this will decrease the solid angle of the atom distribution, it will also decrease the flux of atoms through the trap centre. However, in the current setup producing and trapping ions is quick, so this modification is likely to slow down

the process but not stop it.

### Components

The trap electrode substrates (figure 3.11) are made from alumina ceramic of 0.5 mm thickness which were laser cut to form the 2D shape of the electrodes. The electrodes themselves consists of a thin gold coating (a few  $\mu\text{m}$ ) on both sides of the substrate. The electrodes extend 5 mm from the base of the substrate, and are 6 mm in width, with the tip a knife edge with an angle of  $20^\circ$ . The knife edge was chosen to gain better optical access to the trap centre, but posed difficulties during the mechanical machining process used due to the alumina being prone to chipping.

Two types of these ceramic blades were made. One type is a single blade with only one

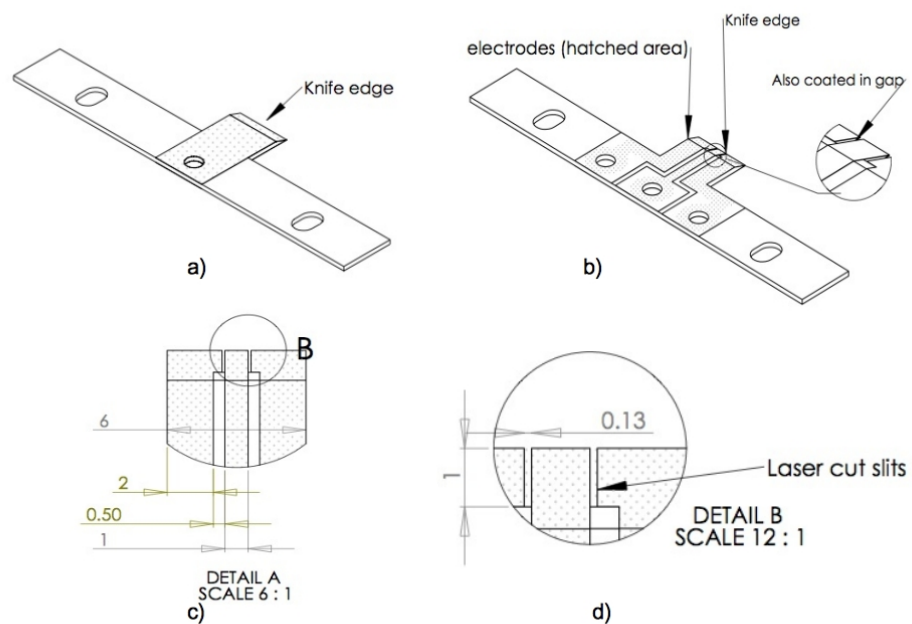


Figure 3.11: Drawings of the trap electrodes. The dotted area represents the gold coating. a) Shows the an rf- electrode without slits. b) Shows a slitted electrode, the centre electrode is the rf-ground electrode, while the two outer electrode are used for axial confinement. c) shows the slitted electrode in more detail including the dimensions in mm. d) shows the laser cut slits at the electrode tip.

electrode (see figure 3.11a) ). This type is used to apply the rf trapping potential. The other type is divided into three regions by 0.5 mm wide gaps in the gold coating along the depth of the electrode, and laser cut slits of width 0.13 mm in the electrode tip (see figure 3.11b) - d) ). The centre electrode is 1 mm wide from tip to base. The two outer electrodes measure

2 mm at the base but widen to 2.37 mm at the tip where they are separated from the centre electrode by the laser cut slits. Of the resulting three electrodes the outer two are used for the axial confinement while the inner electrode is the rf-ground electrode.

### Assembly

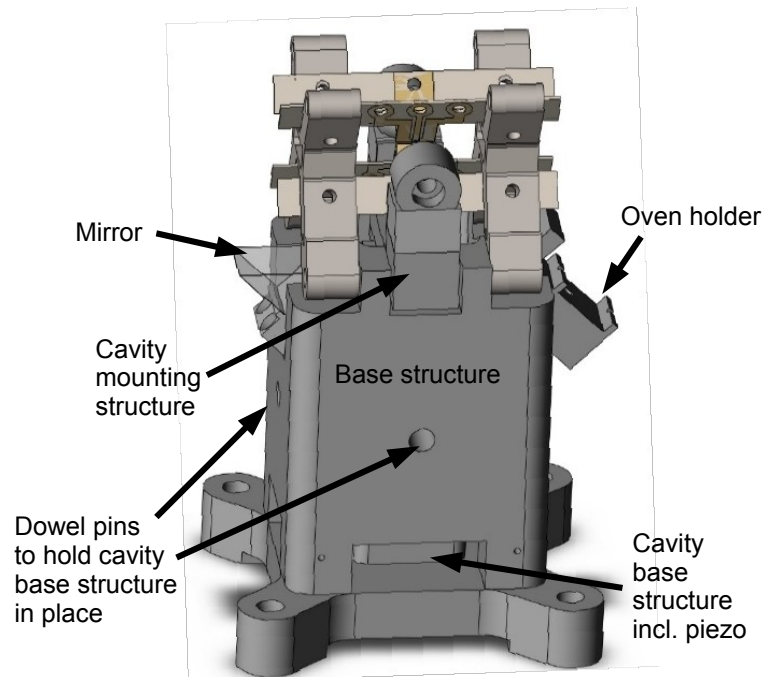


Figure 3.12: The solid works assembly of the alumina trap structure.

A hollow stainless steel block made using a combination of conventional machining techniques and wire eroding forms the base of the trap structure (figure 3.12). The experimental cavity mounting structure is integrated within the trap assembly. The vertical rectangular hole inside the base structure houses the cavity's base structure (figure 3.13) with a piezo that allows 50  $\mu\text{m}$  of vertical travel of the cavity with respect to the trap. It is held in place with two dowel pins. The mounting structure for the cavity mirrors was then glued on top of the vertical piezo. The mirror holders were glued on top of two shear piezos (PI PICA<sup>TM</sup>P-141.05), which in turn were glued on top of the cavity mounting structure. Two non-magnetic stainless steel x-shaped mounting brackets (figure 3.14) that have been wire eroded out of one piece of metal, and were only cut into two as the last manufacturing step to assure symmetry provide the support for the electrode substrates and were bolted to the side of the base block. To

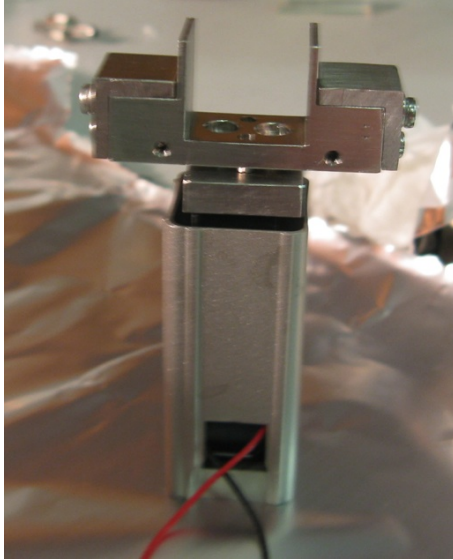


Figure 3.13: The cavity base structure which houses the piezo for vertical adjustment of the cavity with respect to the trap including the cavity mounting structure on top of the piezo. The shear piezos for varying the cavity length and the mirror holders are yet to be mounted.

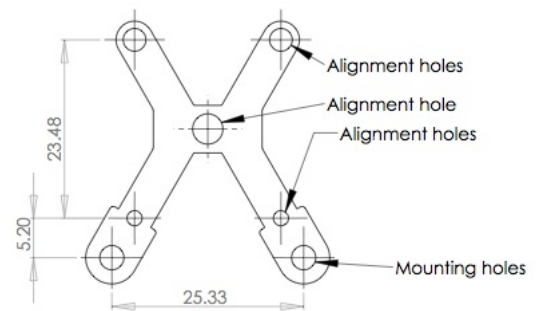


Figure 3.14: A drawing of the x-shaped stainless steel mounting structure for the 'alumina' electrodes.

assure accurate alignment of the trap and cavity axes custom brass tools were made. Figure 3.15 shows the set of tools used to precisely align the electrode mounting brackets and the mirror holders. Figure 3.16 shows them in use during trap assembly.

The final step was to mount the electrodes on the structure. Another set custom made tool was used for this. One cross shaped piece (figure 3.15) each was mounted on either side of each mounting bracket using the alignment holes to provide an accurate reference for the electrode substrates. The electrodes were then bolted to the mounting brackets, and the reference tools removed. The final alignment was done with a microscope and the electrodes moved one at a time until they were aligned to about  $10\ \mu\text{m}$  precision. The aim was to have an ion to electrode distance of  $170\ \mu\text{m}$ . Microscope pictures of the final setup show the ion electrode distance to be roughly  $200\ \mu\text{m}$  (figures 3.17 and 3.18). A picture of the assembled trap can be seen in figure 3.19.

### Electronic Connections

The electrical connections for the axial dc and the rf-ground are made via thin copper sheet (0.125 mm thickness) and screws that fit through the holes in the blades. Thin copper wires are soldered to these copper sheets and connect to a vacuum compatible sub D connector mounted on the base of the mounting structure. A slightly thicker copper foil structure

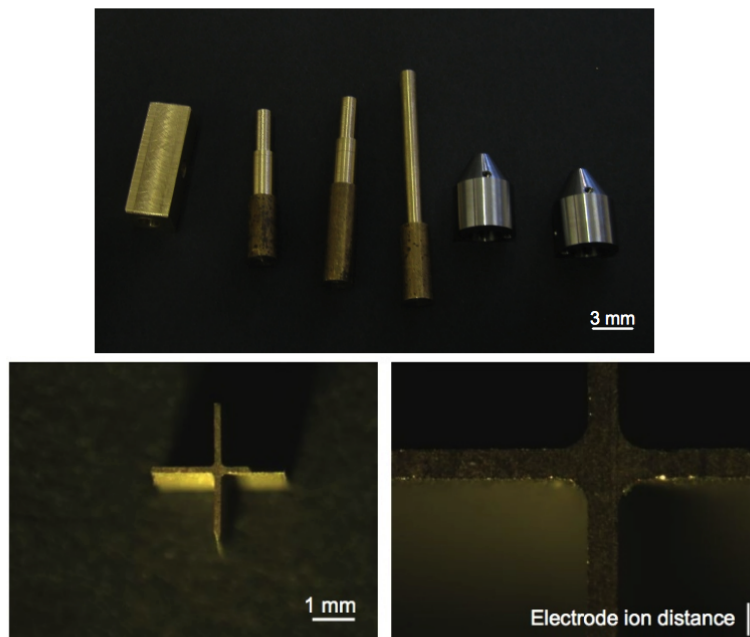


Figure 3.15: The first photo shows the custom brass tools used to assure precise alignment of the x mounting brackets, and the cavity mirror holders. The second two photos show the tool for aligning the electrodes with respect to one another.

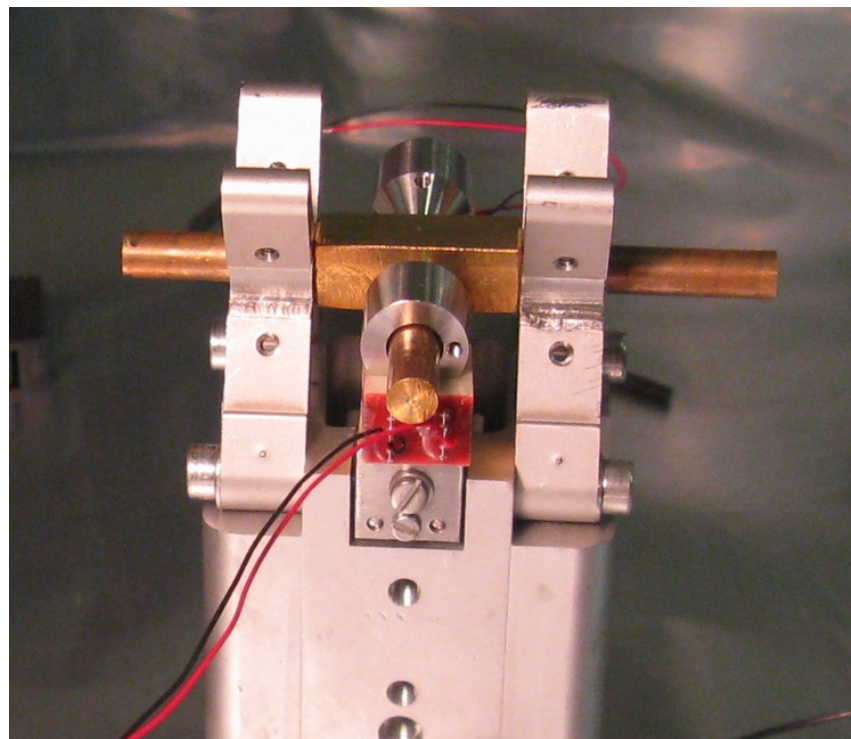


Figure 3.16: Aligning the electrode mounting brackets and the mirror holders during the trap assembly.

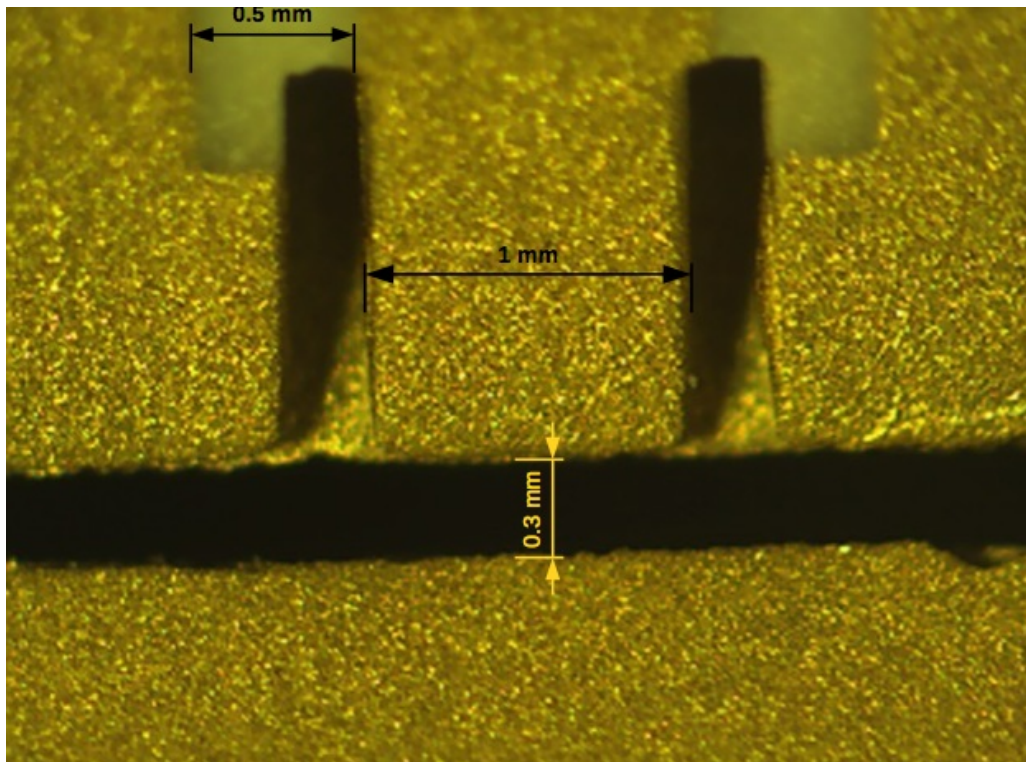


Figure 3.17: A close up of the electrodes under the microscope including the electrode - electrode distance as estimated using known electrode dimensions from the side.

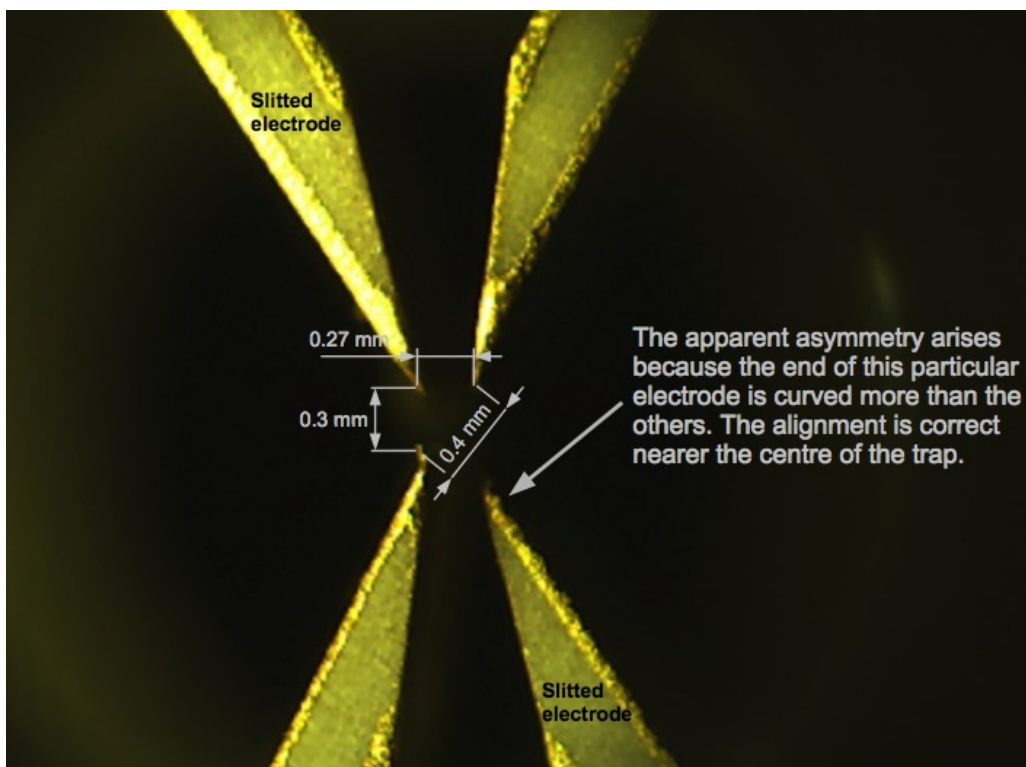


Figure 3.18: I

A close up of the electrodes under the microscope including the electrode - electrode distance as estimated using known electrode dimensions facing along the trap axis.

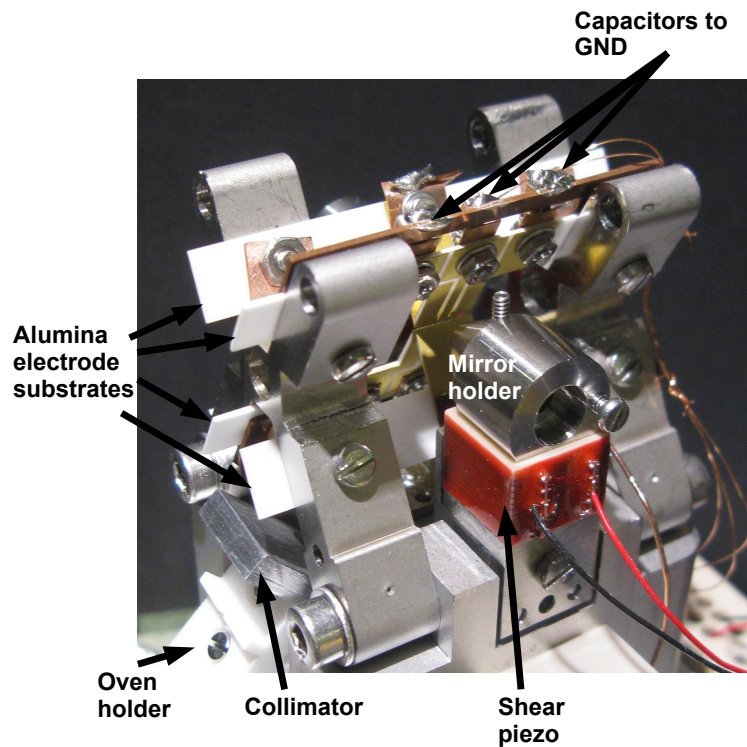


Figure 3.19: The fully assembled trap without cavity mirrors.

(0.5 mm thickness) is mounted close to either of the slitted blades, and bolted directly to the x-shaped mounts, which are connected to ground via the base structure. The three electrode of each slitted blade are then connected to this foil via capacitors to avoid rf pick up. A sub D connector cable extends from one of the vacuum chamber's feedthroughs up to the side of the trap. All dc, ground and piezo electrical connections are crimped to the pins of this connector. As a result de-installation of the trap is greatly simplified. Figure 3.20 shows the electric connections to the trap. The rf connections are made via separate barrel connectors that are mounted to side of the trap base structure. The rf voltage is supplied via separate feedthrough utilising significantly thicker copper wires. Only one wire is connected through the feedthrough. Using a barrel connector the supply is then split immediately below the trap base structure, and connected to the side mounted barrel connectors. This helps to ensure that both rf feed wires are of the same length and hence the capacitance of the trap is symmetric.

To compensate the micromotion in this trap, a dc voltage can be supplied to the rf-ground electrodes, as well as the mirror holders.

All dc supplied to the trap comes from a D/A-card. The rf frequency is provided by a resonance autotransformer circuit (figure 3.21). The primary resonance circuit consists of the

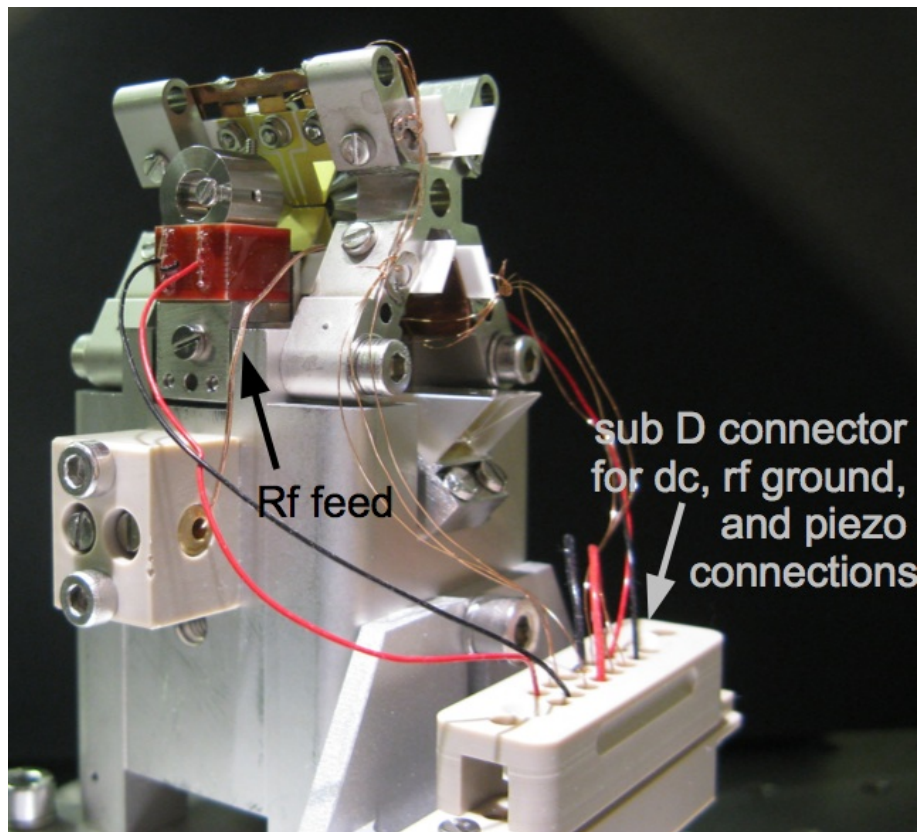


Figure 3.20: The electronic signals supplied to the trap and piezos are all connected via a sub D connector, apart from the rf potential.

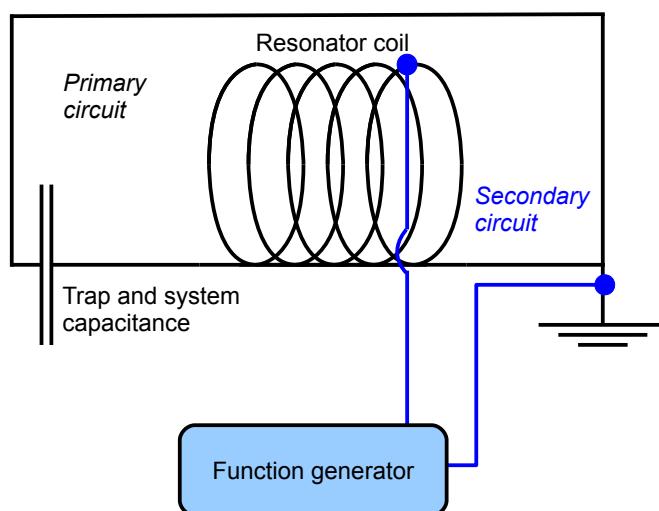


Figure 3.21: Circuit diagram of the autotransformer that supplies the rf to the trap electrodes.

resonator coil and the system's capacitance. In an ideal setup this capacitance would be the trap capacitance alone. However, because this is a very small capacitance the capacitances of the wires leading to the trap are not negligible in comparison. The total capacitance of the system was established to be approximately 12 pF. This was done by replacing the trap and system in the circuit by capacitors of known value until a match in resonance frequency was found. The secondary circuit consists of a part of the resonator coil and the function generator. In addition to the voltage increase due to the ratio of the number of turns per coil in each circuit as for a standard autotransformer, an additional voltage step up is observed when the frequency applied to the secondary circuit matches the resonance frequency of the primary circuit. The additional step up is equal to the Q factor of the circuit, which was measured with a spectrum analyser to be 90. Impedance matching of the transformer and the function generator was achieved by moving the electrical connection of the secondary circuit to the coil until the reflected rf power reached a minimum.

### Trap Characteristics - Simulations

As before the trap was characterised numerically by calculating the trapping potentials with a finite element code (FEMLAB). The trap efficiency  $\eta$  (equation 3.1) gives an expression to the deviation from an ideal quadrupole trap. The efficiency of the 'alumina' trap is 75%.

The anharmonicity of the ponderomotive potential can be characterised by fitting a polynomial to the data and decomposing the fit in a Taylor expansion and comparing the amplitudes with the harmonic term. These ratios are summarised in Table 3.2.

For the axial confinement a quadratic fit to the numerically evaluated potential in combination with the harmonic oscillator model is used to calculate the confinement strength. This gives a confinement strength of 226 kHz  $\sqrt{U_{DC}}$ .

Numerically evaluating the pseudopotential when including cavity mirrors with  $\epsilon_r = 3.9$  at a separation of 500  $\mu\text{m}$  and comparing the resulting secular frequencies to the case without mirrors show a change in the radial frequency of 5.5%. If we compare this to the 'sandwich' trap (0.5%) this is a large difference, but it is small enough to be confident that the trapping will be unaffected.

### Trap Characteristics - Measurements

The confining potential of the ion trap was again probed by applying a small modulation voltage to one of the mirror electrodes to test the radial potential, and one dc-electrode for the axial potential, while observing the fluorescence as the modulation frequency was scanned.

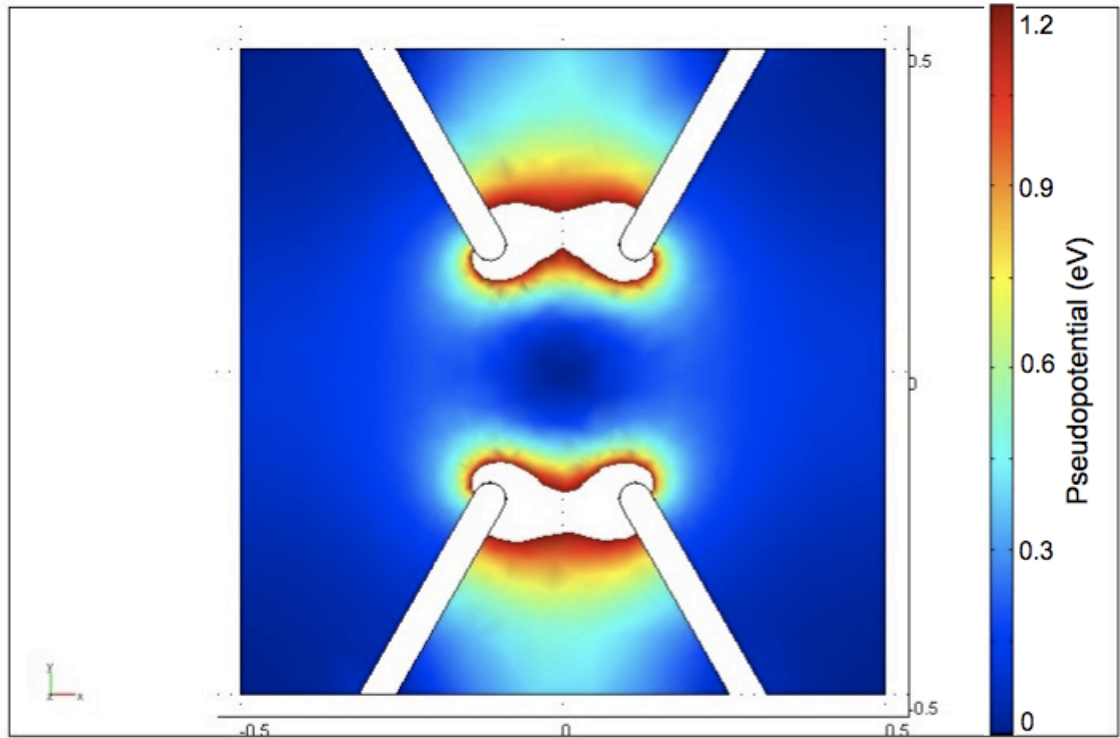


Figure 3.22: Radial cross-section of the pseudopotential of the 'alumina' linear trap in the at the trap center for  $U_{AC} = 61.48\text{ V}$ , obtained from a finite element calculation by averaging the potential over one rf-cycle. (All distances are in mm.)

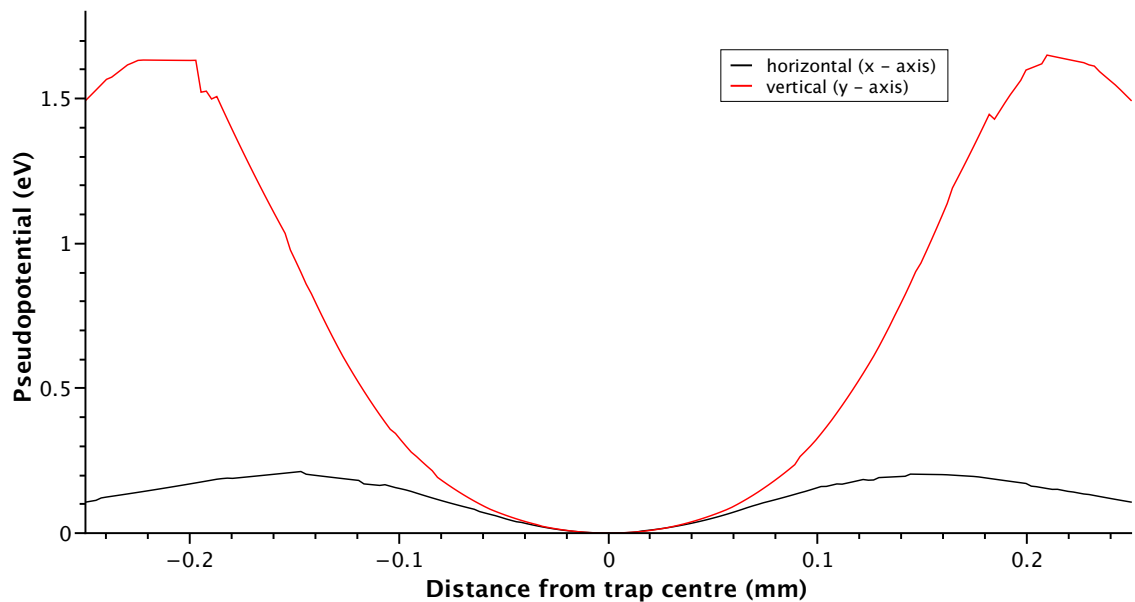


Figure 3.23: Profile of the pseudopotential in the horizontal and vertical direction for  $U_{AC} = 61.48\text{ V}$ .

Using this method for different amplitudes  $U_{AC}$  of the rf-voltage, found that stable trapping is obtained for radial secular frequencies in the range of  $\nu_{\text{secular, radial}} = 1\text{ - }3\text{ MHz}$  (figure 3.24), which equates to  $q$  values from 0.1-0.31 and potential depths from 0.23-1.71 eV. Axial secular

radial (x) confinement	radial (y) confinement	axial confinement
$C_4 r^2/C_2 = 1 \cdot 10^{-7}$	$C_4 r^2/C_2 = 8 \cdot 10^{-9}$	$C_4 z^2/C_2 = 2 \cdot 10^{-5}$
$C_6 r^4/C_2 = 4 \cdot 10^{-14}$	$C_6 r^4/C_2 = 2 \cdot 10^{-15}$	$C_6 z^4/C_2 = 4 \cdot 10^{-11}$
$C_8 r^6/C_2 = 4 \cdot 10^{-21}$	$C_8 r^6/C_2 = 7 \cdot 10^{-23}$	$C_8 z^2/C_2 = 3 \cdot 10^{-13}$

Table 3.2: Relative size of anharmonic contributions to the radial (ponderomotive) and axial (dc) confinement of the 'alumina' trap.  $C_n$  is the coefficient of the  $n$ -th term in the Taylor expansion of the potential. The anharmonicity was evaluated at the transverse size  $r \approx 20\text{nm}$  of an ion's wave packet at a temperature of  $1\text{mK}$  in the radial direction and the displacement  $z \approx 6\mu\text{m}$  of an ion in a two-ion crystal in the axial direction, assuming typical experimental parameters.

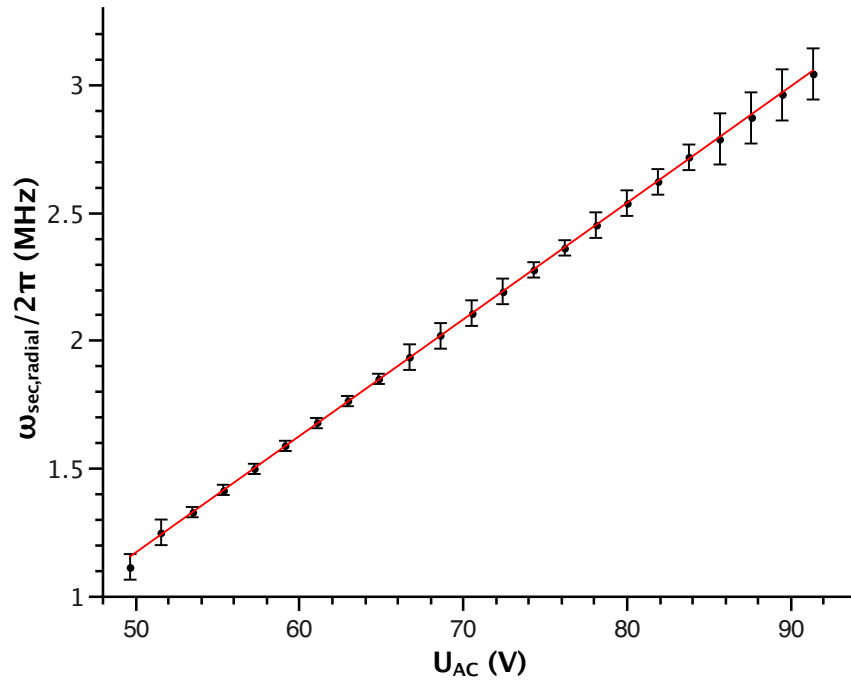


Figure 3.24: The relationship between the radial secular frequency and the voltage applied to the two rf-electrodes.

frequencies range from  $\nu_{\text{secular, axial}} = 200 - 500 \text{ kHz}$  (figure 3.25), which is approximately 86% of the values obtained from the simulation for axial confinement. Comparing the measured secular frequency to the value obtained for an ideal trap gives a voltage loss factor of 72% for the radial confinement. Comparing to the simulation results the measured values are 4% smaller.

### 3.4.3 Micromotion Compensation

In chapter 1 we explained how stray electric fields can cause micromotion of the ion, which leads to line broadening, heating and reduced coupling due to bad localisation of the ion in the cavity mode. To compensate the electric stray fields and hence avoid micromotion, we

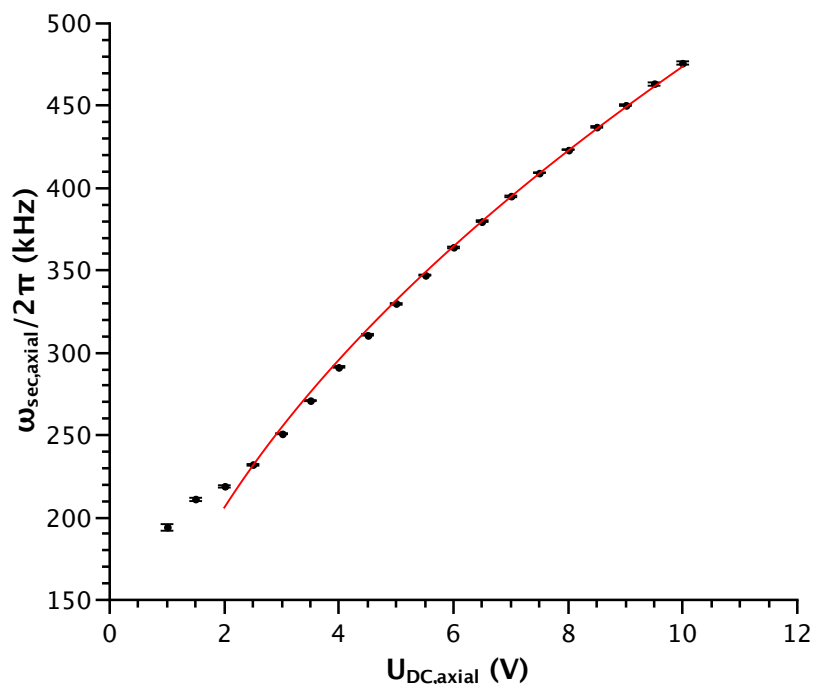


Figure 3.25: The relationship between the axial secular frequency and the dc-voltage applied to all four endcap electrodes.

apply additional dc offset voltages to the rf-electrodes. There are several methods that can be employed to establish the correct compensation voltages.

### Linewidth Minmisation

For weak confinement ( $\Gamma \gg \Omega$ ), as it is present in our traps, the sidebands caused by the ion's oscillations in the trap are not resolved, but the linewidth of the transition observed is broadened. The linewidth gives a measure of how well the stray fields are compensated. In practise the laser is red detuned from the transition to the full width half maximum of the line, where the most drop for decrease in linewidth is achieved. To establish the linewidth which at this stage is likely to be broadened from its theoretical value, we perform a spectroscopy scan, that is we scan the laser wavelength from red detuned to just beyond resonance and record the fluorescence response. From a Lorentzian fit to the data the linewidth of the transition can be evaluated. This method is a useful first step for a rough compensation before progressing to more elaborate methods. Figure 3.26 illustrates the effect micromotion has on the linewidth of the cooling transition.

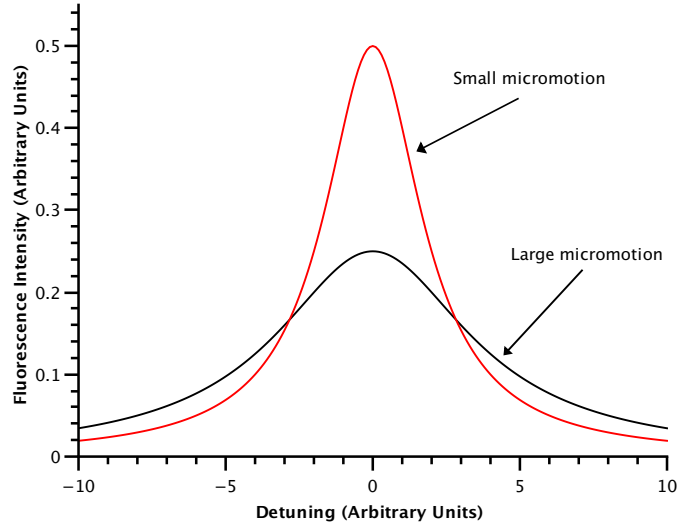


Figure 3.26: The linewidth of the cooling transition increases with micromotion. Therefore spectroscopy scans give a measure of the amount of micromotion the ion is undergoing.

### Correlation Method

The correlation method is the most accurate and reliable method for micromotion compensation for a trap in the weak confinement regime. In the rest frame of an ion subject to micromotion the laser frequency appears modulated because of the Doppler effect:

$$\Delta\nu(t) = \vec{k} \cdot \vec{x} \Omega_{\text{RF}} \cos(\Omega_{\text{RF}} t) , \quad (3.3)$$

where  $\vec{k}$  is the wave vector of the laser and  $\vec{x}$  the vector representing the micromotion amplitude. The fluorescence intensity of the ion depends on the detuning of the laser, and hence this effect results in a modulation of the fluorescence signal as described in figure 3.27.

To explain how we obtain a measure of the fluorescence modulation let's consider the dependence of the fluorescence intensity on the laser detuning. For small motional amplitudes a Taylor expansion around the laser detuning as seen by an ion at rest can be used, where small is defined as  $\Delta\nu(t)$  being small compared to the laser detuning of an ion at rest in the laboratory frame,  $\Delta\nu_0$ , and the transition linewidth,  $\Gamma$ . The countrate,  $I(\nu)$ , then varies as a function of time according to

$$I_{\text{corr}}(\Delta\nu_0, t) = I(\Delta\nu_0) + \left. \frac{dI(\nu)}{d\nu} \right|_{\nu=\Delta\nu_0} \cdot \vec{k} \cdot \vec{x} \Omega_{\text{RF}} \cos(\Omega_{\text{RF}} t) . \quad (3.4)$$

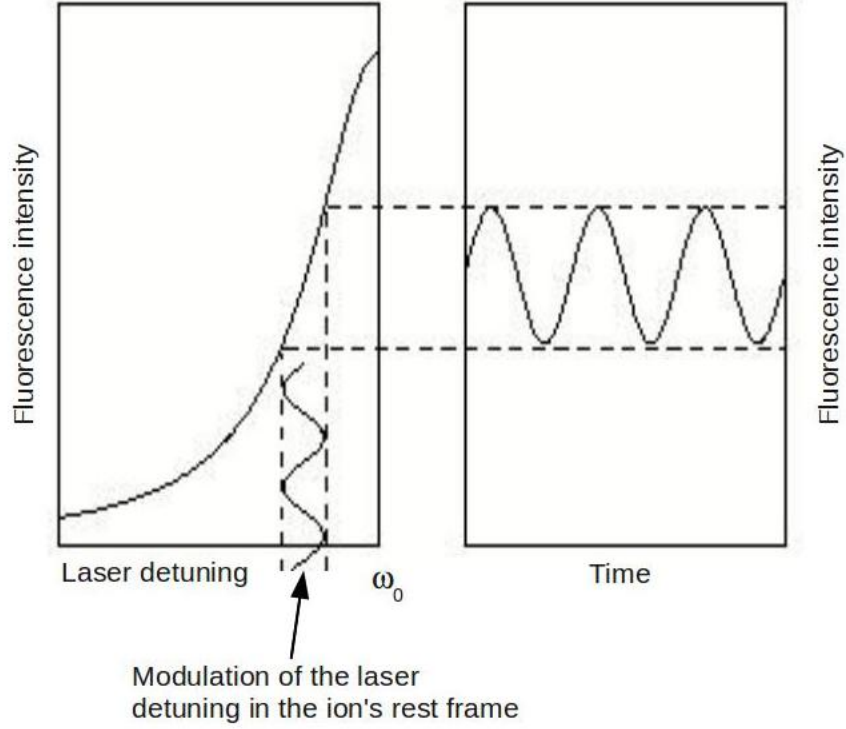


Figure 3.27: The micromotion of the ion causes the ion to experience a modulation of the incident laser radiation. This is observed as a modulation in the fluorescence intensity.

Assuming the transition's line profile to be Lorentzian the time evolution of the intensity is

$$I_{\text{corr}}(\Delta\nu_0, t) = \frac{\left(\frac{\Gamma}{2}\right)^2 I_{\text{max}}}{\Delta\nu_0^2 + \left(\frac{\Gamma}{2}\right)^2} - \frac{\left(\frac{\Gamma}{2}\right)^2 I_{\text{max}} \Delta\nu_0}{\left[\Delta\nu_0^2 + \left(\frac{\Gamma}{2}\right)^2\right]^2} \cdot \vec{k} \cdot \vec{x} \Omega_{\text{RF}} \cos(\Omega_{\text{RF}} t). \quad (3.5)$$

We measure this effect by observing the time-resolved ion fluorescence in relation to the phase of the trap drive. A time-to-digital converter is triggered by the arrival of a photon at the photon multiplier tube, and stopped at a fixed phase of the trap drive. The time difference between start and stop are recorded in a histogram. By looking closely at equation (3.5) we can see that the amplitude of the modulation depends on the transition linewidth, the laser detuning, and the maximum count rate,  $I_{\text{max}}$ . The amplitude of the modulation can be deduced to [12]

$$A = \Delta t \frac{T_{\text{rec}}}{2T_{\text{trap}}} (I_{\text{corr}}(\Delta\nu_0, t_{\text{max}}) - I_{\text{corr}}(\Delta\nu_0, t_{\text{min}})) = \Delta t \frac{T_{\text{rec}} \Omega_{\text{RF}}^2}{2\pi} \frac{dI(\nu)}{d\nu} \Big|_{\nu=\Delta\nu_0} \cdot \vec{k} \cdot \vec{x}, \quad (3.6)$$

where  $T_{\text{rec}}$  is the recording time,  $T_{\text{trap}}$  the trap drive's period, and  $\Delta t$  the width of a histogram

interval. For a Lorentzian this equals

$$A = \Delta t \frac{T_{\text{rec}} \left(\frac{\Gamma}{2}\right)^2 I_{\text{max}} \Delta\nu_0}{\pi \left[\Delta\nu_0^2 + \left(\frac{\Gamma}{2}\right)^2\right]} \cdot \vec{k}\vec{x}\Omega_{\text{RF}}^2. \quad (3.7)$$

This also holds true for saturated spectra if  $\Gamma$  is replaced with  $\Gamma\sqrt{1+S}$ , where  $S$  is the saturation parameter. A measurement of the amplitude  $A$  requires the amplitude to be larger than the noise of the measurement. If the noise is due to counting statistics then  $A > \sqrt{\bar{N}}$ .  $\bar{N}$  is the average number of events recorded per channel:

$$\bar{N} = \int_0^{T_{\text{trap}}} I(t) dt \cdot \frac{\Delta t}{T_{\text{trap}}} = \bar{I} \frac{\Delta t}{T_{\text{trap}}} T_{\text{rec}}. \quad (3.8)$$

$\bar{I}$  is the average number of events for all channels. Using equations (3.8), and (3.6) the recording time evaluates to

$$T_{\text{rec}} > \frac{2\pi\bar{I}}{\Delta t \Omega_{\text{RF}} \left. \frac{dI(\nu)}{d\nu} \right|_{\nu=\Delta\nu_0}^2} \cdot \frac{1}{\left(\vec{k}\vec{x}\Omega_{\text{RF}}\right)^2}. \quad (3.9)$$

For a Lorentzian lineshape the largest slope occurs at  $\Delta\nu_0 = \frac{\Gamma}{2}$ , and thus this is the detuning where the largest effect can be observed. Equation (3.7) allows to evaluate the term  $\vec{k}\vec{x}$ , and consequently the micromotion amplitude, from the modulation amplitude of the histogram. The accuracy of a individual measurement depends on the recording time only. In practice we measure a fixed number of events rather than a period of time.

It is worth noting that large micromotion amplitude results in a modulation of the fluorescence that has twice the frequency of the trap drive. In this case the ion motion is so large that the the laser detuning in the ion's rest frame changes from red to blue detuned during one period of oscillation.

To determine the position of minimal micromotion we need to establish the point of minimum fluorescence modulation. The ion is displaced horizontally and vertically using additional dc voltages on the rf-electrodes (H and V) and the fluorescence amplitude modulation is recorded. A linear fit to the amplitude data then lets us determine the point of optimally compensated micromotion in the direction of the probing laser beam. An example of such a measurement can be seen in figure 3.28. Because it employs the Doppler effect only micromotion in direction of the laser beam used to probe it can be measured. Hence, in a linear Paul trap two laser beams are necessary, as long as they have a non-collinear projection onto the

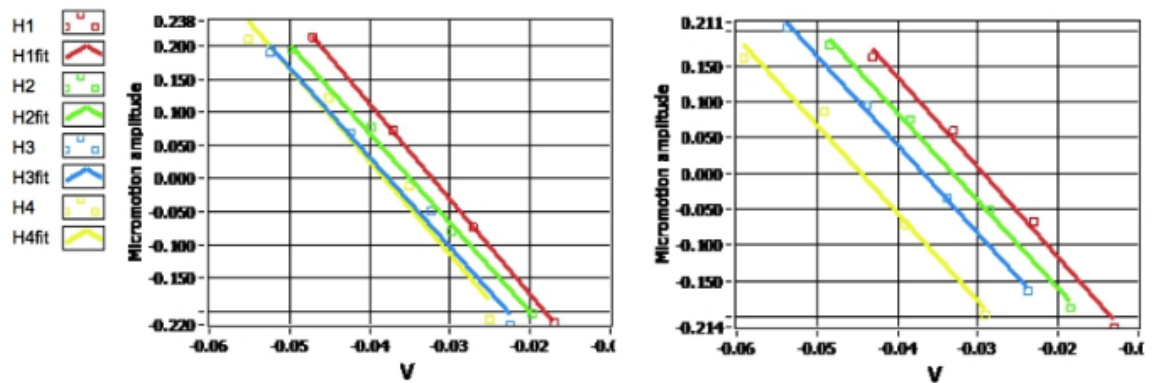


Figure 3.28: Examples of typical graphs from the micromotion compensation routine. For each laser we record the micromotion amplitude at a series of H and V voltages. The four H values ranged from  $-0.01$  to  $0.07$  V by in this case and were spaced at equal distances.

plane perpendicular to the trap axis. A combination of the micromotion data from both laser beams results in a graph like 3.29, and determines the horizontal and vertical dc voltages we need to apply to minimise the micromotion in all dimensions.

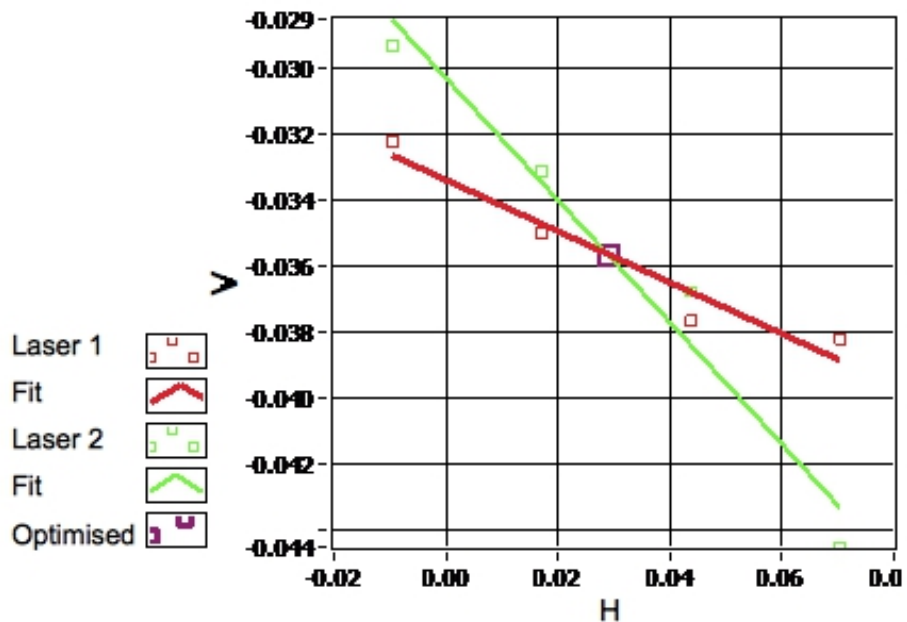


Figure 3.29: An example of a typical graph from the micromotion compensation routine. For each laser there are 4 data points (H and V voltages) where the micromotion is zero. Where the linear fit to these cross the micromotion is minimised for all radial dimensions.

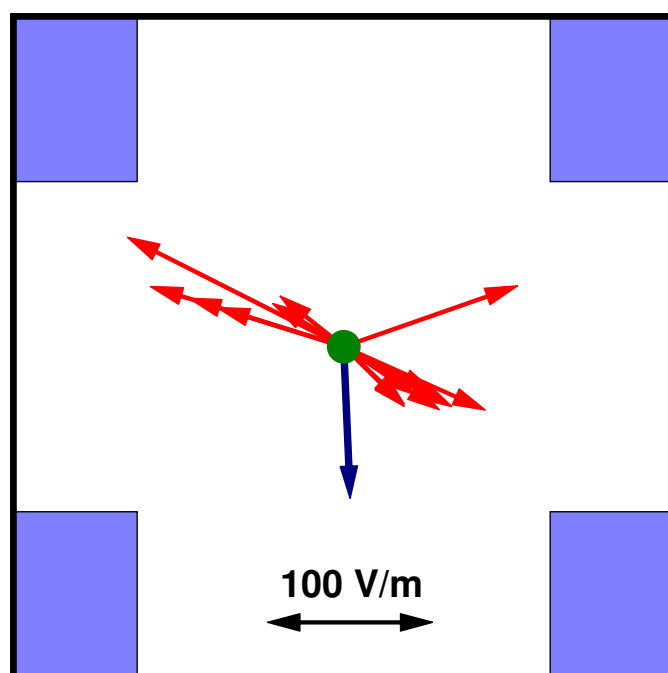


Figure 3.30: Average direction of stray fields (blue arrow) as well as deviations (red arrows), obtained by subtracting the average from each individual stray field measurement. The position of the rf-electrodes in the four corners is indicated. Data were taken over a period of 129 days. The direction of the day-to-day deviations during this time appears mainly along one diagonal. The scale of the deviations in V/m is indicated at the bottom.

Typical values of the residual modulation of fluorescence for an ion in the 'sandwich' trap after compensation of micromotion were less than 1% of average fluorescence level detected during the compensation. This corresponds to a residual motional amplitude of the ion of below 8 nm which is two orders of magnitude lower than the size of the standing wave structure of the cavity mode. This is essential for achieving deterministic ion-cavity coupling.

The compensation voltages and hence the stray fields obtained in this way changed during the period of data acquisition. Over 129 days, the compensation electric fields varied between -88 V/m and 106 V/m in the horizontal direction and -135 V/m and -47 V/m in the vertical. The average shift observed during this time was in the vertical direction. The size of variations around this average was statistical. In Fig. 3.30 the average stray field is shown along with the daily deviations. It is striking that the variations occur predominantly along one diagonal between two rf-electrodes, indicating that stray fields originate on one or two diagonally opposite electrodes. This is in keeping with the fact that the ion trap is loaded in situ, leading to an asymmetric coating of the rf-electrodes with calcium during the loading procedure. This is expected to result in patch potentials which change during the loading of the ion trap [32]. The observed fluctuations mean that an optimisation of the compensation is necessary on a daily basis. During the first months of the experiment we were particularly concerned about

the process seeming unreliable. Eventually we found a bug in the programme written to automate the process. While this reduced the time spent on the micromotion compensation and improved results significantly, it also means that unfortunately some of the data obtained during the spectroscopy measurements presented in chapter 4 is affected by the variability of the early compensation.

## Chapter 4

# Spectroscopy of Single $^{40}\text{Ca}^+$ Ions

### 4.1 Introduction

Calcium is the third element in the group of alkaline earth metals, and has an atomic number of 20. There are four stable isotopes:  $^{40}\text{Ca}$ ,  $^{42}\text{Ca}$ ,  $^{43}\text{Ca}$ , and  $^{44}\text{Ca}$ . In our experiment we use  $^{40}\text{Ca}$ , which is the most abundant (96.941%). As a group II element it possesses two electrons in its outer shell, which have ionisation energies of 6.11 eV and 11.87 eV respectively. To trap calcium we remove one of these electrons via two-stage photo ionisation, leaving one valence electron whose excitation energies are so remote from those of the electrons in the closed shells of the atom that light from the optical region of the electromagnetic spectrum only addresses this valence electron. Thus the resulting level scheme is greatly simplified and particularly useful for quantum optics applications. Figure 3.4 shows the relevant parts of the  $\text{Ca}^+$  level scheme including transition wavelengths and linewidths of transitions. Calcium 40 also possesses an even number of nucleons which is advantageous since it results in no nuclear spin and thus no hyperfine structure complicating the level scheme.

### 4.2 Theory

In our experiment we drive the cooling cycle on the  $P_{1/2} \rightarrow S_{1/2}$  transition ( $\lambda = 396.595 \text{ nm}$ ). We can treat the ion as a two-level system with a single loss mechanism, the  $P_{1/2} \rightarrow D_{3/2}$  transition. For efficient cooling it is necessary to avoid the ion escaping the cooling cycle via this transition. There are two possible ways to do this. Either laser light at 866 nm is provided to drive the  $D_{3/2} \rightarrow P_{1/2}$  transition, repumping the ion back into the cooling cycle. The disadvantage of this method is that it results in a coupling between the  $S_{1/2}$  and the  $D_{3/2}$  level, and treating the ion as a two-level system is no longer adequate. Instead the ion has to

be treated as a  $\Lambda$  system if this method of repumping is employed.

This can be avoided by repumping via the  $P_{3/2}$  level. Two lasers are required for this process. 850 nm light transfers any population of the  $D_{3/2}$  to the  $P_{3/2}$  level. From the  $P_{3/2}$  level the ion can decay either to the  $S_{1/2}$  level, as desired, or to the  $D_{5/2}$  level. The latter transition, even though much less likely to occur, is not part of the cooling cycle, and hence impairs efficient cooling. A 854 nm laser is employed to excite the ion back to the  $P_{3/2}$  level.

The wavelengths of the cooling laser as well as the repumper lasers, and the laser power influence the level of fluorescence from the ion. To increase cooling and detection efficiency it is necessary to investigate the influence of these parameters.

### 4.2.1 Line Profile

The optical Bloch equations for a two-level atom including spontaneous emission have been discussed in sections 2.2.1 and 2.2.1. We arrived at the steady state solutions to the rate equations given in equations 2.26 and 2.27. Both equations have characteristics of a Lorentzian,

$$L(\omega - \omega_0) = \frac{\Gamma_{\text{eff}}}{2\pi} \frac{1}{(\omega - \omega_0)^2 + \frac{\Gamma_{\text{eff}}^2}{4}}, \quad (4.1)$$

with the effective linewidth of the transition

$$\Gamma_{\text{eff}} = 2\sqrt{\left(\frac{\Gamma}{2}\right)^2 + \frac{1}{2}|\Omega_0|^2}. \quad (4.2)$$

$\Omega_0$  is the on resonance Rabi frequency which is proportional to the electric field of the light incident on the ion. Thus with increasing light intensity the linewidth of the transition increases. This effect is known as power broadening. Power broadening is a homogeneous broadening effect, it affects all atoms in the same way for a given light intensity.

### Saturation

As the power of the incident light increases so does the upper state population, equation 2.26, approaches one half. The saturation parameter is defined in equation 2.31. On resonance, i.e.  $\delta = 0$ , the saturation parameter expresses the ratio between excitation and spontaneous emission. If saturation is defined as  $S = 1$ , the excited state population,  $\rho_{22}$ , equals 1/4, and equation 2.31 simplifies to  $\Omega_0 = \frac{1}{\sqrt{2}}\Gamma$ . The intensity of the light wave is defined as

$$\bar{I} = \frac{1}{2}\epsilon_0 c E_0^2. \quad (4.3)$$

Using the conversion factor between the dipole moment and the Einstein A coefficient,  $\mu^2 = A_{21} \frac{3\pi\epsilon_0\hbar c^3}{\omega_0^3}$  [33], and substituting  $\omega_0 = 2\pi c/\lambda_0$ , the saturation intensity can be written as

$$I_{\text{Sat}} = \frac{2\pi^2 c \hbar \Gamma}{3\lambda_0^3}. \quad (4.4)$$

For the calcium  $P_{1/2} \rightarrow S_{1/2}$  transition using literature values for the linewidth and wavelength the saturation intensity is  $7.409 \text{ mW/cm}^2$ . Similarly for the  $P_{3/2} \rightarrow D_{3/2}$  and the  $P_{3/2} \rightarrow D_{5/2}$  the saturation intensities are  $0.052 \text{ mW/cm}^2$  and  $0.006 \text{ mW/cm}^2$ , respectively.

### Voigt Profile

An ion at temperature  $T$  appears broadened because of its translational motion resulting in a Doppler shift of  $\delta = \omega - \omega_0$ , or alternatively  $\omega = \omega_0 \left(1 + \frac{v_z}{c}\right)$ . The distribution of the frequencies  $\omega$  is linked to the distribution of speeds via

$$P_\omega = P_{v_z} \frac{c}{\omega_0}. \quad (4.5)$$

At thermal equilibrium the velocities have a Maxwell-Boltzmann distribution:

$$P_{v_z} = \sqrt{\frac{m}{2\pi k_B T}} e^{-\frac{mv_z^2}{2k_B T}}, \quad (4.6)$$

where  $m$  is the mass of the emitting particle,  $T$  is the temperature and  $k_B$  is the Boltzmann constant. Substituting equation 4.6 into equation 4.5 we arrive at

$$D(\omega - \omega_0) = \frac{c}{\omega_0} \sqrt{\frac{m}{2\pi k_B T}} e^{-\frac{mc^2(\omega - \omega_0)^2}{2\omega_0^2 k_B T}}. \quad (4.7)$$

This is a Gaussian distribution with a peak at  $\omega_0$  and a FWHM  $2\omega_0 \sqrt{\frac{2k_B T \ln 2}{mc^2}}$ . In contrast to the Lorentzian lineshape of natural, and power broadening, Doppler broadening is a heterogeneous broadening effect, because the Doppler shift is unique for every individual atom. Although we are dealing with single ion in our experiments this concept still applies as the atoms thermal state can be described as a superposition of Fock states of its motion.

Because in practise both homogeneous and heterogeneous broadening are present the lineshape of an atom is usually represented by a convolution of both homogeneous (Lorentzian) and

heterogeneous (Gaussian) lineshapes. This is known as a Voigt profile:

$$V(\omega - \omega_0) = \int_{-\infty}^{\infty} L(\omega - \omega_0 - \omega')D(\omega')d\omega' \quad (4.8)$$

$$= \frac{\Gamma_{\text{eff}}}{\sqrt{2\pi}2\pi} \sqrt{\frac{m}{k_{\text{B}}T}} \int_{-\infty}^{\infty} \frac{e^{-\frac{mc^2(\omega')^2}{2\omega_0^2 k_{\text{B}}T}}}{(\omega - \omega_0 - \omega')^2 + \frac{\Gamma_{\text{eff}}^2}{4}} d\omega'. \quad (4.9)$$

Although this can't be solved analytically it is easily evaluated numerically. In the limit of large temperatures the Doppler profile dominates and the expression simplifies to a Doppler lineshape.

### 4.3 Measurements

For the spectroscopy measurements the fluorescence of the  $P_{1/2} \rightarrow S_{1/2}$  transition of a single calcium ion was recorded with a photomultiplier tube (PMT) while varying several parameters. To optimise the spectroscopy results of the cooling transition, it makes sense to establish the most efficient repumper wavelengths, and an adequate repump intensity first. The experimental setup used during the spectroscopy measurements is shown in figure 4.1. The two repumper laser beams are overlapped first using a polarising beam splitter (PBS). To regulate the intensity in these beams the light passes through a  $\lambda/2$  wave plate before entering the PBS. The combined beams then pass through a dichroic mirror which also serves to reflect one of the cooling lasers (Laser 1 in figure 4.1) towards the chamber. All three beams are overlapped at this stage, and continue to the ion trap via two further mirrors and finally a lens that focusses the beams at the trap centre. The final mirror before the lens is mounted on a piezo so it is possible to scan the beams across the trap centre systematically. This arrangement has proven particularly useful when finding the first ion signal in the trap after the optical setup had to be changed. A second cooling laser (Laser 2) enters from the other end of the trap axis and makes an angle with the horizontal. This is crucial for the micromotion compensation. The two lasers for the two-stage photo-ionisation that we employ to make the ions are also combined using a PBS. They enter the chamber via two further mirrors used for alignment. In contrast to laser 2 they are aligned in the horizontal, and pass just underneath the final mirror directing laser 2 into the chamber. The angle between these lasers is however so slight that it is possible to use the same lens to focus all three. Finally, the ions' fluorescence can be observed using an EMCCD camera or a PMT. The imaging setup was described in more detail in chapter 3.3.

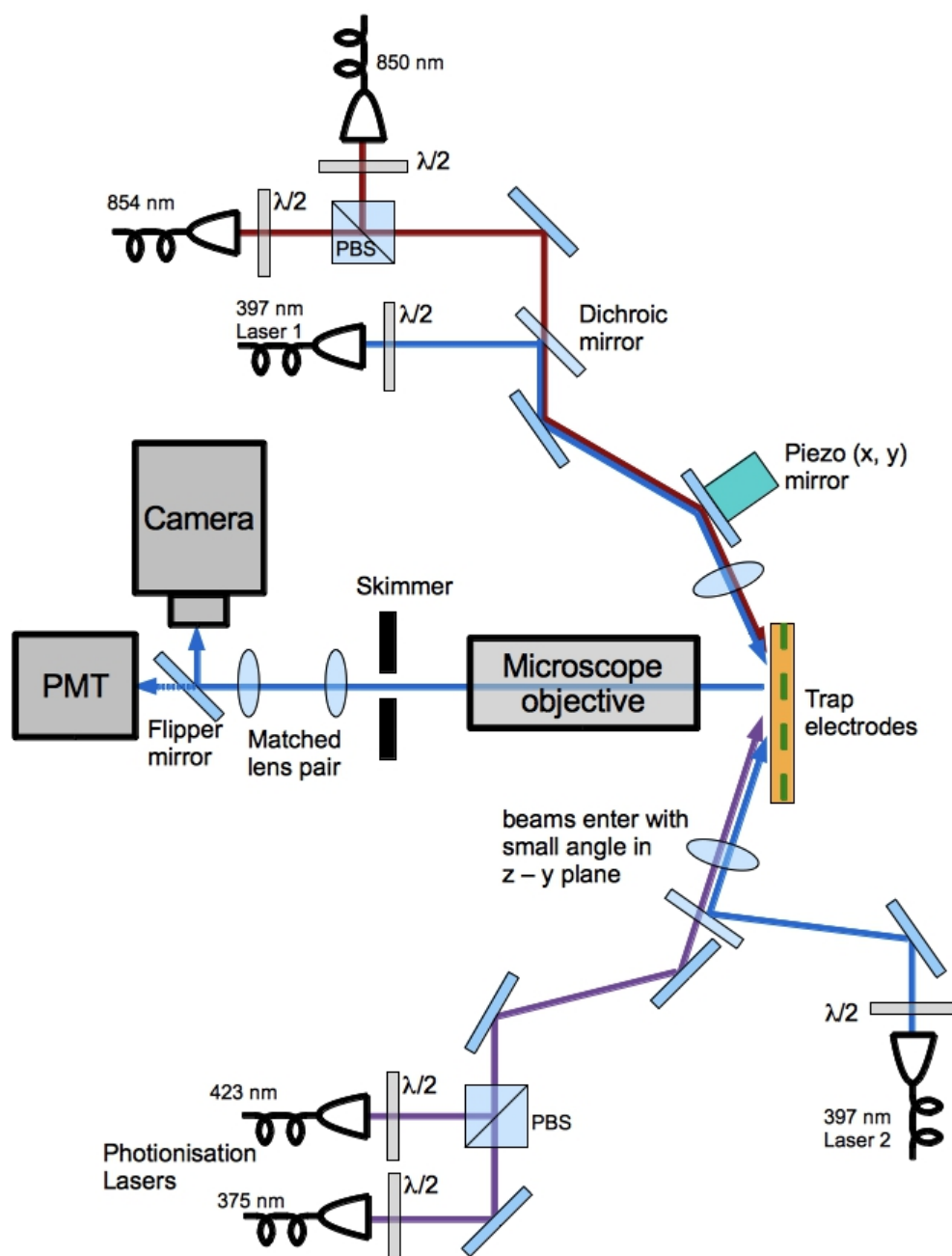


Figure 4.1: A schematic of the optics and laser setup during the spectroscopy and heating rate measurements.

### 4.3.1 Repumper Spectroscopy and Initial Intensity Settings

The first measurement concerned the cooling transition fluorescence as a function of power of the repumper lasers. The cooling laser was set to 396.95921 nm (detuning  $\delta = 95$  MHz).

With a waist of  $45\ \mu\text{m}$  a power of  $0.4\ \mu\text{W}$  from the two cooling beams is equivalent to the previously calculated saturation intensity. During these measurements the cooling laser powers were both set to  $0.44\ \mu\text{W}$ . At constant wavelength one repumper laser beam was set to an intensity level that we assumed to be safely within the region of saturation of the transition, the power in the second repumper beam was varied, and the fluorescence of the cooling transition recorded. The results can be seen in figures 4.2 and 4.3 respectively. From these measurements we concluded that saturation for the given beam diameters the ion position occurred at  $150\ \mu\text{W}$  for the  $850\ \text{nm}$  laser and  $7\ \mu\text{W}$  for the  $854\ \text{nm}$  laser. To determine the

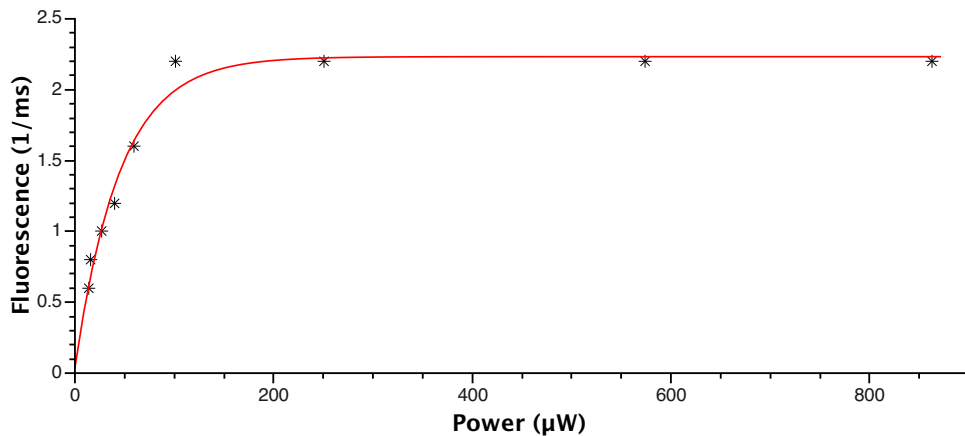


Figure 4.2: The cooling fluorescence level as a function of the  $850\ \text{nm}$  repumper power

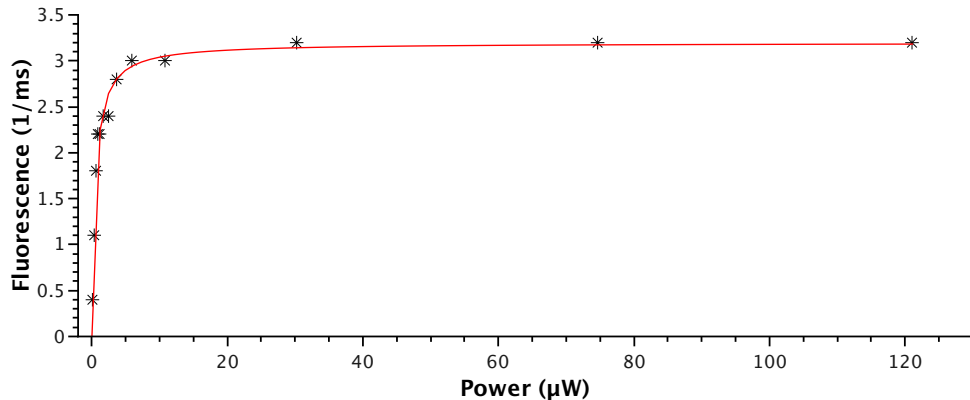


Figure 4.3: The cooling fluorescence level as a function of the  $854\ \text{nm}$  repumper power

exact transition wavelengths for both repumper lasers we observed the level of cooling fluorescence as one repumper wavelength was scanned while the other was kept constant, and vice versa. For this measurement the cooling laser had the same wavelength and intensity settings previously described. Both repumper lasers were set just below saturation to prevent any power broadening effects:  $P_{854} = 0.5\ \mu\text{W}$  and  $P_{850} = 24.5\ \mu\text{W}$ . Figures 4.4 and 4.5 show the results for each of these measurements respectively. During the measurement for the  $854\ \text{nm}$

laser  $\lambda_{850} = 850.03488$  nm, during the measurement for the 850 nm laser  $\lambda_{854} = 854.44334$  nm. From these measurements we determined the centre wavelength for each repumper to within the accuracy of the wavemeter ( $\pm 60$  MHz) to be  $850.03488(14)$  nm and  $854.44334(15)$  nm.

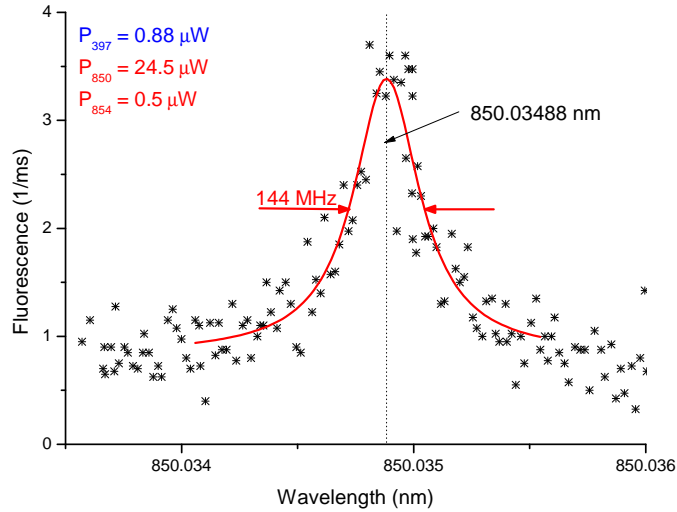


Figure 4.4: The cooling fluorescence level as a function of the 850 nm repumper wavelength

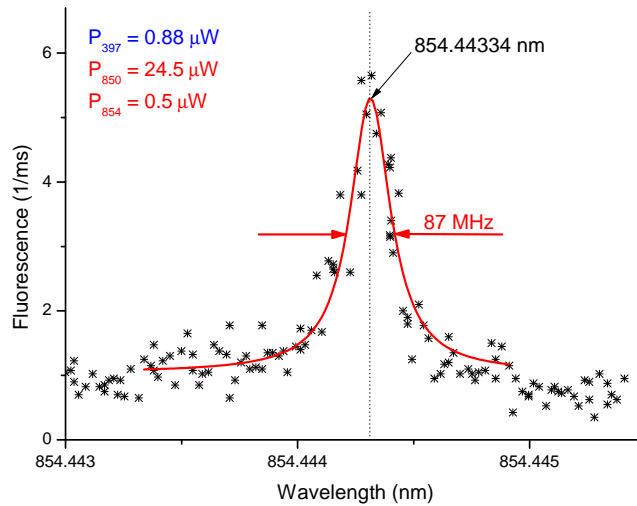


Figure 4.5: The cooling fluorescence level as a function of the 854 nm repumper wavelength

### 4.3.2 Cooling Transition Spectroscopy

For this measurement the cooling laser was scanned from red detuned to blue detuned with respect to the transition wavelength. When the laser is red detuned the fluorescence follows a Lorentzian lineshape, when the laser is blue detuned a sharp drop in fluorescence is observed.

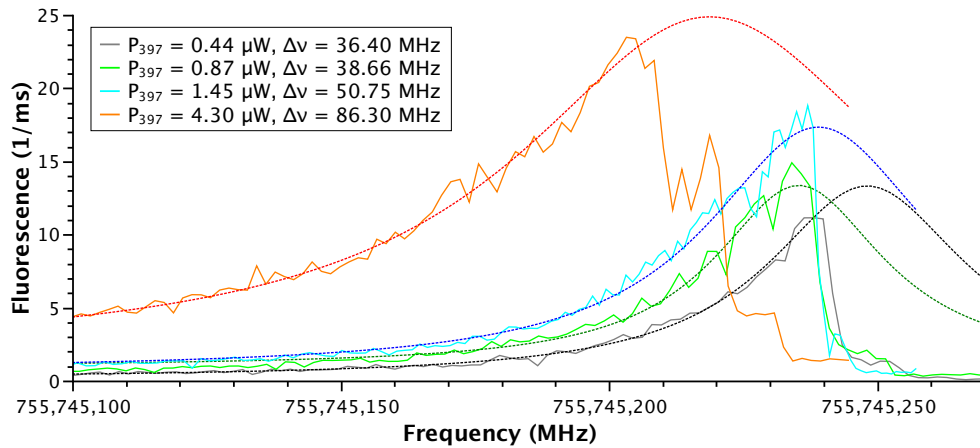


Figure 4.6: The cooling transition spectroscopy scans for various cooling laser powers

The cause of this is the mechanism of Doppler cooling (Chapter 2). A red detuned laser will cool the ions, while a blue detuned laser will heat them. If the ions are heated the fluorescence level drops due to the mechanisms described earlier in this chapter. If heating continues the ion can acquire enough energy to escape the trap, and no more fluorescence is recorded.

Figure 4.6 shows the fluorescence level of the ion as a function of cooling laser frequency for different laser power levels. Because the fluorescence signal follows a Lorentzian shape on the red detuned side of the resonance only, the data used for the fit was restricted from this part of the scan up to the point where a sharp drop in fluorescence was noted.

The centre wavelengths from all four fits agree with each other within the accuracy of the wavemeter used to determine the wavelengths. The resulting wavelength for the cooling transition is 396.95872(954) nm. Within this error it agrees with the value determined by Wolf et al.[34]

With increasing laser power the linewidth of the transition increases (Figure 4.7). This is due to power broadening effects. A fit to the data allows to extrapolate to zero intensity and gives a value of 23.3 MHz. Within the uncertainty of the measurement this matches the literature value of 22.3 MHz.

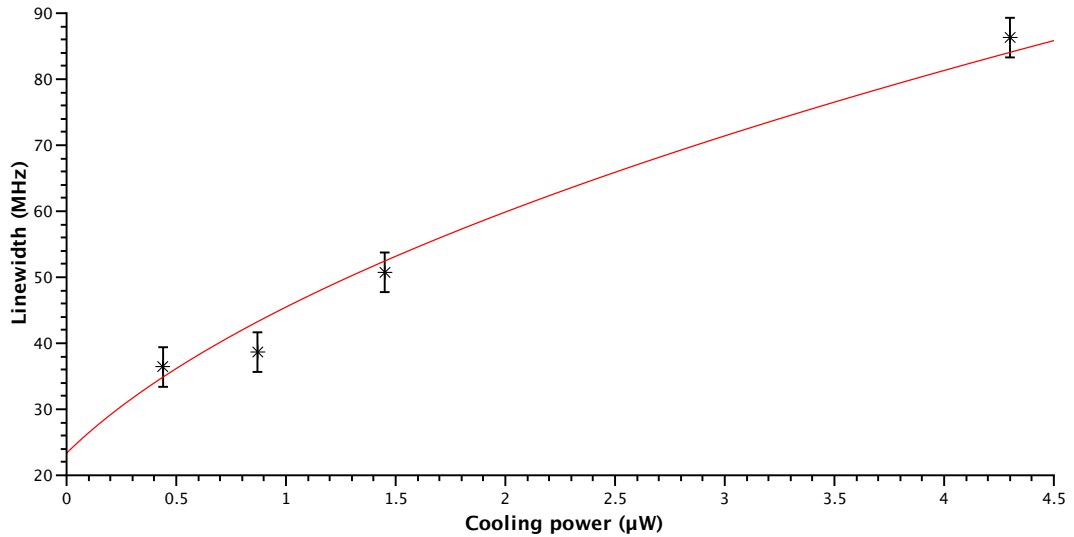


Figure 4.7: The cooling transition linewidth dependence on cooling laser power

### 4.3.3 Cooling Transition Spectroscopy with Variations in Repumper Power

I repeated the cooling transition spectroscopy for different power settings of the repumper lasers to confirm that there is no broadening effect on the cooling transition's lineshape, i.e. it is adequate to treat the ion as a two-level system. We used two cooling lasers with a total cooling power of  $1.2 \mu\text{W}$  so we expected some power broadening effects but as we were looking for the relative changes in the transition profile this was acceptable. The results are presented in Figure 4.8. The scans don't show a clear increase with rising repumper power, in

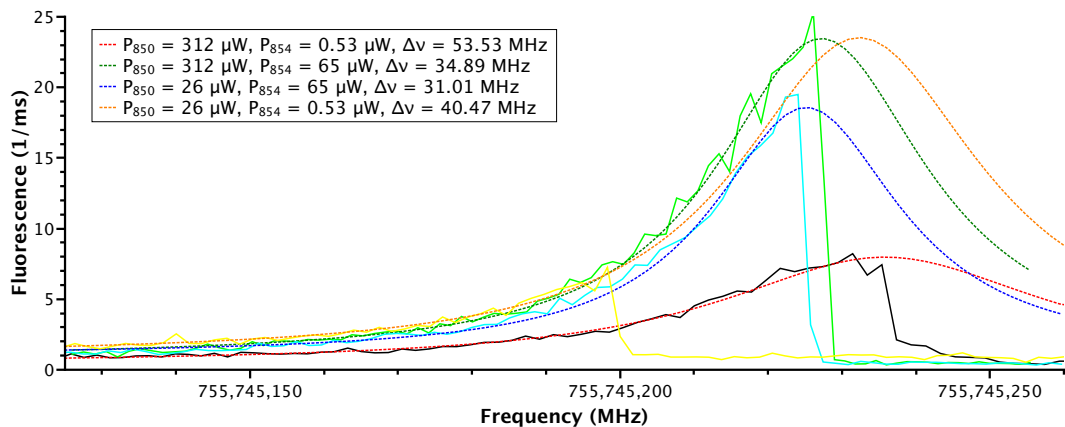


Figure 4.8: Cooling transition spectroscopy scans for combinations of high and low power in the two repumper lasers. The power was set such that low power was below the previously established saturation level of the transition, while the high power setting was just above the point of saturation.

fact the smallest measured linewidth occurs when the 854 nm laser beam carries a lot of power regardless of the power in the 850 nm laser beam. (The linewidth of the scans are the same

within the error of the measurement.) In fact the linewidth in the measurement is narrower than previously measured. This is likely due to an improved micromotion compensation. One interesting feature to note is the narrowing in the linewidth as when the  $D_{3/2} \rightarrow P_{3/2}$  transition is saturated indicating more efficient cooling of the ion. The effect is not observed as strongly for the  $D_{5/2} \rightarrow P_{3/2}$  transition. The transition to the  $D_{5/2}$  level occurs with branching ratio of 7:1000, so it only plays a relatively small part in the scheme, which explains the less pronounced effect. An accurate analysis of how much less pronounced the effect is, is not possible since the low power scan is very inaccurate as the ion escaped from the trap a long time before the scan passed the resonance frequency. The total fluorescence level recorded follows a similar pattern, indicating that the cooling process is the most efficient when both repumpers are run with intensities well beyond the point of saturation. The power in the beams was chosen such that they were in fact quite sufficiently into the region of saturation to exclude any effects on the cooling transition. The measurements show up clearly that it is justified to treat the ion as a two-level system when this repumping scheme is employed, and advise a range of powers that can be used for efficient cooling.

#### 4.3.4 Repumper Spectroscopy for Variations in Repumper Power

The effect of repumper power on the fluorescence level during repumper spectroscopy can be seen in Figures 4.9 and 4.10 for the 850 nm laser and the 854 nm laser respectively. High power is equivalent to 300  $\mu\text{W}$  for the 850 nm laser and 65  $\mu\text{W}$  for the 854 nm laser, low power 24.5  $\mu\text{W}$  and 0.5  $\mu\text{W}$  respectively. As expected a higher power level in the laser that is being scanned leads to a broadening of the line, while an increase in power of the second repumper results in an increase in fluorescence only. This is particularly well illustrated for the 850 nm laser in 4.9. The diode laser providing the 850 nm light was not stable enough to scan over the entire range necessary to sample the entire broadened resonance curve. But due to the symmetry of the curves the acquired data is sufficient for fitting a Voigt profile. For the 854 nm laser the effect can be seen to a lesser extent. The 854 nm spectroscopy measurements need to be viewed with caution since they were taken on different days. At the time of these measurements there were still problems with the micromotion compensation in the trap, and so the conditions in the trap were unfortunately not the same. A summary of the width of the peaks depending on the power of the repumpers is shown in Table 4.1. For efficient cooling it is useful to take advantage of the broadened line of the high power settings as small variations in the linewidth of the repumpers have less of an effect on the cooling fluorescence level.

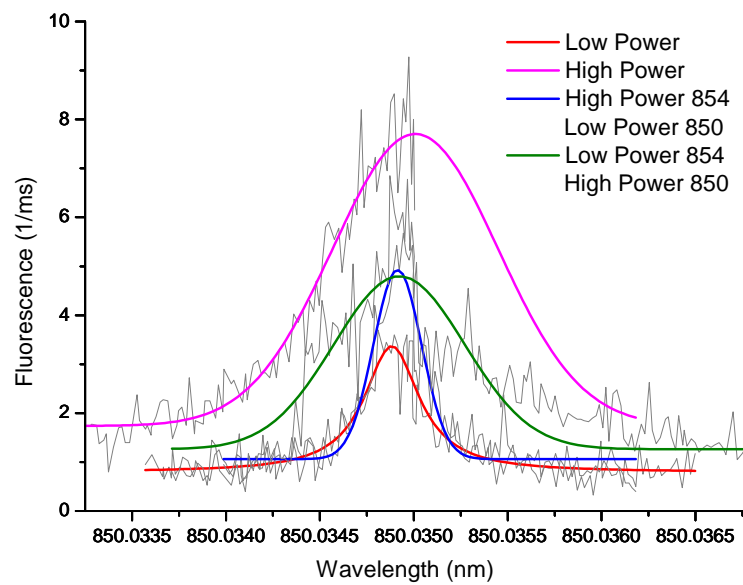


Figure 4.9: The cooling fluorescence as a function of 850 nm repumper wavelength for different combinations of power levels of the repumper lasers with Voigt profile fits

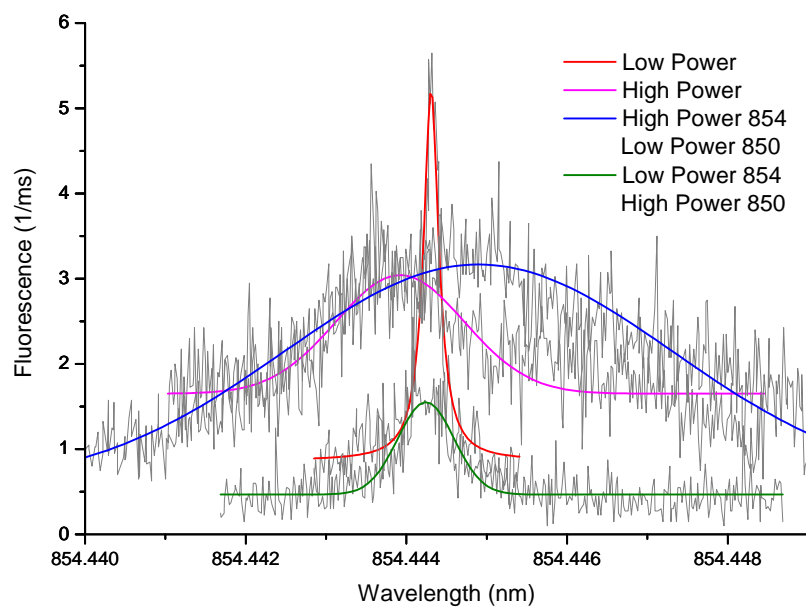


Figure 4.10: The cooling fluorescence as a function of 854 nm repumper wavelength for different combinations of power levels of the repumper lasers with Voigt profile fits

---

Power <sub>850</sub>	Power <sub>854</sub>	Width <sub>850</sub>	Width <sub>854</sub>
300 $\mu\text{W}$	65 $\mu\text{W}$	366 MHz	657 MHz
300 $\mu\text{W}$	0.5 $\mu\text{W}$	289 MHz	287 MHz
24.5 $\mu\text{W}$	65 $\mu\text{W}$	106 MHz	1989 MHz
24.5 $\mu\text{W}$	0.5 $\mu\text{W}$	144 MHz	87 MHz

Table 4.1: Summary of the repumper linewidths for the different power combinations of the repumpers laser beams

## Chapter 5

# Heating Rate Measurement

### 5.1 Introduction

An important issue related to fluctuating patch potentials on the trap electrodes and the small ion-electrode distance is an increase of the ions' temperature. It has direct impact on the localisation of the ions. The heating rate is found to scale inversely with the fourth power of the ion-electrode distance [35, 36]. In a miniature trap like the 'sandwich' trap, heating is therefore expected to be strong and establishing that the rate of heating characteristic to the trap is manageable is important. In experiments where low thermal excitation is achieved by using resolved sideband cooling, a precise measurement of heating rates from the strength of the sidebands is possible [35, 36, 37]. The ions in the 'sandwich' trap are not strongly trapped,

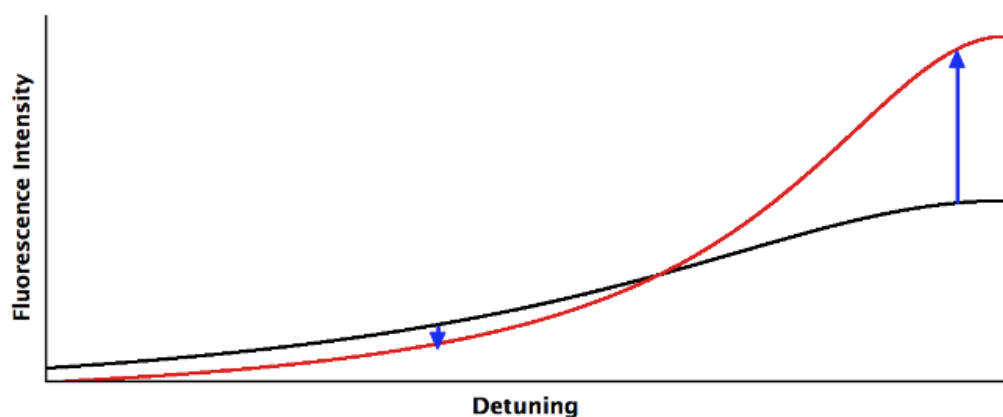


Figure 5.1: The ion fluorescence behaves differently if the spectrum changes shape due to broadening effect. For small detunings the fluorescence level drops when the ion heats up, for large detunings the opposite holds true.

so this method is not available to us. We have employed a simpler method to measure the

heating rate of the trap, based on the one demonstrated by Epstein *et al.* [38]. By suspending Doppler cooling for a given time, the ions experience a period of exclusive heating, increasing their thermal motion in proportion to the heating rate and the heating time. After switching the cooling laser back on, the time-resolved fluorescence of the ions during Doppler recooling can be employed to obtain the temperature at the end of the heating phase. The fluorescence level of the ion changes since the ion's spectrum is narrowed as the ion is cooled. The ion's spectrum is described using a Voigt profile (chapter 4.2.1). Figure 5.1 shows two fluorescence profiles of different width. It is immediately visible that for small detunings, fluorescence increases with decreasing temperature, while for large detunings, fluorescence decreases. A typical fluorescence curve in our experiment is shown in figure 5.2, with the recooling laser switched on at  $t=0$ . As can be seen from the figure, the ion's fluorescence, starting from  $S_0$  at  $t=0$ , approaches the equilibrium value  $S_\infty$  on a time-scale of  $\tau=3.4$  ms. The setup

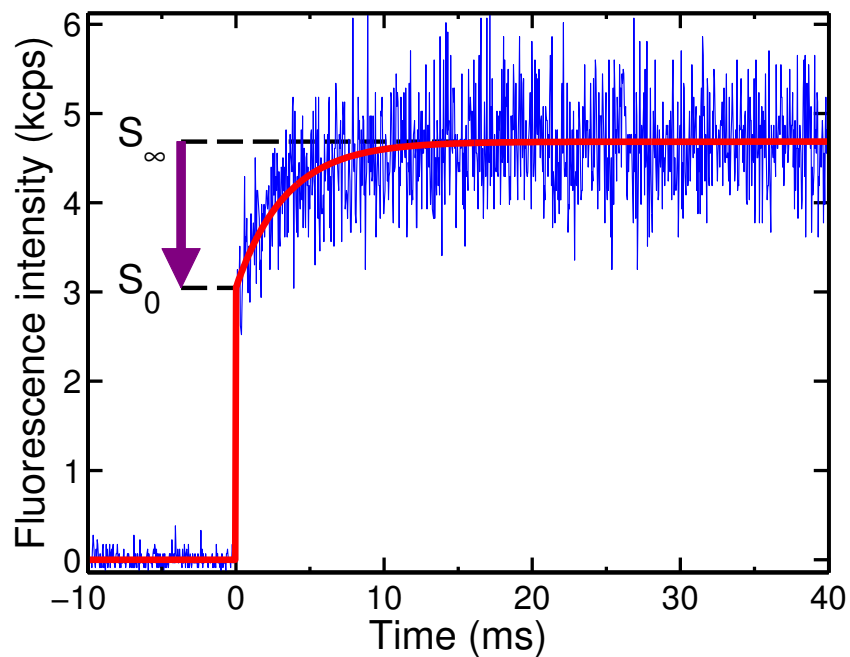


Figure 5.2: Ion fluorescence as a function of time, with the recooling laser switched on at  $t=0$ . The red curve is an exponential fit to the  $R(t) = S_\infty + (S_0 - S_\infty) \cdot \exp(-t/\tau)$ . Fit parameters:  $\tau = 3.4$  ms,  $S_0/S_\infty = 0.66$ .

common for the Doppler recooling method uses a single laser beam with components in both the axial and radial directions. In our setup the laser subtends an angle of  $20^\circ$  with the  $z$  axis. Consequently, the cooling laser exerts radiation pressure on the ion along the axis. While the cooling laser is on, radiation pressure displaces the equilibrium position of the ion away from the centre of the axial potential well. When the cooling is suddenly switched off at the beginning of the heating period, the ion is left in a displaced position in the potential well

and starts to oscillate along the trap axis, with an amplitude equal to the initial displacement  $z_0$ . In the experiment, this displacement cannot be observed directly, but the corresponding oscillation has a significant influence on the spectrum of the ion. Thus, heating of the ion's motion is not the only effect of switching off the Doppler cooling laser. It leads to a Doppler shift peaking at a value of  $\Delta_0$ , which is related to the oscillation amplitude  $z_0$  by

$$\Delta_0 = 2\pi \frac{z_0}{\lambda} \omega_z, \quad (5.1)$$

where  $\lambda$  is the wavelength of the radiation and  $\omega_z = 2\pi \times \nu_z$  is the oscillation frequency of the ion along the trap axis.

Because the radial confinement is much stronger, this effect is much smaller in the *radial* direction. However, even a small radial displacement, moving the ion away from the node of the trapping field, results in increased micromotion, as discussed in section 3.4.3. Both micromotion and axial oscillations contribute to the observed Doppler shift in the spectrum and must be taken into account when determining the ion's temperature. Ignoring these effects may lead to a considerable overestimation of the ion's temperature by falsely attributing a thermal origin to the oscillatory motion. This effect of radiation pressure has not been considered in previous heating rate measurements based on the method introduced in reference [38], even though it can be significant.

## 5.2 Spectrum of an Ion with Intermittent Cooling

We consider the fluorescence line shape of a trapped ion exposed to intermittent excitation. The treatment of homogeneous broadening and thermal Doppler broadening is similar to the one in reference [39] (note that angular frequencies instead of scaled parameters are used). What sets our model apart is that it includes the oscillatory motion of the ion in the harmonic trapping potential resulting from the interruption of radiation pressure. The derived analytical expression allows us to determine the temperature of the ion from the spectrum, without relying on the details of the recoiling dynamics used in reference [39], which would be difficult to model in the presence of radiation pressure.

First we consider the case of homogeneous broadening, applicable to a cold ion at rest in the trapping potential. The normalised spectrum, which is proportional to the fluorescence intensity measured in the experiment is given by a Lorentzian

$$S_{\text{cooled}}(\delta, \Gamma) = \frac{\Gamma}{2\pi} \frac{1}{\frac{\Gamma^2}{4} + \delta^2}, \quad (5.2)$$

where  $\delta$  is the detuning from resonance and  $\Gamma$  is the full width at half maximum of the transition due to homogeneous broadening. When the ion is not at rest but undergoing oscillatory motion in the trapping potential, a periodically changing Doppler shift  $\Delta(t)$  occurs, given by

$$\Delta(t) = \Delta_0 \cos \omega_z t, \quad (5.3)$$

where oscillation along the trap-axis (z-direction) with frequency  $\omega_z$  is assumed and the amplitude  $\Delta_0$  is given by equation (5.1).  $\delta$  in equation 5.2 then has to be replaced by  $\delta + \Delta(t)$ . When observing an ion at an instant the likelihood to find it with an instantaneous Doppler shift  $\Delta_{\text{inst}}$  is given by the probability

$$\begin{aligned} P(\Delta_{\text{inst}}, \Delta_0) &= \int_0^{2\pi} \delta_{\text{Dirac}}(\Delta_{\text{inst}} - \Delta_0 \sin(\phi)) \frac{d\phi}{2\pi} \\ &= \frac{1}{\pi} \frac{1}{\sqrt{\Delta_0^2 - \Delta_{\text{inst}}^2}} \quad \text{if } |\Delta_{\text{inst}}| < \Delta_0. \end{aligned} \quad (5.4)$$

To obtain the scattering rate the following integral has to be evaluated

$$S_D = \int P(\Delta_{\text{inst}}, \Delta_0) \frac{\Gamma}{2\pi} \frac{1}{\frac{\Gamma^2}{4} + (\delta + \Delta_{\text{inst}})^2} d\Delta_{\text{inst}}. \quad (5.5)$$

The real part of the solution of this integral gives us an expression for a spectrum modified by the periodic Doppler shift

$$S_D(\delta, \Gamma, \Delta_0) = \frac{1}{\pi} \text{Re} \left[ \frac{1}{\sqrt{\Delta_0^2 - \left(\delta + i\frac{\Gamma^2}{4}\right)}} \right]. \quad (5.6)$$

For an ion undergoing thermal motion, spectrum (5.6) must be averaged over a distribution of Doppler shift amplitudes  $\Delta_0$ . It is convenient to express the Doppler shift through the oscillatory energy  $\epsilon = m\omega_z^2 z_0^2/2$  of the ion and the recoil energy  $E_r = h^2/2m\lambda^2$  [39]:

$$\hbar\Delta_0 = \frac{\hbar z_0 \omega_z}{\lambda} = \sqrt{4\epsilon E_r}. \quad (5.7)$$

The probability distribution for oscillation energy  $\epsilon$  of the ion is given by

$$P(\epsilon, \bar{\epsilon}) = \frac{1}{\bar{\epsilon}} \exp\left(\frac{-\epsilon}{\bar{\epsilon}}\right), \quad (5.8)$$

where  $\bar{\epsilon}$  is the mean energy.

The thermally broadened spectrum is then obtained as

$$S_{\text{therm}}(\delta, \Gamma, \sigma) = \int_0^{\infty} P(\epsilon, \bar{\epsilon}) S_{\text{D}}(\delta, \Gamma, \sqrt{4\epsilon E_r/\hbar}) d\epsilon, \quad (5.9)$$

with  $\hbar\sigma = \sqrt{2E_r\bar{\epsilon}}$ . The integral can be evaluated and expressed in analytical form

$$S_{\text{therm}}(\delta, \Gamma, \sigma) = \frac{1}{\sqrt{2\pi}\sigma} \text{Re} \left[ w \left( \frac{|\delta| + i\Gamma/2}{\sqrt{2}\sigma} \right) \right]. \quad (5.10)$$

The function  $w(z)$  is the Faddeeva function or complex error function, given by

$$w(z) = \exp(-z^2) (1 - \text{erf}(-iz)) \quad (5.11)$$

and can be readily computed [40]. Expression (5.10) is identical to a Voigt profile with inhomogeneous linewidth  $\sigma$ .

However, equation 5.9 only holds for an ion at rest which is heating up. To accommodate for the fact that the ion starts oscillating with fixed amplitude  $z_0$  as soon as the laser is switched off and before it starts heating up we use a modified distribution function, spread around an oscillation at fixed energy  $\epsilon_0 = (\hbar\Delta_0)^2/4E_r$ .

$$P_{\text{osc}}(\epsilon, \epsilon_0) = \frac{1}{\bar{\epsilon} [2 - \exp(-\epsilon_0/\bar{\epsilon})]} \exp\left(-\frac{|\epsilon - \epsilon_0|}{\bar{\epsilon}}\right). \quad (5.12)$$

Finally, the spectrum of a hot ion including homogeneous broadening, harmonic oscillation and thermal effects is therefore given by

$$S_{\text{heated}}(\delta, \Gamma, \sigma, \Delta_0) = \int_0^{\infty} P_{\text{osc}}(\epsilon, \epsilon_0) S_{\text{D}}(\delta, \Gamma, \sqrt{4\epsilon E_r/\hbar}) d\epsilon. \quad (5.13)$$

The integral in (5.13) can be solved analytically, again using the Faddeeva function:

$$S_{\text{heated}}(\delta, \Gamma, \sigma, \Delta_0) = \text{Re} \left[ \frac{w(\sqrt{z-d}) - i w(\sqrt{d-z^*}) + ie^{-d} w(\sqrt{-z^*})}{\sqrt{2\pi}\sigma(2 - e^{-d})} \right], \quad (5.14)$$

where

$$z = \frac{(|\delta| + i\Gamma/2)^2}{2\sigma^2}, \quad d = \frac{\Delta_0^2}{2\sigma^2}$$

and  $w(z)$  is defined in equation (5.11). It is easy to see that for negligible oscillatory motion of the ion ( $\Delta_0 \rightarrow 0$ ), the above expression reduces to (5.10), i.e., a Voigt profile.

Expression (5.14) describes the most general fluorescence spectrum of a trapped ion.

In the experiment, the homogeneous linewidth  $\Gamma$  is determined by fitting the fluorescence spectrum  $S_{\text{cooled}}$  (equation 5.2),  $\sigma$  is related to the temperature of the ion and  $\Delta_0$  is either due to secular motion in the trap or due to micromotion.

Oscillation along the axis of the linear trap is usually a result of the sudden switch-off of the cooling laser at the beginning of the heating period. Radiation pressure of the cooling laser displaces the equilibrium position of the ion by an amount  $z_0$  in the axial potential well. Removal of radiation pressure therefore launches oscillatory motion with amplitude  $z_0$ . A value of the initial displacement  $z_0$  can be derived from balancing the radiation force with the restoring force of the harmonic oscillator potential the ion is subject to:

$$z_0 = \frac{\hbar\omega_{\text{laser}}\Gamma/2}{mc\omega_z^2} \left[ \frac{I/I_{\text{Sat}}}{\delta^2/(\Gamma/2)^2 + 1 + I/I_{\text{Sat}}} \right]. \quad (5.15)$$

Figure 5.3 shows fluorescence spectra calculated from equation (5.14) for different parameters. In the figure below, the corresponding distribution of oscillation energies, which appears explicitly in equation (5.13), is plotted. While an oscillating ion is characterised by a delta-function (case (b), green line), adding thermal motion leads to a broader distribution. In case (c), red line, there is still a peak at the original oscillation energy. It is, however, approaching the pure thermal distribution of case (d).

For an ion at temperature  $T$ , Doppler-broadening leads to

$$\sigma = \frac{2\pi}{\lambda} \sqrt{\frac{k_B T}{m}}. \quad (5.16)$$

Solving for the temperature, we obtain

$$T = \frac{m\lambda^2\sigma^2}{4\pi^2 k_B}. \quad (5.17)$$

For calcium ions, this expression evaluates to  $T [\text{mK}] = 0.758 (\sigma [\text{MHz}])^2$ .

For short heating periods, which is the case relevant here,  $\sigma < \Delta_0$ . The spectrum is then best described as oscillatory with an amplitude distribution broadened by thermal effects. It is clearly different from the Voigt profile one would expect in thermal equilibrium.

An example is given in figure 5.4. The blue curve is the power-broadened Lorentzian spectrum of a laser-cooled ion, corresponding to  $S_{\text{cooled}} = S_{\infty}(\delta)$ . The red curve represents the spec-

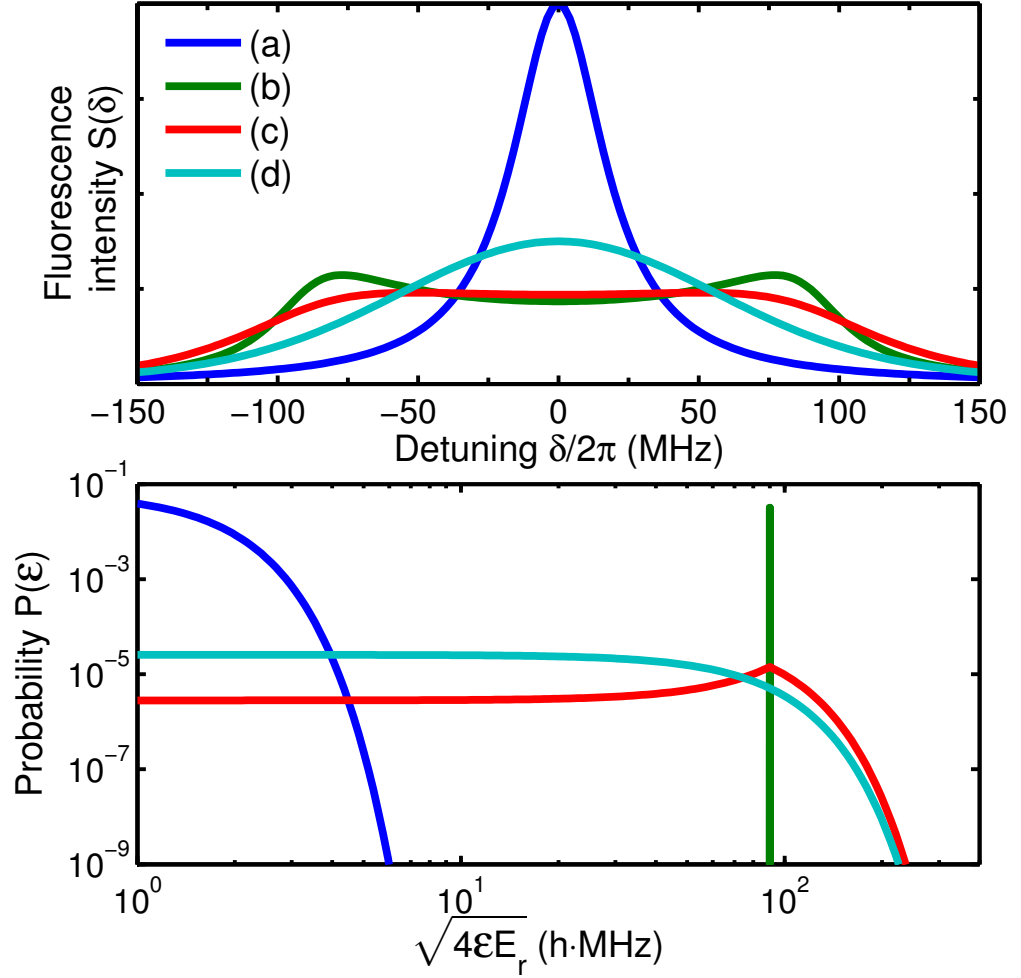


Figure 5.3: Fluorescence spectra  $S(\delta)$  calculated from equation (5.14) for different sets of parameters. (a)  $(\Gamma, \sigma, \Delta_0) = 2\pi \times (40, 1, 0)$  MHz, corresponding to homogeneous broadening (Lorentzian profile); (b)  $(\Gamma, \sigma, \Delta_0) = 2\pi \times (40, 1, 90)$  MHz, corresponding to a cold oscillating ion; (c)  $(\Gamma, \sigma, \Delta_0) = 2\pi \times (40, 50, 90)$  MHz, corresponding to a hot oscillating ion; (d)  $(\Gamma, \sigma, \Delta_0) = 2\pi \times (40, 50, 0)$  MHz, corresponding to a hot ion with no oscillation (Voigt profile). The graph below shows the corresponding probability distributions  $P(\epsilon)$ , plotted as a function of the scaled energy  $\sqrt{4\epsilon E_r}$ .

trum a certain time after switching off the cooling laser, according to equation (5.14). It takes into account thermal effects and oscillatory motion. As expected, the direction of change in fluorescence level depends on detuning. Close to resonance, the fluorescence level drops as a result of switching off the cooling laser, while for large detuning it increases. In figure 5.4, the change in fluorescence level from cooled to heated ion is indicated at two selected detunings.

To illustrate how much of the spectral redistribution is due to the ion's oscillation, we show in the same graph a spectrum with negligible thermal broadening but otherwise identical parameters (green fluorescence trace). At the two indicated detunings, roughly half the effect is due to the harmonic oscillation of the ion. By fitting the spectrum of the ion following a period of suspended cooling using equation (5.14), we can determine the homogeneous linewidth of

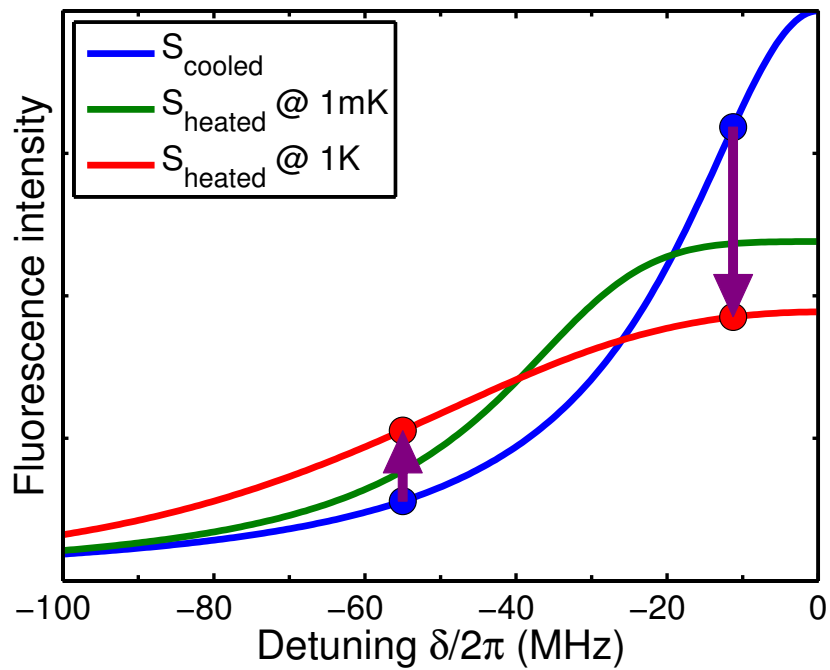


Figure 5.4: Calculated spectra  $S_{\text{cooled}}$  for a cooled ion (blue) and  $S_{\text{heated}}$  for a heated ion at a temperature of 1 K (red). The arrows show the difference in fluorescence level between the two cases. Only part of the effect is due to thermal motion. Another contribution is due to an harmonic oscillation, triggered by switching off the cooling laser. This results in the intermediate spectrum (green), which displays significant line broadening, even for a cold ion at 1 mK.

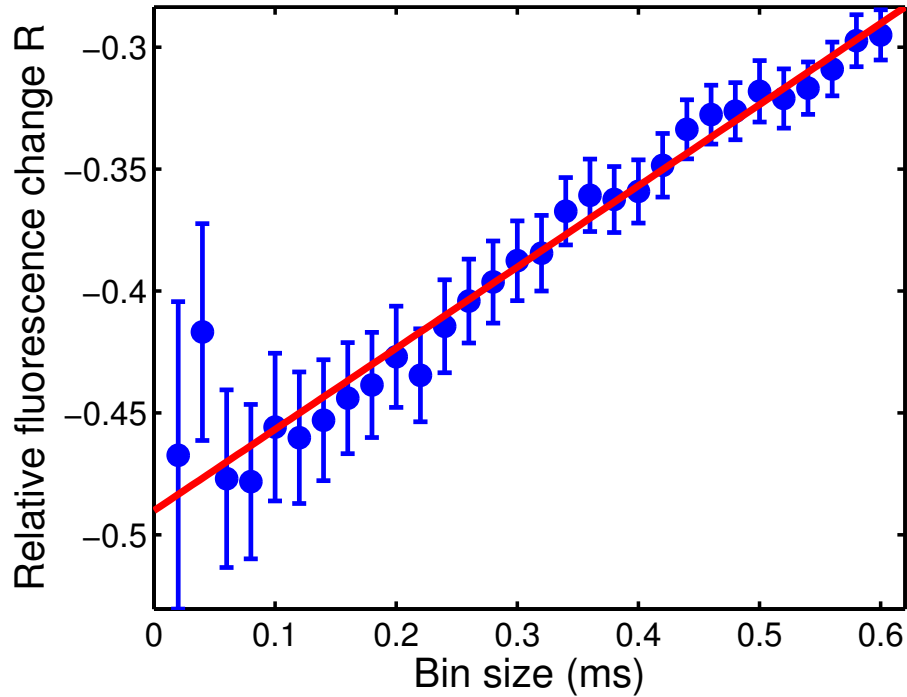


Figure 5.5: Relative change  $R = (S_0/S_\infty - 1)$  of fluorescence in the first bin after recoiling starts, as a function of bin-size. The linear increase is evident and allows us to extrapolate the results to zero bin-size, giving us an accurate value for the relative fluorescence level at  $t=0$ .

the ion, its oscillation amplitude and, most importantly, the correct inhomogeneous linewidth. From the latter the temperature follows directly according to equation (5.17).

### 5.3 Heating Rates

The approach we follow to measure the temperature of the ion is more general than that of Wesenberg *et al.* [39], as it doesn't require any assumptions about details of the recoiling process other than that the fluorescence level rises or falls linearly at the onset of recoiling. This is well confirmed by the experimental data during the first  $600 \mu\text{s}$  (see figure 5.5).

The most important quantity to determine is the fluorescence level at the moment the cooling laser is switched on ( $t=0$ ). In practice, it depends on the size of the time-bins chosen to evaluate detector counts. A larger bin-size decreases fluctuations of the counting statistics but introduces a systematic error caused by the influence of recoiling during the sampling period, which changes the fluorescence level. Immediately following the switch-on of recoiling, a first-order approximation to the behaviour shown in figure 5.2 is possible. For  $t < 600 \mu\text{s} \ll \tau$ , the fluorescence level changes linearly in response to recoiling. This allowed to determine the fluorescence rate at  $t=0$  independently from a model of the recoiling dynamics. Analysis of the fluorescence curves such as in figure 5.2 was done by using varying bin size. For each

bin-size, the ratio of counts in the initial bin ( $S_0$ ) was taken and divided by the counts per bin at equilibrium ( $S_\infty$ ). From the linear change of the fluorescence level, it is then possible to extrapolate to the level that would have been obtained for zero bin-size. The method is illustrated in figure 5.5. It provides a precise value of the fluorescence level at the beginning of recoiling. The change of fluorescence with respect to the equilibrium level obtained in this way is indicated in figure 5.2 by an arrow.

### 5.3.1 Experimental Procedure

The setup used during the heating rate measurements was the same as during the spectroscopy experiments described in chapter 4. A block diagram of this setup is shown in figure 4.1. The ions were produced using two-stage photo-ionisation in vicinity of the trap centre. A single ion was trapped and cooled using both lasers 1 and 2 for cooling and a free space repumper. After optimising the micromotion compensation as described in chapter 3.4.3, laser 2 was switched off and remained so during the measurements described in this chapter. The photo-ionisation lasers and the oven were also turned off during the experiments.

In a first step, the fluorescence spectrum of the Doppler cooled ion was measured, which yielded the equilibrium fluorescence level  $S_\infty(\delta)$  and, from  $S_{\text{cooled}}$  in equation (5.2), the power-broadened linewidth  $\Gamma$ . An example is shown in figure 5.6. It served as a reference for the determination of the heated spectrum, indicating the asymptotic fluorescence level approached in the recoiling process. We also used the results from this initial spectroscopy to establish the detuning parameters to be used during the heating rate measurements. This process required trapping a new ion because the ion was lost when the laser frequency passed the resonance into blue detuning. In a second step, the change of fluorescence level from hot to cold ion was measured,  $S_0$  to  $S_\infty$  for a given detuning and heating duration. To achieve meaningful statistics this process was automated using LabView. For the measurements presented here the number of heating cycles was around 1000. The recoiling curves like that in figure 5.2 were then used to determine the change in fluorescence as described above. The ratio  $R$  of the two values can be compared directly to the corresponding theoretical expression, obtained from the spectra given by equations (5.2) and (5.14).

$$R(\delta, \Gamma, \sigma, \Delta_0) = \frac{S_{\text{heated}}(\delta, \Gamma, \sigma, \Delta_0)}{S_{\text{cooled}}(\delta, \Gamma)} - 1 \stackrel{!}{=} S_0/S_\infty - 1. \quad (5.18)$$

With  $\Gamma$  already determined from the cooled spectrum, fitting the theoretical expression (5.18) to the relative change of the fluorescence level allows to determine the values of thermal broadening  $\sigma$  and oscillatory motion  $\Delta_0$ .

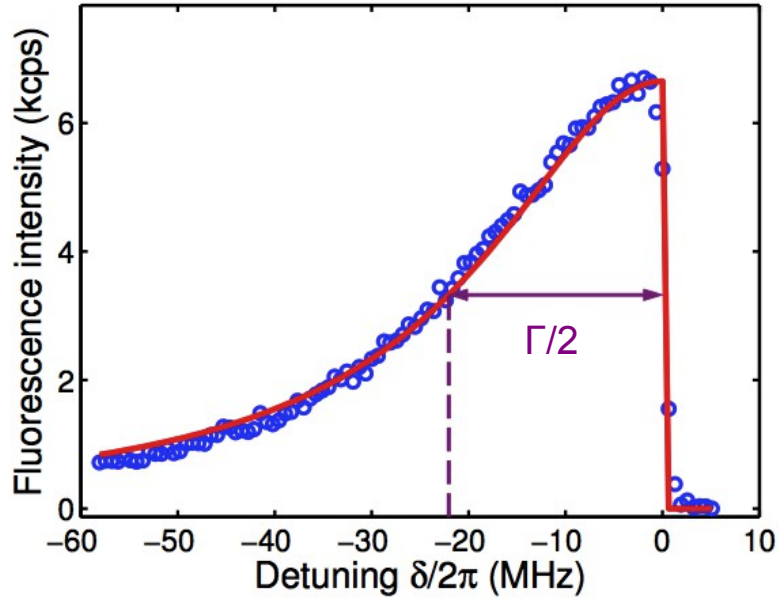


Figure 5.6: Fluorescence spectrum of the Doppler cooled ion, obtained under steady-state conditions. It corresponds to  $S_{\text{cooled}}$  in figure 5.4 and provides the reference level  $S_{\infty}(\delta)$  for measuring the fluorescence of the heated ion. The measured linewidth is  $\Gamma = 2\pi \times 43.8$  MHz, corresponding to a saturation parameter  $s = (\Gamma/\Gamma_0)^2 - 1 = 2.9$ .

As the radiation pressure of the laser depends on detuning, so does the amplitude  $z_0$  of oscillatory motion after the laser is switched off. We accommodate this by using a detuning-dependent expression for  $\Delta_0$ .

$$\Delta_0(\delta) = \Delta_{00} \frac{(\Gamma/2)^2 - (\Gamma_0/2)^2}{(\Gamma/2)^2 + \delta^2}, \quad (5.19)$$

where  $\Gamma_0$  is the natural linewidth of the transition and  $\Delta_{00}$  is the maximum Doppler shift for resonant radiation pressure.

### 5.3.2 Results

The results presented in figure 5.7 show the fit for four different detunings of the laser. The four detunings were chosen as  $\Gamma/4$ ,  $\Gamma/2$ ,  $3\Gamma/4$ , and  $\Gamma$ , where  $\Gamma$  was determined by fitting a Voigt profile to a spectroscopy scan before each experiment. This range of detunings was chosen to confirm that the mechanisms at work are independent of the cooling efficiency. Each data point falls on the theoretical curve corresponding to the value of  $\Gamma$  used for this measurement, as indicated by different colours. It is not possible to fit the data in figure 5.7 with a model neglecting the oscillatory motion of the ion as illustrated by the dashed trace in the figure. These results confirm that the expression (5.14) accurately describes the ion's

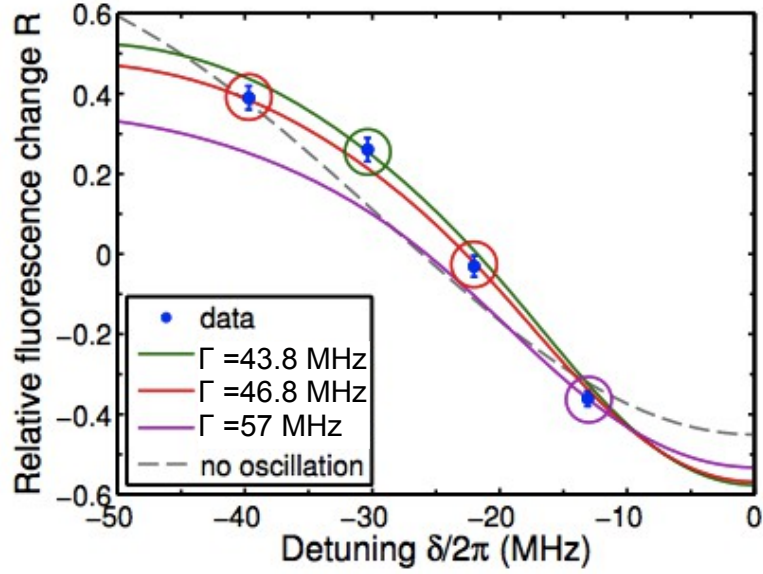


Figure 5.7: Measured values for the relative fluorescence change  $R = (S_0/S_\infty - 1)$  after 500 ms of heating. Three different theoretical fit curves are shown to accommodate the independently determined homogeneous linewidths which are slightly different for each measurement. The oscillatory motion and inhomogeneous linewidth of the ion are obtained from a fit using all data points as  $\Delta_{00} = 2\pi \times 66.4$  MHz and  $\sigma = 2\pi \times 24.5$  MHz. This corresponds to a temperature of  $T = 457$  mK. The dashed line shows the inadequate fit obtained when the oscillatory motion of the ion is neglected.

spectrum at the end of the heating phase.

Having obtained the value of  $\Delta_{00}$  and  $\sigma$  from the fit, the temperature of the ion at the end of the heating period can be extracted using equation (5.17). As long as the laser power is kept constant, which was verified using an optical powermeter,  $\Gamma$  is identical for all measurements. Therefore,  $\sigma$  and hence the temperature is the only unknown parameter in expression (5.18). It can be determined by working at a fixed detuning which we have chosen as  $\delta = -2\pi \times 11$  MHz.

The temperature of the ion for different heating times  $\tau$  was determined in this way. The results are shown in figure 5.8. The increase of temperature with heating time is linear, the slope defining the heating rate of the ion in the 'sandwich' trap. A value of  $dT/d\tau = (2.0 \pm 0.1)$  mK/ms was obtained for the heating rate. Note, that for  $\tau \rightarrow 0$ , the temperature approaches the Doppler limit, as it should be starting from an ion cooled to the Doppler temperature at a level of 1 mK. The effect of neglecting the oscillatory motion of the ion is also demonstrated in figure 5.8. The green circles indicate the temperatures that would have been obtained in this case. The apparent heating rate would have been 15% smaller, but the biggest problem is the resulting offset of 570 mK at  $\tau = 0$ , three orders of magnitude larger

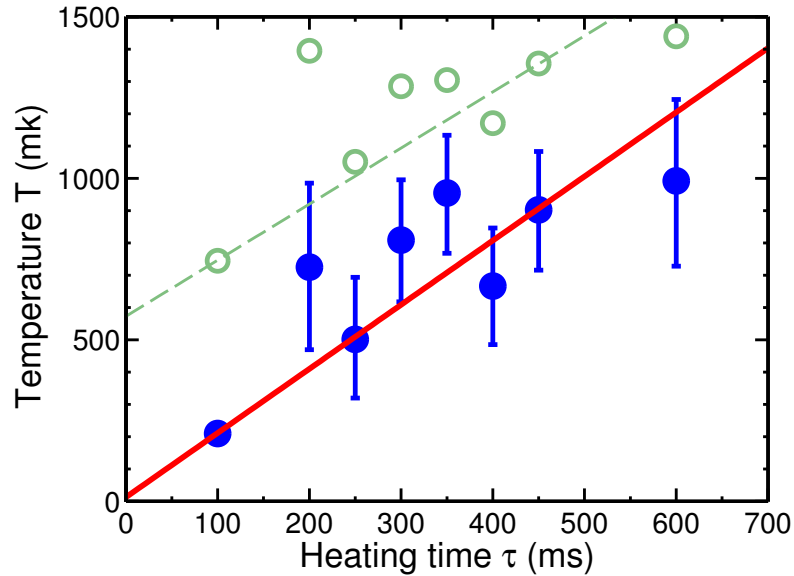


Figure 5.8: Measured temperature of the ion as a function of heating time. The heating rate is determined from the slope of a linear fit (solid line) to be  $dT/d\tau = (2.0 \pm 0.1)$  mK/ms. The temperature measurement is most precise for the data point at  $\tau = 100$  ms, which has error bars smaller than the size of the marker. The open green circles indicate the temperature values that would have been obtained from a model neglecting oscillatory motion of the ion. The corresponding linear fit, shown as a dashed line, wrongly results in a slightly lower heating rate and a large temperature offset of 570 mK.

than the Doppler temperature of the ion. This is clearly impossible, as at  $\tau \approx 0$ , no thermal heating could have occurred and hence no measurable increase in temperature. Observation of substantial temperature offsets in other heating-rate experiments shows that radiation pressure induced oscillations of the ion are a phenomenon that must be taken into account to arrive at correct values for the ion temperature.

The spectral density of electric field fluctuations is given by Turchette *et al.* [35] as  $S_E(\omega_n) \approx \frac{dn}{dt} \frac{4m_{Ca}\hbar\omega_n}{e^2}$ , where  $n$  is the number of motional quanta,  $m_{Ca}$  the mass of the ion, and  $\omega_n$  the secular frequency of the trap. From the observed heating rate, a spectral density of electric field fluctuations of  $S_E(\omega) = 3 \times 10^{-10} \text{V}^2/\text{m}^2\text{Hz}$  is obtained at an ion-electrode distance of  $166 \mu\text{m}$  and for a secular frequency of 1.5 MHz. This compares well with measurements of heating in other traps of the same size [41, 42]. This is remarkable, given the limited surface quality of the copper electrodes, which is a potential source of increased heating, and the presence of stray fields found in micromotion compensation.

## 5.4 Conclusions

This chapter presents a thorough measurements of the heating rates of an ion in the 'sandwich' trap. The measurements employed the Doppler-recooling method. An analytical expression

---

for the ion spectrum which includes homogeneous and inhomogeneous broadening, and takes into account harmonic oscillation of the ion induced by radiation pressure was derived to analyse the results. The resulting heating rate of  $dT/d\tau = (2.0 \pm 0.1)$  mK/ms is comparable to that of other traps with a similar size in spite of the surface roughness and the unusual electrode material. It is worth noting that for experiments with ions in cavities, it is sufficient to reach the Lamb-Dicke regime of ion localisation, which extends to a thermal excitation of a few hundred vibrational quanta.

At the measured heating rate, the system will remain in the Lamb-Dicke regime for times of the scale of milliseconds, which is long compared to cavity-enhanced ion-photon coupling rate on the order of MHz. The observed heating rate is therefore no constraint for achieving controlled ion-cavity interaction in the trap.

## Chapter 6

# Coupling Ions and Cavity Mode

### 6.1 Introduction

An important step towards cavity quantum electrodynamics (cavity QED) experiments is coupling the ion to the cavity mode. Both traps reported on in this thesis are designed with the cavity axis to be perpendicular to the trap axis. In combination with a linear trap this has the advantage of allowing us to move the ions in the horizontal direction within the cavity mode using the axial dc potential only. This chapter explains the atom light interactions for a three-level  $\Lambda$  system, introduces the effects of placing the ion into a resonant optical cavity and describes the experimental cavity used with the 'alumina' trap. We also report on first results in aligning the cavity mode with the ion position in the 'alumina' trap.

### 6.2 Theory

So far we have been able to treat the ion as a two-level system in our experiment because we used the repumper scheme described in chapter 4. For the spectroscopy measurements this was a very useful deviation from the more common way to repump directly via the  $P_{1/2}$  state which can result in coupling the  $D_{3/2}$  and  $S_{1/2}$  states with adverse effects on the cooling of the ion. However, it is in fact this coupling that becomes a desired effect for the experiments that the trap was designed for. Hence it becomes necessary to expand the model treating the atom light interaction to the  $\Lambda$  system.

#### 6.2.1 Optical Bloch Equations in a $\Lambda$ System

The equations derived in sections 2.2.1 and 2.2.1 have to be modified to adequately describe the interaction between the ion and the cavity field. Janik *et al.* [43] derive the three-level

Bloch equations to calculate the population of the  $P_{1/2}$  level (state  $|P\rangle$ ). In this model the  $S_{1/2}$  level is represented as state  $|S\rangle$ , and the  $D_{3/2}$  level as state  $|D\rangle$  (Figure 6.1). We neglect the Zeeman sublevels in this derivation.

The possibility of the two-photon resonance requires accounting for coherences. The five

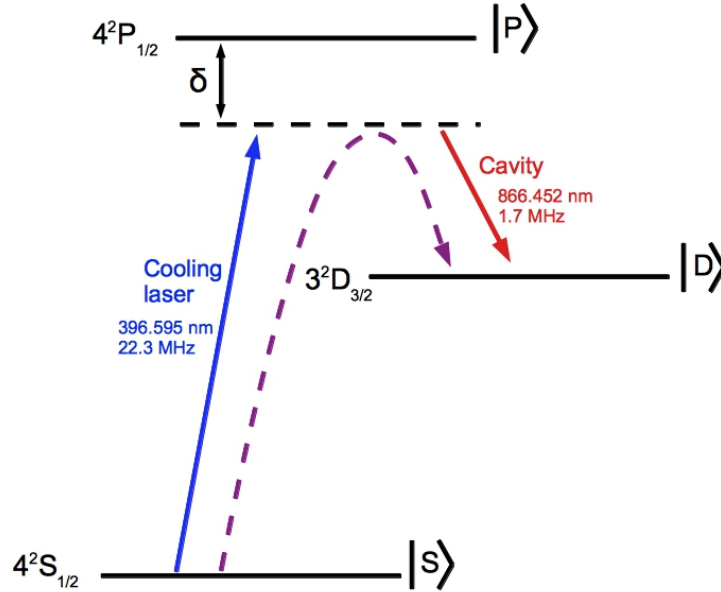


Figure 6.1: Simplified level structure of  $^{40}\text{Ca}^+$  with the transitions relevant to our experiments. The  $D_{3/2}$  state is metastable and has a lifetime of 1.2s. If the cooling laser and the cavity are resonantly detuned from the excited state by  $\delta$ , the population of the  $P_{1/2}$  state is zero as the ion can make the transition directly from the  $S_{1/2}$  to the  $D_{3/2}$  state.

independent equations for the density matrix elements are given in Gray *et al.* [44] after a more thorough derivation as

$$\frac{d\rho_{SS}}{dt} = i\frac{\Omega_{\text{blue}}}{2} (\rho_{SP} - \rho_{PS}) + \Gamma_{\text{blue}}\rho_{PP}, \quad (6.1)$$

$$\frac{d\rho_{DD}}{dt} = i\frac{\Omega_{\text{red}}}{2} (\rho_{DP} - \rho_{PD}) + \Gamma_{\text{red}}\rho_{PP}, \quad (6.2)$$

$$\frac{d\rho_{SD}}{dt} = i \left[ (\delta_{\text{red}} - \delta_{\text{blue}}) \rho_{SD} + \frac{\Omega_{\text{red}}}{2} \rho_{SP} - \frac{\Omega_{\text{blue}}}{2} \rho_{PD} \right], \quad (6.3)$$

$$\frac{d\rho_{SP}}{dt} = i \left[ \frac{\Omega_{\text{blue}}}{2} (\rho_{SS} - \rho_{PP}) + \frac{\Omega_{\text{red}}}{2} \rho_{SD} - \delta_{\text{blue}} \rho_{SP} \right] - \frac{\Gamma}{2} \rho_{SP}, \quad (6.4)$$

$$\frac{d\rho_{DP}}{dt} = i \left[ \frac{\Omega_{\text{red}}}{2} (\rho_{DD} - \rho_{PP}) + \frac{\Omega_{\text{blue}}}{2} \rho_{DS} - \delta_{\text{red}} \rho_{DP} \right] - \frac{\Gamma}{2} \rho_{DP}, \quad (6.5)$$

where  $\Omega_{\text{blue}}$  and  $\Omega_{\text{red}}$  are the Rabi frequencies for the  $S_{1/2} \rightarrow P_{1/2}$  transition and the  $D_{3/2} \rightarrow P_{1/2}$  transition respectively. Similarly  $\delta_{\text{blue}}$  and  $\delta_{\text{red}}$  are the detunings of the cooling laser and the repumper laser or cavity from the excited state,  $P_{1/2}$ .  $\Gamma$  is the total decay rate from the  $P_{1/2}$  state and is the sum of the decay rates to the ground state ( $\Gamma_{\text{blue}}$ ) and the metastable  $D_{3/2}$  level ( $\Gamma_{\text{red}}$ ).

The steady state solution for the  $P_{1/2}$  state population is

$$\rho_{PP} = \frac{4(\delta_{\text{blue}} - \delta_{\text{red}})^2 \Omega_{\text{blue}}^2 \Omega_{\text{red}}^2 \Gamma}{Z}, \quad (6.6)$$

where  $Z$  is defined as

$$\begin{aligned} Z = & 8 (\delta_{\text{blue}} - \delta_{\text{red}})^2 \Omega_{\text{blue}}^2 \Omega_{\text{red}}^2 \Gamma + 4 (\delta_{\text{blue}} - \delta_{\text{red}})^2 \Gamma^2 Y \\ & + 16 (\delta_{\text{blue}} - \delta_{\text{red}})^2 [\delta_{\text{blue}}^2 \Omega_{\text{red}}^2 \Gamma_{\text{blue}} + \delta_{\text{red}}^2 \Omega_{\text{blue}}^2 \Gamma_{\text{red}}] \\ & - 8 \delta_{\text{blue}} (\delta_{\text{blue}} - \delta_{\text{red}}) \Omega_{\text{red}}^4 \Gamma_{\text{blue}} + 8 \delta_{\text{red}} (\delta_{\text{blue}} - \delta_{\text{red}}) \Omega_{\text{blue}}^4 \Gamma_{\text{red}} \\ & + (\Omega_{\text{blue}}^2 + \Omega_{\text{red}}^2)^2 Y, \end{aligned} \quad (6.7)$$

with  $Y = \Omega_{\text{blue}}^2 \Gamma_{\text{red}} + \Omega_{\text{red}}^2 \Gamma_{\text{blue}}$ .

From equation 6.6 we can see two effects which are relevant to the work presented in this

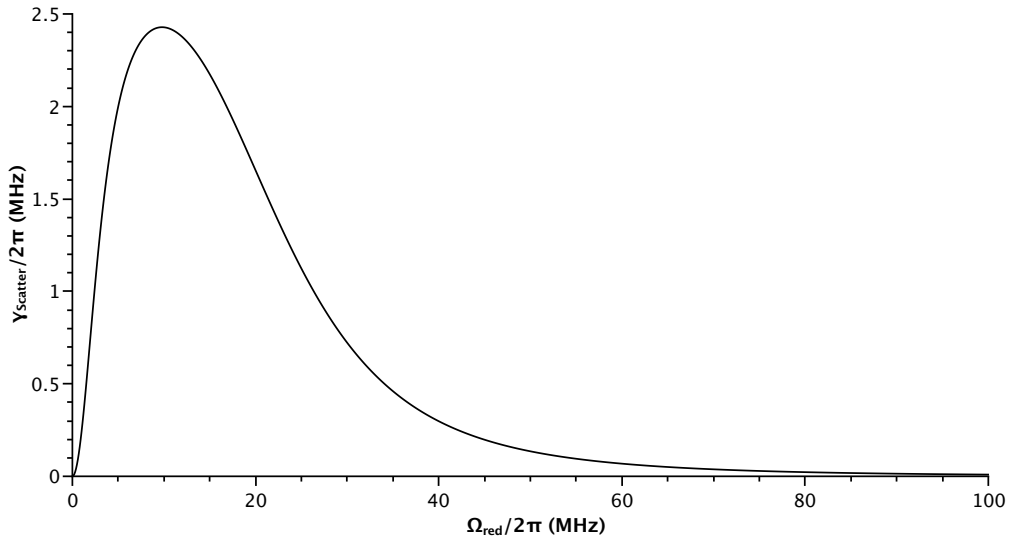


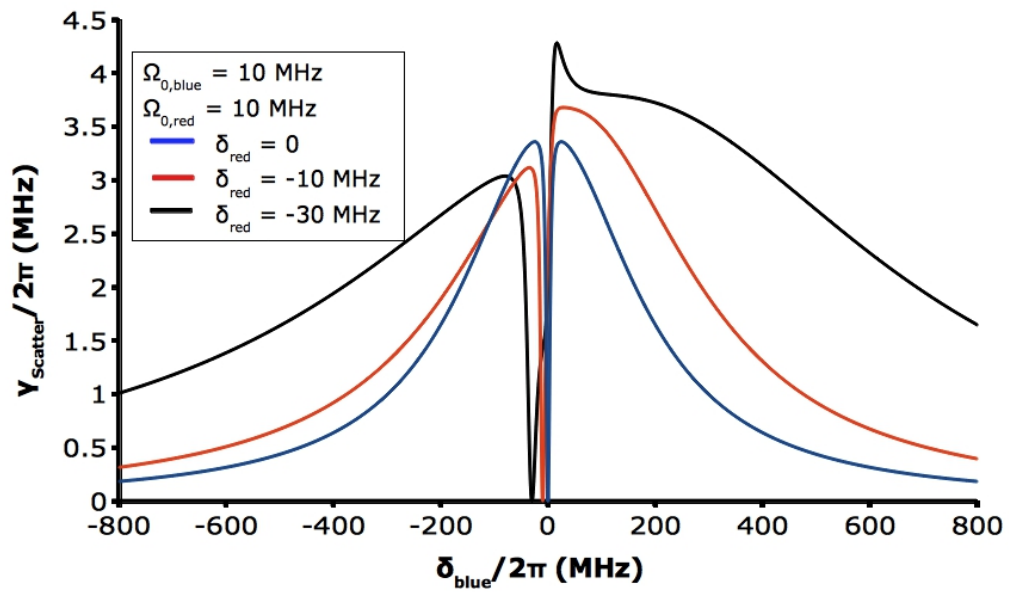
Figure 6.2: Initially the fluorescence increases with repumper intensity as the repump process becomes more efficient. If the intensity is increased further the ac Stark effect shifts the  $P_{1/2}$  level away from resonance and the fluorescence decreases.

thesis. Firstly, the cooling fluorescence dependence on the power in the repumping laser is not trivial. Figure 6.2 shows a plot of this dependency in the  $\Lambda$  model for cooling intensity  $\Omega_{\text{blue}} = 2\pi \times 10$  MHz, zero detuning for the cooling laser and  $-2\pi \times 10$  MHz detuning for the

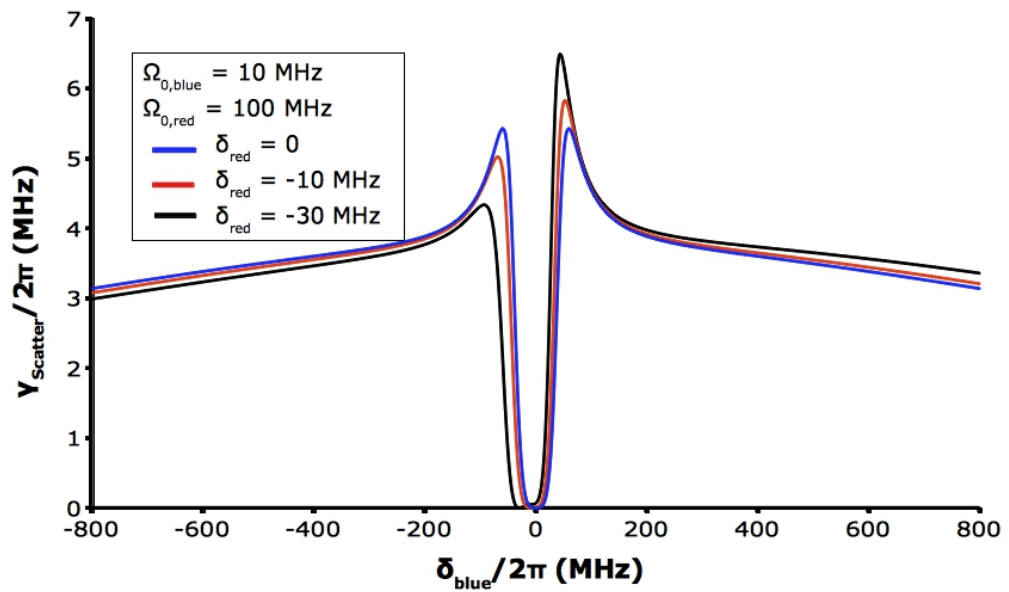
repumper laser. Initially the fluorescence level rises as the ion is being repumped from the  $D_{3/2}$  state more efficiently. However, this process does not continue indefinitely. Eventually the large intensity introduces an ac Stark shift and the lasers are no longer resonant with the atomic transition causing a drop in the fluorescence level. Since the cooling of the ion relies on a large number of scattering events, a reduced scattering rate results in a slower cooling process. This also gives the ions more time to heat up in between scattering events, and hence the final temperature that can be reached is higher.

Secondly, when the detuning of cooling and repumper laser is equal ( $\delta_{\text{blue}} = \delta_{\text{red}}$ ) a two-photon resonance occurs and the population of the  $P_{1/2}$  level is zero, and hence there will be no fluorescence. The ion can make a transition directly from the  $S_{1/2}$  to the  $D_{3/2}$  level bypassing the  $P_{1/2}$  level completely. This is known as a Raman transition or dark resonance. Figure 6.3 shows plots of the fluorescence rate according to the three-level Bloch equations for different repump intensities and detunings. The two-photon (Raman) resonance is a pronounced feature in all plots and widens with increasing repumper intensity. Plot 6.3a shows a lower repump intensity with a Rabi frequency similar to that of the cooling transition. As the detuning from resonance increases the fluorescence profile becomes more asymmetric. With increasing negative repumper detuning the two-photon resonance is shifted to a negative detuning with respect to resonance. For larger repump intensity the asymmetry is also visible but is overshadowed by the widening of the dip.

The Raman resonance has an effect on the efficiency of the Doppler cooling employed in our experiments. As the cooling relies on the repeated loss of energy by the ion equal to  $h\delta$  as the ion transitions from the  $P_{1/2}$  to the  $S_{1/2}$  state, an ion that never populates the  $P_{1/2}$  state is not subject to a cooling effect. For efficient cooling the detunings of the cooling and repumper lasers from the  $P_{1/2}$  state need to differ, that is  $\delta_{\text{red}} \neq \delta_{\text{blue}}$ .



(a) Low repumper laser intensity.



(b) High repumper laser intensity

Figure 6.3: Theoretical cooling fluorescence spectrum for the three-level  $\Lambda$  structure of the  $^{40}\text{Ca}^+$  ion. The first graph shows different repumper detunings low repumper power, the second graph shows the effect for a much higher light intensity. ( $\Omega_{0,\text{red}} = 2\pi \times 10$  MHz and  $\Omega_{0,\text{red}} = 2\pi \times 100$  MHz respectively). The cooling power is the same for both graphs. The two-photon resonance is notably wider for the higher intensity and the asymmetry increases with the repumper detuning.

### 6.2.2 Fabry - Pérot Cavities

Figure 6.4 shows the basic configuration of a Fabry-Pérot optical cavity. It consists of two highly reflective mirrors ( $M_1$  and  $M_2$ ) with radii of curvature  $R_1$  and  $R_2$  respectively, placed a distance  $L_{\text{Cav}}$  apart from each other. The mirrors have transmissivities  $T_1$  and  $T_2$ .

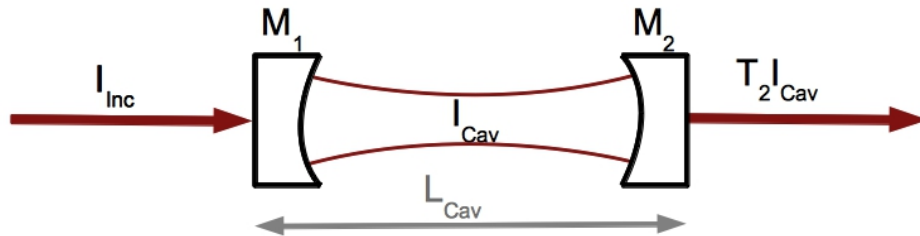


Figure 6.4: Fabry - Pérot Cavity consisting of mirrors  $M_1$  and  $M_2$  with radii of curvature  $R_1$  and  $R_2$  and transmissivities  $T_1$  and  $T_2$  respectively.

#### Cavity Modes

Light beams differ from plane waves in that they have non-uniform intensity distributions. The simplest imaginable light beam has a Gaussian intensity profile, and is often called the fundamental mode. Its spot size  $w(x)$  and the radius of curvature of its wavefront  $R(x)$  vary as a function of the position from the waist  $w_0$  (where the radius of curvature is infinity) according to

$$w(x) = w_0 \sqrt{1 + \left(\frac{x}{x_R}\right)^2}, \quad (6.8)$$

and

$$R(x) = x + \frac{x_R^2}{x}, \quad (6.9)$$

respectively.  $x_R = \pi w_0^2 / \lambda$  is the so-called Rayleigh range.

An optical cavity imposes boundary conditions on the light modes that can exist between its mirrors. Longitudinally the resonance condition for a cavity is that after one round trip the light arrives at the incoupling mirror in phase with the incident light, that is the phase difference from one mirror to the other is an integer multiple of  $\pi$ . In this way the light can interfere constructively and the intensity in the cavity builds up. The parameters  $w$  and  $R$  describe transverse modes of all order, however the phase velocities are different for the different transverse modes.

The transverse modes or spatial configurations inside a cavity are described using Hermite-

Gaussian modes or Laguerre-Gaussian modes. Hermite-Gaussian modes have rectangular symmetry and the horizontal and vertical mode order are denoted by  $m$  and  $n$  ( $\text{TEM}_{mn}$ ), Laguerre-Gaussian modes have radial symmetry. When scanning the cavity length both types of modes can be observed, but for simplicity only Hermite-Gaussian modes are explained further here. For a cavity aligned with the  $x$ -axis the spatial intensity distribution of the electric field of these modes is

$$I_{mn}(z, y) = I_0 \left[ H_m \left( \frac{\sqrt{2}z}{w(x)} \right) \exp \left( \frac{-z^2}{w(x)^2} \right) \right]^2 \left[ H_n \left( \frac{\sqrt{2}y}{w(x)} \right) \exp \left( \frac{-y^2}{w(x)^2} \right) \right]^2, \quad (6.10)$$

where  $I_0$  is the intensity at the centre of the beam at its Gaussian beam waist. Figure 6.5 shows the Hermite-Gaussian transverse modes for  $m, n = 0, 1, 2, 3$ . The equation for the most fundamental mode,  $\text{TEM}_{00}$  is

$$I_{00}(z, y) = I_0 \left[ \left( \frac{\sqrt{2}z}{w(x)} \right) \exp \left( \frac{-z^2}{w(x)^2} \right) \right]^2 \left[ \left( \frac{\sqrt{2}y}{w(x)} \right) \exp \left( \frac{-y^2}{w(x)^2} \right) \right]^2. \quad (6.11)$$

Taking into account the transverse modes the resonance condition therefore depends on the

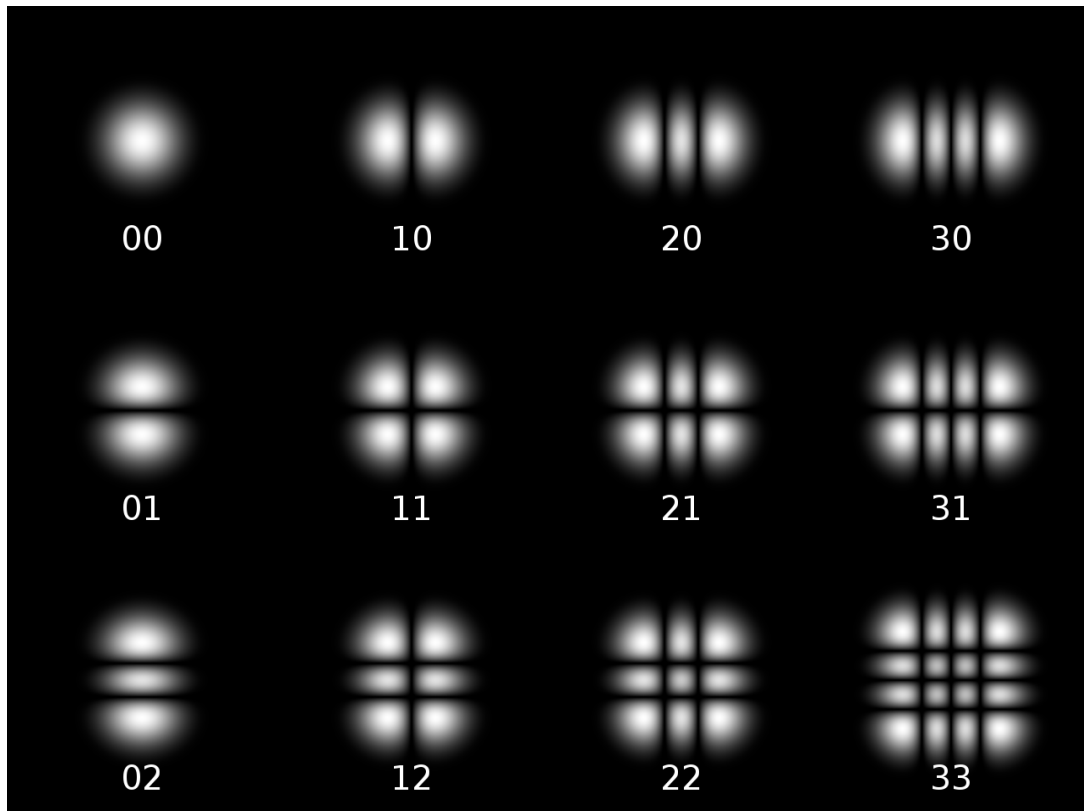


Figure 6.5: Hermite-Gaussian modes  $\text{TEM}_{mn}$  (<http://en.wikipedia.org/wiki/File:Hermite-gaussian.png>)

$m$ ,  $n$  and longitudinal mode number  $n_{\text{axial}}$  [45]

$$(1 + n_{\text{axial}})\pi = kL_{\text{Cav}} - 2(m + n + 1) \arctan \frac{\lambda}{2x_R}. \quad (6.12)$$

The spacing between longitudinal resonances given by the free spectral range  $\text{FSR} = \frac{c}{2L_{\text{Cav}}}$ . The resonance frequency  $\nu$  for a resonator with two mirrors of equal curvature is thus

$$\nu/\text{FSR} = (n_{\text{axial}} + 1) + \frac{1}{\pi}(m + n + 1) \arccos \left( 1 - \frac{L_{\text{Cav}}}{R} \right). \quad (6.13)$$

### Photon Decay Rate - $\kappa$

The cavity decay rate is a measure of how quickly the electric field within a cavity decays. It is important for classifying the coupling strength of ion and cavity field. If at  $t = 0$  there are  $N_{\text{Photon}}$  photons in the cavity, and the cavity consists of two mirrors with transmissivity  $T$ , which are a distance  $L_{\text{Cav}}$  apart, then after one round trip of the cavity ( $t = 2n_{\text{refr}}L_{\text{Cav}}/c$ , where  $n_{\text{refr}}$  is the index of refraction of the medium between the mirrors) the number of photons remaining in the cavity is  $N_{\text{Photon}}/T^2$ . The change in the number of photons can be written as

$$\frac{dN_{\text{Photon}}}{dt} = -\frac{c(1 - 1/T)}{n_{\text{refr}}L_{\text{Cav}}} N_{\text{Photon}}. \quad (6.14)$$

The solution is  $N_{\text{Photon}} = N_{0,\text{Photon}}e^{-2\kappa t}$ , with  $\kappa = \frac{c(1-1/T)}{2n_{\text{refr}}L_{\text{Cav}}}$ . For high quality mirror coatings of transmissions of the order of 100s of ppm or less we can assume  $1/T \sim 1$ . Using  $\mathcal{F} = \frac{\pi \left( \frac{1}{R_1 R_2} \right)^{1/4}}{1 - \sqrt{\frac{1}{R_1 R_2}}}$  for the cavity finesse and  $\Delta\omega = \frac{\pi c}{n_{\text{refr}} \mathcal{F} L_{\text{Cav}}}$  for the linewidth in equation 6.14, we can conclude that  $2\kappa = \Delta\omega$ .

### 6.2.3 Ion - Cavity Coupling

If an ion is placed inside an optical cavity as described in the previous section the restrictions on the available modes can be expected to affect the optical properties of an ion behaving according to the three-level Bloch equations derived in section 6.2.1. The case where the cavity resonance coincides with an atomic transition is of particular interest, as it allows ion and cavity to resonantly exchange excitation, and thus the ion - cavity coupling can be viewed in a similar way as a free space laser in the three-level Bloch equations.

### Jaynes - Cummings Model

The interaction between a two - level atom and a single mode cavity in the regime of cavity QED was first analysed by Jaynes and Cummings in 1963 [46]. In this model the electromagnetic field of the cavity mode is quantised, and its state vector is a superposition of photon - number states (Fock states),  $|n\rangle$ . The energy is then  $\hbar\omega_{\text{Cavity}}(n + 1/2)$ , where  $\hbar\omega_{\text{Cavity}}$  is the energy of a photon. Analogous to the quantum harmonic oscillator there are photon annihilation ( $a$ ) and creation ( $a^\dagger$ ) operators resulting in the Hamiltonian of the cavity field

$$H_{\text{Cavity}} = \hbar\omega_{\text{Cavity}} \left( a^\dagger a + \frac{1}{2} \right) . \quad (6.15)$$

The Hamiltonian for a two-level atom with ground state  $|D\rangle$  and excited state  $|P\rangle$ , with energies  $\hbar\omega_D$  and  $\hbar\omega_P$ , is

$$H_{\text{Atom}} = \hbar\omega_D |D\rangle \langle D| + \hbar\omega_P |P\rangle \langle P| . \quad (6.16)$$

In a loss - less system any change in the number of photons must result in a change in the ion's internal state. So the interaction between ion and cavity can be expressed by [47]

$$H_{\text{Int}} = -\hbar g_0(\vec{r}) \left[ |P\rangle \langle D| a + a^\dagger |D\rangle \langle P| \right] , \quad (6.17)$$

where  $g_0(\vec{r})$  is the coupling strength between the ion and the cavity [12]

$$g_0(\vec{r}) = \sqrt{\frac{\mu_{\text{PD}}^2 \omega}{2\epsilon_0 \hbar V_{\text{mode}}}} u(\vec{r}) . \quad (6.18)$$

$\mu_{\text{PD}}$  is the dipole matrix element of the transition,  $V_{\text{mode}}$  the mode volume, and  $u(\vec{r})$  describes the spatial dependence of the electric field amplitude. For the TEM<sub>00</sub> mode the spatial dependence perpendicular to the cavity axis follows a Gaussian, while along the cavity axis it is sinusoidally varying standing wave pattern. Because we are considering an ion within a cavity we don't need to sum over all available eigenmodes of the light field but only have to consider the modes of the cavity. Furthermore by choosing the cavity parameters carefully it is possible to reduce this even further to a single mode.

The cavity's mode volume is given by

$$V_{\text{Mode}} = \int |u(\vec{r})|^2 d^3r , \quad (6.19)$$

which for lowest order transverse mode is

$$V_{\text{TEM}_{00}} = \frac{2}{3}\pi w_0^2 L_{\text{Cav}}. \quad (6.20)$$

Equation 6.18 suggests that a small mode volume leads to increase coupling. The dependency of the mode volume suggests that a small cavity waist may be advantageous. A concentric cavity produces a diffraction limited waist size, so may be considered the best choice to achieve this, and this is in fact what Rainer Blatt's group in Innsbruck use in their experiments. The large disadvantage of concentric cavities is the difficulty of their alignment. This is the reason we choose not to use these and rather try to increase the coupling strength in our experiments by reducing the cavity length.

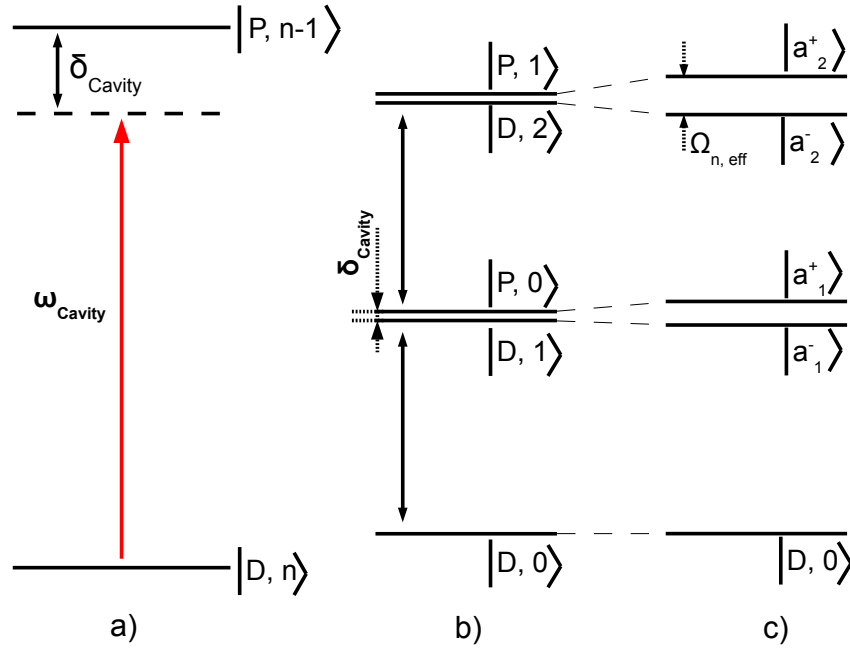


Figure 6.6: (a) Level scheme for a two-level atom with ground state  $|D\rangle$  and excited state  $|P\rangle$  coupled to a cavity containing  $n$  photons. In the dressed atom picture this gives two degenerate energy states for all but the  $|D, 0\rangle$  state if the cavity detuning is zero with respect to the resonance and the ion is outside the cavity. If the detuning is non-zero as portrayed in the (b) the levels are split by the cavity detuning  $\delta_{\text{Cavity}}$ . (c) If the atom is inside the cavity the levels are split by the effective Rabi frequency  $\Omega_{n, \text{eff}}$ .

The total Hamiltonian of the system is the sum of equations 6.15, 6.16, and 6.17.

In the rotating wave approximation the eigenfrequencies of this Hamiltonian [47] are

$$\omega_n^\pm = \omega_{\text{Cavity}} \left( n + \frac{1}{2} \right) + \frac{1}{2} \left( \delta_{\text{Cavity}} \pm \sqrt{4ng_0^2 + \delta_{\text{Cavity}}^2} \right). \quad (6.21)$$

So the atom - cavity interaction splits the photon number states into doublets of non - degenerate dressed eigenstates which are split by  $\Omega_{n,\text{eff}} = \sqrt{4ng_0^2 + \delta_{\text{cavity}}^2}$ , which is the effective Rabi frequency of the oscillation between the dressed states  $|D, n\rangle$  and  $|P, n-1\rangle$ . A distinct feature is the fact that an excited atom placed within an empty cavity is enough to start the oscillation. These oscillation are thus called vacuum-Rabi oscillations. Figure 6.6 illustrates the dressed atom level scheme for a two-level system.

### Three - Level Atom

So far we have analysed the ion - cavity coupling for a two-level system. Calcium is however a three-level system as shown in figure 6.1 and 6.7 and so we need to extend this idea further. The interaction Hamiltonian for this type of system is [47]

$$H_{\text{Int}} = \hbar \left[ \delta |S\rangle \langle S| + \delta |D\rangle \langle D| - g_0 \left( |P\rangle \langle D| a + a^\dagger |D\rangle \langle P| \right) - \frac{1}{2} \Omega_{\text{blue}} \left( |P\rangle \langle S| + |S\rangle \langle P| \right) \right]. \quad (6.22)$$

In equation 6.22 we have already assumed the condition for the Raman resonance, that is the

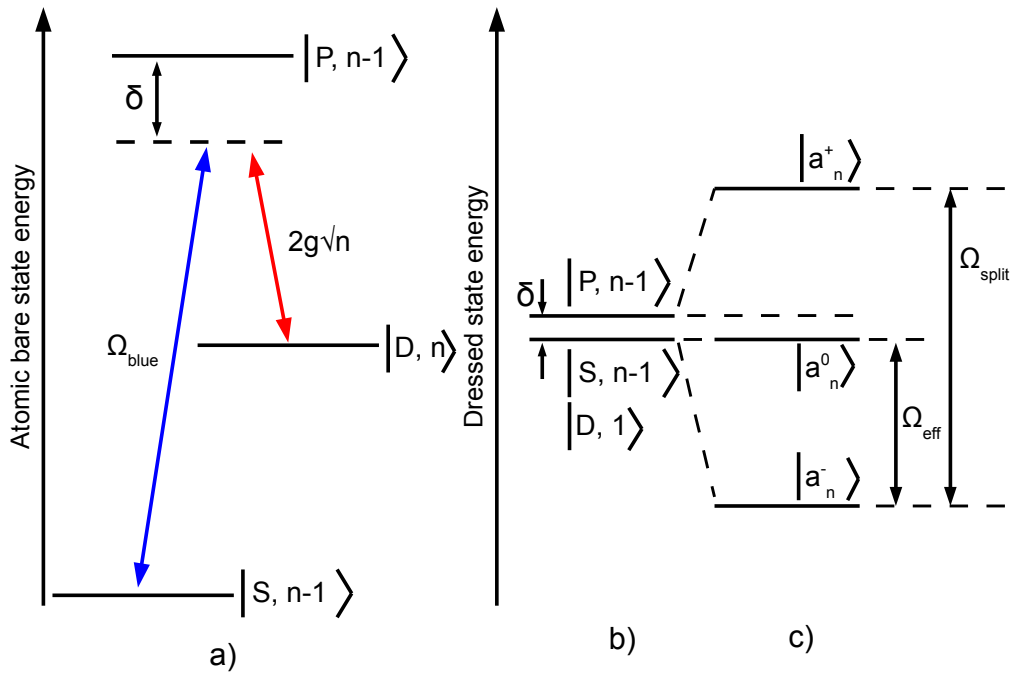


Figure 6.7: (a) Level scheme for a three-level atom driven by the cooling laser field on the  $|S\rangle \leftrightarrow |P\rangle$  transition and coupled to a cavity containing  $n$  photons on the  $|D\rangle \leftrightarrow |P\rangle$  transition. (b) Dressed atom level scheme for an atom interacting with cooling laser and cavity for vanishing coupling strength. (c) The triplet of states is split by  $\Omega_{\text{split}} = \sqrt{4ng^2 + \Omega_{\text{blue}}^2 + \delta^2}$ . For detunings  $\delta \gg \Omega$  the Raman transition ( $|S, n-1\rangle \leftrightarrow |S, n\rangle$ ) is driven at the effective Rabi frequency  $\Omega_{\text{eff}} = \frac{1}{2} (\Omega_{\text{split}} - |\delta|) \approx (4ng^2 + \Omega_{\text{blue}}^2) / |4\delta|$ .

cooling laser is detuned from state  $|P\rangle$  by the same amount as the cavity. For any number of photons  $n$  this interaction Hamiltonian couples only the three states  $|S, n-1\rangle$ ,  $|P, n-1\rangle$ , and  $|D, n\rangle$ . The eigenfrequencies of the system are

$$\omega_n^0 = \omega_{\text{Cavity}} \left( n + \frac{1}{2} \right) \text{ and} \quad (6.23)$$

$$\omega_n^\pm = \omega_{\text{Cavity}} \left( n + \frac{1}{2} \right) + \frac{1}{2} \left( \delta \pm \sqrt{4ng_0^2 + \Omega_{\text{blue}}^2 + \delta^2} \right). \quad (6.24)$$

The eigenstates are now Jaynes-Cummings state triplets:

$$|\Phi_n^0\rangle = \cos \Theta |S, n-1\rangle - \sin \Theta |D, n\rangle \quad (6.25)$$

$$|\Phi_n^+\rangle = \cos \Phi \sin \Theta |S, n-1\rangle - \sin \Phi |P, n-1\rangle + \cos \Phi \cos \Theta |D, n\rangle \quad (6.26)$$

$$|\Phi_n^-\rangle = \sin \Phi \sin \Theta |S, n-1\rangle - \cos \Phi |P, n-1\rangle + \sin \Phi \cos \Theta |D, n\rangle, \quad (6.27)$$

where  $\Theta$  and  $\Phi$  are mixing angles given by

$$\tan \Theta = \frac{\Omega_{\text{blue}}}{2g_0\sqrt{n}} \quad \text{and} \quad \tan \Phi = \frac{\sqrt{4ng_0^2 + \Omega_{\text{blue}}^2}}{\sqrt{4ng^2 + \Omega_{\text{blue}}^2 + \delta^2 - \delta}}, \quad (6.28)$$

and  $\Omega_{\text{blue}}$  and  $g$  are real.

There are a few interesting features to this system. The triplet levels are degenerate if no light field or cavity coupling is present. As soon as either is provided and the Rabi frequencies are non-zero the levels split. The state  $|\Phi_n^0\rangle$  is called a dark state, because the population of this state can't be lost by spontaneous emission, and it can only be depopulated if it absorbs light from the cooling laser. The level is also not subject to an energy shift. It is a superposition of the ground state of the ion with no photon present and the metastable D level with a cavity photon present. These two states constitute the two levels involved in the Raman transition considered earlier and thus for this state there is no observation of cooling fluorescence.

In the limit  $\Omega_{\text{blue}} \rightarrow 0$  the the states  $|\Phi_n^\pm\rangle$  correspond to the Jaynes-Cummings doublet described in the previous section and  $|\Phi_n^0\rangle$  to  $|S, n-1\rangle$ .

### Coupling Regimes

Coupling between ion and cavity is categorised into two regimes, strong and weak coupling. These regimes are defined by the relationship between the coupling constant  $g_0$  and the damping factors present in a real system: the cavity decay rate  $\kappa$  and the rate of spontaneous emission into free space  $\Gamma$ . Coupling is considered weak if  $\kappa, \Gamma \gg g_0$  and strong

if  $g_0 \gg \kappa, \Gamma$ . For any chosen atomic species  $\Gamma$  is fixed and hence only the  $\kappa$  and  $g_0$  are available to influence the coupling in experiment.  $\kappa$  was discussed in section 6.2.2 and from there it becomes apparent that this parameter depends linearly on  $1/L_{\text{Cav}}$  as well as  $1/\mathcal{F}$ .  $g_0 \propto 1/\sqrt{V_{\text{Mode}}}$  (see equation 6.20), so with the waist being related to the cavity length via  $w_0(L_{\text{Cav}}) = \sqrt{\frac{\lambda}{2\pi}} (L_{\text{Cav}} (2R - L_{\text{Cav}}))^{\frac{1}{4}}$ , where  $R$  is the radius of curvature of the mirrors,  $g_0$  varies as  $1/L_{\text{Cav}}^{3/4}$ . A shorter cavity thus results in stronger coupling, but to keep the cavity decay rate the same a shorter cavity requires a higher finesse.

If the ion and cavity are weakly coupled the emission of photons by the ion is an irreversible process as the photon is lost from the cavity before reabsorption can occur. This regime can be used if extracting photons from the cavity for measurement or communication between quantum devices is desired.

In the strong coupling regime the ion-photon interaction occurs on timescales much faster than the loss rates present in the system. Such a system is of large interest since the exchange of photons between the ion and the cavity field can be employed to entangle the quantum state of the ion with those of the light field deterministically. Not only is the concept of entanglement one of the most striking results of quantum theory [48, 49], it also opens up many possibilities in the field of quantum information processing [50, 51, 52]. Several schemes have been proposed to utilize a strongly coupled ion-cavity system for quantum computation [53, 54, 55]. The system forms the physical basis for realizing a deterministic ion-photon interface, which would allow the combination of localised quantum processing (trapped ions) and photonic transmission of quantum states, providing the building block for a quantum network [56, 57].

## 6.3 The Experimental Cavity surrounding the 'Alumina' Trap

### 6.3.1 Experimental Setup

The cavity mirrors consist of a cylindrically shaped fused silica substrate of radius 1.5 mm and length 10 mm. One end surface of each substrate is concave, with a radius of curvature of 2.5 cm. To facilitate emission from the cavity to a detection setup predominantly in one direction we use mirrors of different reflectivity. At a wavelength of 866 nm the coatings are specified as 2 ppm and 100 ppm, respectively. The cavity mirrors reside inside two mounts where they are fixed in place using a screw pressing against them from the side. The metal cones are glued to the surface of two shear piezos (figure 6.8, also see chapter 3.4.2). The trap and mirror holders were already assembled during installation of the mirrors. As a result

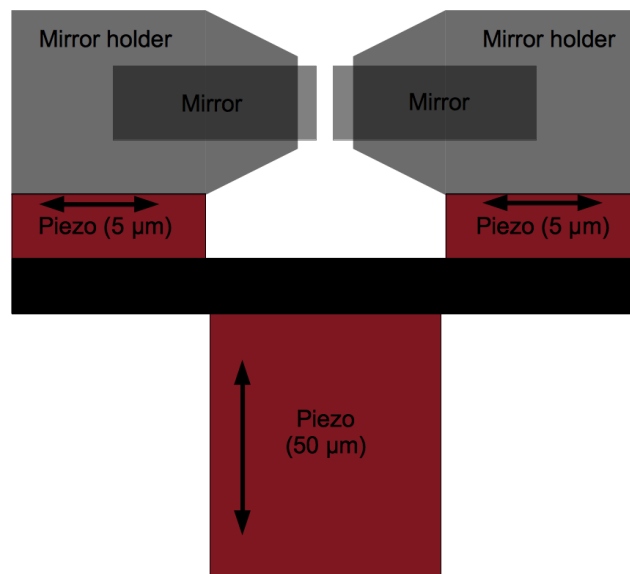


Figure 6.8: The experimental cavity is mounted on a piezo with  $50\ \mu\text{m}$  range so it can be moved in the vertical relative to the trap. The individual mirrors are mounted on shear piezos with  $5\ \mu\text{m}$  range to change the cavity length via electronic signals.

additional care was necessary during the installation to prevent damage to the electrodes due to the proximity of the mirrors. The mirrors were pushed into the cones from behind by hand leaving a relatively large gap to the electrodes. A micrometer stage was used to push the mirrors closer to the trap electrodes in a controlled manner. The movement of the mirrors with respect to the cavity was observed on a video image obtained via a microscope with the objective mounted facing along the trap axis. During the first installation the mirrors were placed 3.7 mm apart. The trap design will ultimately allow a mirror spacing of 0.5 mm. However, to achieve this the mirror substrates will have to be modified to have a tapered front end in order to fit between the electrodes. The current mirrors are not tapered, and some additional space was left to allow for vertical movement of the cavity without touching the electrodes to make sure this would not limit me when trying to move the cavity mode between the electrodes. Crude vertical movement of the cavity is possible by loosening the dowel pins holding the stack in place and sliding it up or down within the trap base structure (Figure 6.9). By drilling a hole through the breadboard the trap structure was mounted on during testing, it was possible to fit a narrow pin through it, which was attached to a micrometer stage below the breadboard. This way the cavity base structure was resting on the tip of the pin, and the height adjusted with micrometer screw while observing the cavity transmission. After the crude alignment was satisfactory, the dowel pins were tightened. The vertical piezo then allows fine adjustment within a range of  $50\ \mu\text{m}$ .

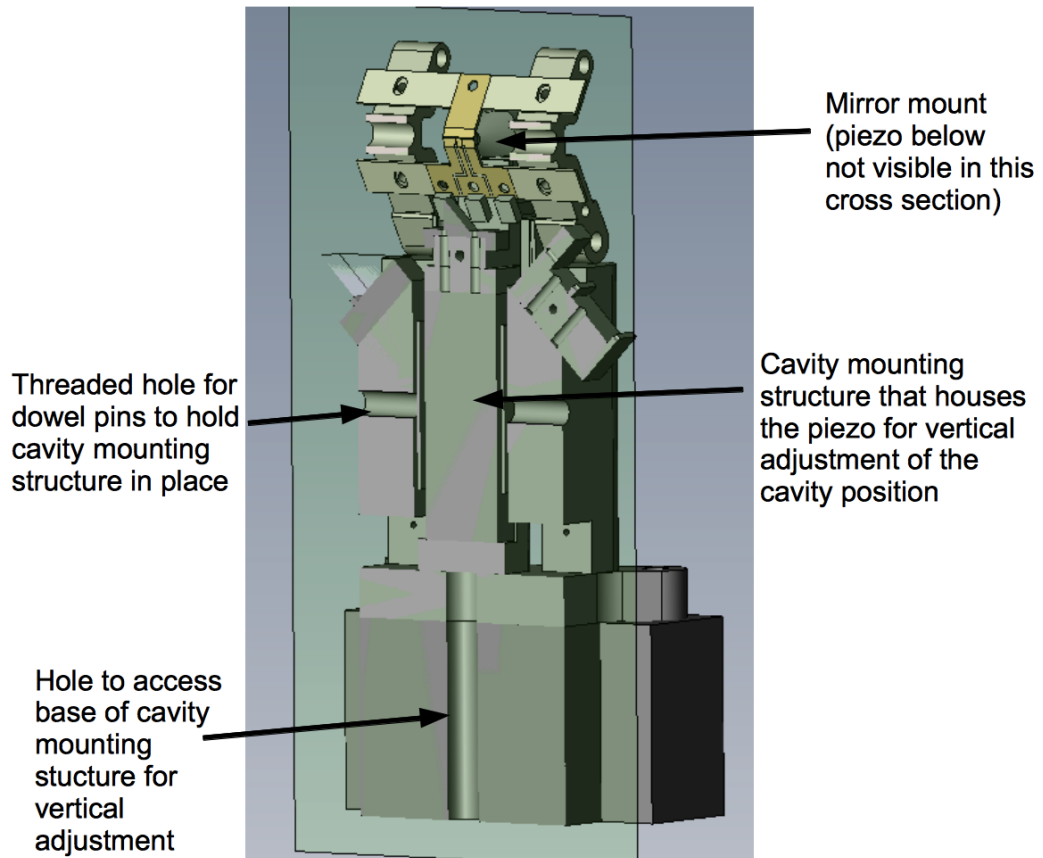


Figure 6.9: Cross section through the 'alumina' trap structure showing the cavity mounting structure including the vertical piezo in place inside the trap base structure.

### 6.3.2 Cavity Characterisation

Referring back to section 6.2.2, we calculate the Rayleigh length and subsequently the waist size of the cavity [58]

$$x_R = z\sqrt{R/x - 1}, \quad (6.29)$$

$$w_0 = \sqrt{\frac{\lambda x_R}{\pi}}. \quad (6.30)$$

For a cavity using mirrors of our specifications and of length 3.7 mm  $x_R = 6.54$  mm, and  $w_0 = 44.72$   $\mu\text{m}$ .

With the absorption losses of the mirrors specified as 2 ppm the total losses of the cavity amount to 106 ppm. The finesse of the cavity is

$$\mathcal{F} = \frac{2\pi}{\delta_0 + \delta_1 + \delta_2}, \quad (6.31)$$

where  $\delta_0$ ,  $\delta_1$ , and  $\delta_2$  are the internal losses, and losses at mirror 1 and 2 respectively. The theoretical value for our cavity is  $\mathcal{F} = 59\,275$ . The free spectral range of the cavity equates to 40.5 GHz, and thus the theoretical linewidth,

$$\Delta\nu = \text{FSR}/\mathcal{F}, \quad (6.32)$$

of the cavity is 683 kHz.

One of the most accurate methods to determine the linewidth and finesse of a cavity experimentally is by using sidebands as a reference. Phase modulating the light results in

$$E_0 e^{i\omega t} \xrightarrow{\text{Modulation}} E_0 e^{i\omega t + i\beta \sin(\Omega_{\text{mod}} t)}, \quad (6.33)$$

where  $E_0$  is the amplitude of the light wave,  $\omega$  its frequency and  $\Omega_{\text{mod}}$  the modulation frequency.  $\beta$  is the modulation depth and if we assume it to be small we can use the first term of the Taylor expansion of the exponential only:

$$E_0 e^{i\omega t} (1 + i\beta \sin(\Omega_{\text{mod}} t)). \quad (6.34)$$

Using trig identities this equals

$$E_0 e^{i\omega t} \left( 1 + \frac{\beta}{2} (e^{i\beta\Omega_{\text{mod}} t} - e^{-i\beta\Omega_{\text{mod}} t}) \right) = E_0 \left( e^{i\omega t} + \frac{\beta}{2} e^{i(\omega + \Omega_{\text{mod}})t} - \frac{\beta}{2} e^{i(\omega - \Omega_{\text{mod}})t} \right), \quad (6.35)$$

clearly showing a central carrier frequency equal to the original light frequency as well as two additional frequencies separated from the carrier by the modulation frequency. These are the sidebands.

If the incoming light is modulated at 15 MHz using an EOM the sidebands are separated 15 MHz from the carrier. This provides us with an accurate reference scale in frequency space for the cavity transmission allowing us to measure the linewidth of the carrier transmission peak. A typical plot of such a measurement is shown in figure 6.10.

Unfortunately the 866 nm ECDL used for testing the cavity has a linewidth approximately 3 MHz, which is larger than the cavity linewidth. So instead of using 866 nm light 894 nm light was used. This laser provides a stable light source with a linewidth of less than the cavity linewidth, thus eliminating any measurement limitations caused by the laser source.

The mirrors have a narrow band coating. Thus for 894 nm light the mirror reflectivities are lower than for 866 nm. According to the data sheet the mirror transmissions at 894 nm are 200 ppm, and 35 ppm, while the absorption losses are 3 ppm per mirror. This gives a theoretical

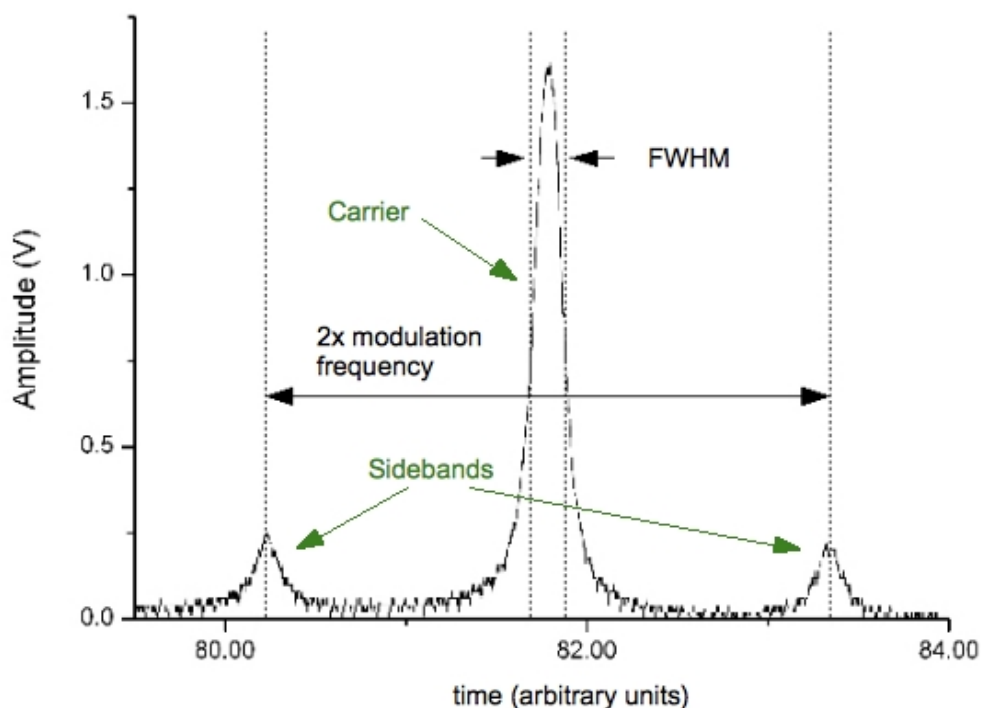


Figure 6.10: Cavity transmission as a function of cavity length as recorded with a photo diode. The large peak is the carrier frequency, the two smaller peaks are the sidebands modulated onto the laser.

linewidth value of 1.55 MHz. By measuring the linewidth of the cavity for 894 nm light, we could establish a value for the actual losses. The cavity linewidth for 894 nm light was measured as 1.73 MHz which equates to  $\sim 30$  ppm losses in the system in addition to those specified. The most likely reason for the deviation from the specifications is contamination of the mirror surfaces which can be assumed to be wavelength independent. Calculating the finesse at 866 nm from these values,  $\mathcal{F} = 46\,200$ , and a linewidth of 876.6 kHz is obtained.

### 6.3.3 Stabilising the Cavity

To avoid any interference with the ion, the locking scheme doesn't use the 866 nm light resonant with the  $D_{3/2}$  to  $P_{1/2}$  transition but 894 nm. This is close enough to 866 nm to provide reasonable performance from the mirrors. The light comes from the Cs stabilised ECDL which has the added benefit of a narrow line and excellent stability. The 894 nm laser is already current modulated to provide sidebands for the Pound-Drever-Hall (PDH) lock [59] used within the scanning cavity system. The same sidebands can be seen by scanning the cavity length while recording the light reflected from the cavity with a photo diode.

As a result of the large base of the structure passive stability of the cavity is fairly good, and it stays on resonance for timescales of a few ms. For the active stabilisation we can supply control signals to the mirror piezos. It is common practise to set the upper limit of such stabilisation to 1/10 of the linewidth, which is approximately 1 pm in this case. High frequency noise can be suppressed using passive filters of appropriate cut off frequency, while in the low frequency range active stabilisation will be used to compensate any drifts. The proposed scheme for active cavity stabilisation and locking is depicted in figure 6.11.

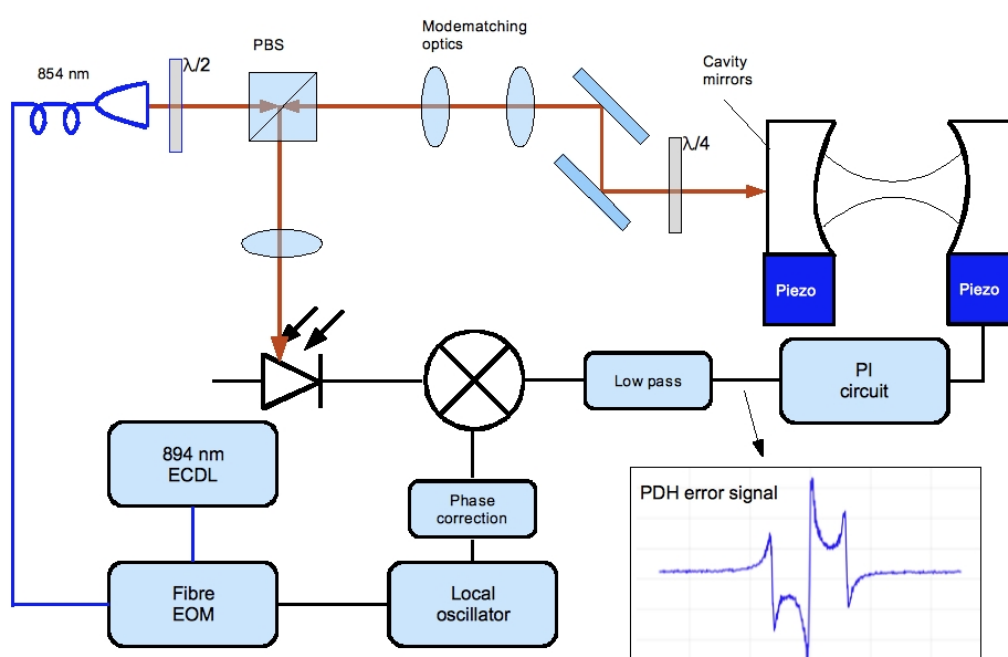


Figure 6.11: A schematic of the proposed setup for locking the experimental cavity to a sideband of the cesium reference laser.

### Pound - Drever - Hall Technique

This technique uses sidebands (section 6.3.2) to generate an error signal. If the laser is incident on an optical cavity with a resonance equal to that of the laser, the sideband components of the spectrum are reflected provided the rf frequency is higher than the linewidth of the cavity resonance. The general transfer function of the light reflected out of the Fabry - Pérot cavity is

$$T_{\text{ref}}(\omega) = \frac{E_{\text{ref}}}{E_{\text{in}}} = \frac{-r_1 + (r_1^2 + t_1^2) r_2 e^{i2\omega L_{\text{Cav}}/c}}{1 - r_1 r_2 e^{i2\omega L_{\text{Cav}}/c}}, \quad (6.36)$$

Where  $E_{\text{ref}}$  and  $E_{\text{in}}$  are the reflected and incoming light wave's electric field respectively,  $r_1$  and  $r_2$  the reflection coefficients of the the two mirrors, and  $t_1$  the transmission coefficient of mirror 1. For light modulated as discussed previously this results in

$$E_{\text{ref}} = E_0 \left[ T_{\text{ref}}(\omega) e^{i\omega t} + T_{\text{ref}}(\omega + \Omega_{\text{mod}}) \frac{\beta}{2} e^{i(\omega + \Omega_{\text{mod}})t} - T_{\text{ref}}(\omega - \Omega_{\text{mod}}) \frac{\beta}{2} e^{i(\omega - \Omega_{\text{mod}})t} \right]. \quad (6.37)$$

The power reflected from the cavity is proportional to the square of the electric field and can be recorded with a photo diode. This signal contains an antisymmetric function of  $(\omega - \omega_{\text{resonance}})$  [60]

$$\chi(\omega) = T_{\text{ref}}(\omega) T_{\text{ref}}^*(\omega + \Omega_{\text{mod}}) - T_{\text{ref}}^*(\omega) T_{\text{ref}}(\omega - \Omega_{\text{mod}}). \quad (6.38)$$

$\chi$  can be extracted electronically mixing the photo diode signal  $V(\omega)$  with the phase-shifted rf oscillator signal (local oscillator) and subsequently low-pass filtering it to remove sinusoidally oscillating terms:

$$V(\omega) \propto \text{Re}[\chi(\omega)] \cos \varphi + \text{Im}[\chi(\omega)] \sin \varphi, \quad (6.39)$$

where  $\varphi$  relates to the phase shift.

This signal gives a measure of how far the laser carrier is off resonance with the cavity (PDH signal, figure 6.11) to feed back to the cavity. Close to resonance, the phase has a linear relationship with the laser detuning.

The Pound-Drever-Hall error signal is sent to a proportional-integral (PI) feedback circuit, which in turn is connected to one channel of the high voltage supply connected to the cavity piezos. Proportional feedback amplifies the error signal before feeding it back to the piezo. It has high bandwidth, but is insufficient for accurate locking on its own. The nature of the PDH signal is such that the feedback signal is small when the cavity is close to resonance. Over time this typically results in a lock with an offset. Integral feedback is used to correct for this. It has low bandwidth and gain that increases as  $1/f$  at low frequencies.

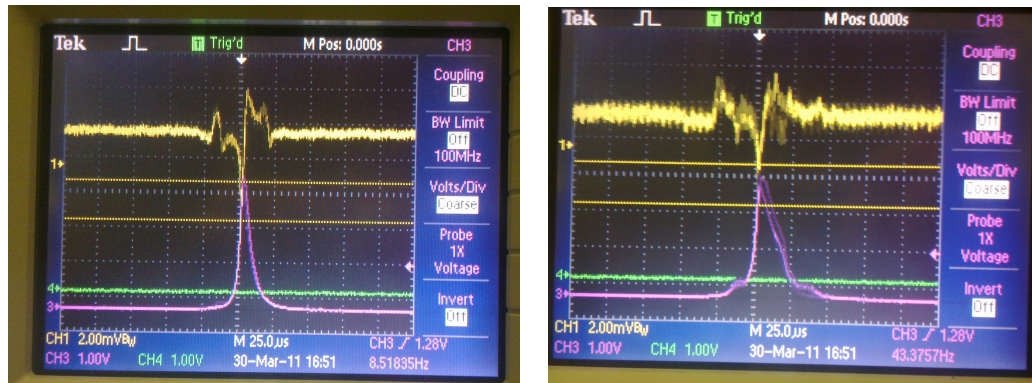
### Scanning the Cavity Length using EOM Sidebands

To stabilise the cavity length it would be sufficient to lock its length to the carrier frequency of the stabilised laser, but our experiments require us to tune the cavity length to match the atomic resonance in addition to achieving good stability. As we have control over the frequency of the sidebands by changing the modulation frequency these make a much better candidate for this purpose. By adding a second modulation, the initial sidebands have sidebands of their own to generate a PDH error signal, and thus we can then stabilise the cavity length to the sidebands resulting from the first modulation. It is not a good idea to use sidebands

generated by the current modulation of the laser, because current modulation also creates amplitude modulation of the laser output, which in turn would generate an offset in the PDH error signal. To work around this we use a fibre EOM for both modulations. The amplitude modulation associated with the electro-optic process is much smaller and the resulting offset can therefore be neglected. In addition the tuning range of the EOM with respect to the carrier frequency is much larger than what is achievable with current modulation. This is essential for overlapping a longitudinal/transverse mode of the atomic reference with the  $TEM_{00}$  mode of the cavity Raman resonance. However, due to the large FSR (40.5 GHz) of the cavity a further trick needs to be used to enable us to scan the cavity length over an entire FSR. The use of different transverse modes of the cavity (section 6.2.2) extend the range of possible sidebands as the resonance frequencies for different transverse modes differ (equation 6.13) we can select a resonant transverse mode for the 894 nm laser for locking that is within 1 GHz (tuning range of the synthesiser providing the modulation signal) of the 866 nm resonance of the  $D_{3/2} \rightarrow P_{1/2}$  transition. Using a higher order transverse mode for the lock also has the advantage that the spatial intensity distribution can be selected such as to coincide as little as possible with a  $TEM_{00}$  mode for the 866 nm light and thus making the separation of the two signals behind the cavity easier.

### Preliminary Results

A first step towards achieving a cavity lock is the observation of a PDH error signal. The modulated 894 nm laser was coupled into the cavity and its reflection observed with a dc coupled avalanche photo diode while the cavity length was scanned by applying a function generator signal to one of the cavity piezos via the high voltage supply. The cavity transmission was observed with a photo diode behind the cavity. The output of the PI circuit was connected to the other high voltage supply of the other piezo mirror. With the P gain of the circuit set correctly engaging P is expected to counteract the cavity length scan and the transmission widens. This effect is shown in figure ???. When this effect can be observed the P gain setting is within the right range and should only require a small amount of optimisation later. However, switching off the cavity length scan and trying to stabilise the cavity with P only was unsuccessful initially. When examining this in more detail the it came to light that for this cavity a scan across one complete FSR takes about 50 V to be supplied to the piezo. Coupled with the large cavity finesse this means that the width of the transmission peaks will be equivalent to a few mV only. The output of the high voltage supply connected to the piezo has electronic noise of the same order of magnitude. Hence achieving a stable lock was



(a) Transmission (purple) and error (yellow) signal with no feedback

(b) Transmission and error signal with P feedback

Figure 6.12: The effect of proportional feedback on the transmission peak of the optical cavity

impossible with the initial setup. To overcome this modified the setup as shown in figure 6.13.

We use two PI circuits, the first for fast feedback to compensate for high frequency low amplitude drift caused by electronic noise, with its output directly connected to one of the mirror piezo via a small resistor. The second PI circuit takes care of slower drift ( $<100$  MHz). The PI circuit output is supplied to the high voltage supply, which is connected to the second mirror piezo via a low pass filter that stops the high frequent noise from the high voltage supply reaching the piezo. An additional capacitor connected to ground very close to the vacuum feedthrough was included to eliminate any high frequency noise picked up along the length of the cable. With this revised scheme in place some locking effect could be observed (figure 6.14). When trying to optimise this however, no improvement to a permanent lock could be achieved. At this point there was still some offset drift present in the error signal. After eliminating polarisation drift as the source of this, we moved on to establish whether there was a certain frequency of noise present in the signal. We recorded the fast Fourier transforms (FFT) of the error signal, the cavity transmission signal, as well as the PI circuit outputs using a spectrum analyser. The results of this were not conclusive at the time when I stopped working on this to start writing this thesis, so further investigation is necessary.

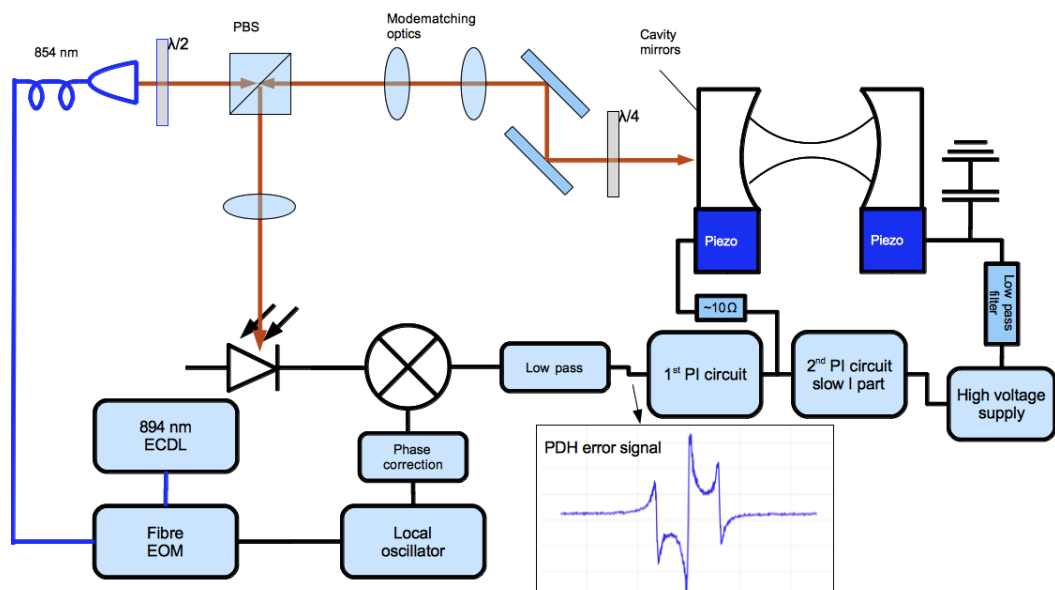


Figure 6.13: A schematic of the revised cavity locking scheme. This scheme uses two PI circuits, the first for fast feedback to compensate for high frequency low amplitude drift caused by electronic noise. The PI circuit output is connected directly to one of the mirror piezo via a small resistor. The second PI circuit takes care of slower drift ( $<100$  MHz). The PI circuit output is supplied to the high voltage supply, which is connected to the second mirror piezo via a low pass filter.

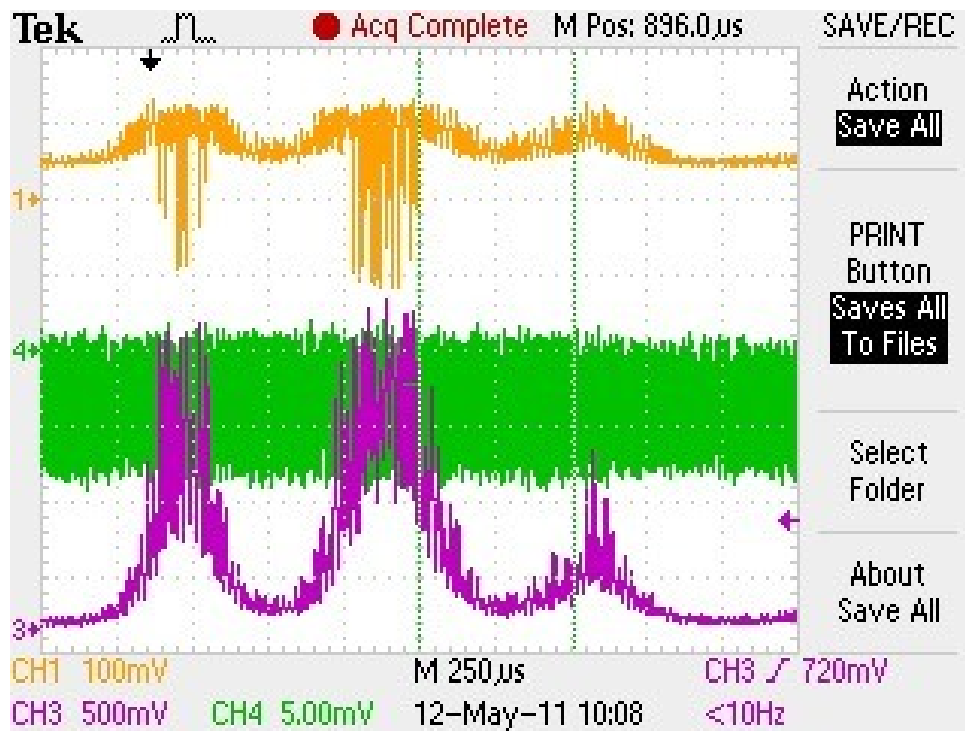


Figure 6.14: The first signs of the cavity length lock working. The pink trace is the cavity transmission as observed with the photodiode behind the cavity, the yellow trace is the PDH signal, the green channel was not connected, and just shows noise.

## 6.4 Cavity Parameters of the 'Alumina' Cavity

In the current setup (cavity length 3.7 mm, radius of curvature 2.5 cm)  $g_0$  evaluates to  $2\pi \times 1.2$  MHz and  $\kappa$  to 438.3 kHz. As we can see in figure 6.15 this value exceeds  $\kappa$  but not  $\Gamma$  so we are in the weak coupling regime. A reduction of the cavity length to the proposed 0.5 mm results in an increase of the coupling strength to  $2\pi \times 5.2$  MHz, which clearly exceeds the decay rate of the  $P_{1/2} \rightarrow D_{3/2}$  transition  $\Gamma_{\text{red}}$ . However,  $\kappa$  depends on the cavity length as  $1/L$  while  $g_0$  is proportional to  $L^{-3/4}$  so for small  $L$   $2\kappa$  exceeds  $g_0$ . As a result we can't reach the strong coupling regime with the current mirror combination of one 100 ppm and one 2 ppm mirror. However, for experiments requiring strong coupling we don't require the transmission of the produced photons via one of the mirrors, and hence we can replace the 100 ppm mirror for another 2 ppm one. Even assuming we still have additional losses of the same magnitude in the cavity as we presently have this would result in a finesse of  $\mathcal{F} = 153248$ , in which case strong coupling can be readily achieved within the setup. The total decay rate from the upper

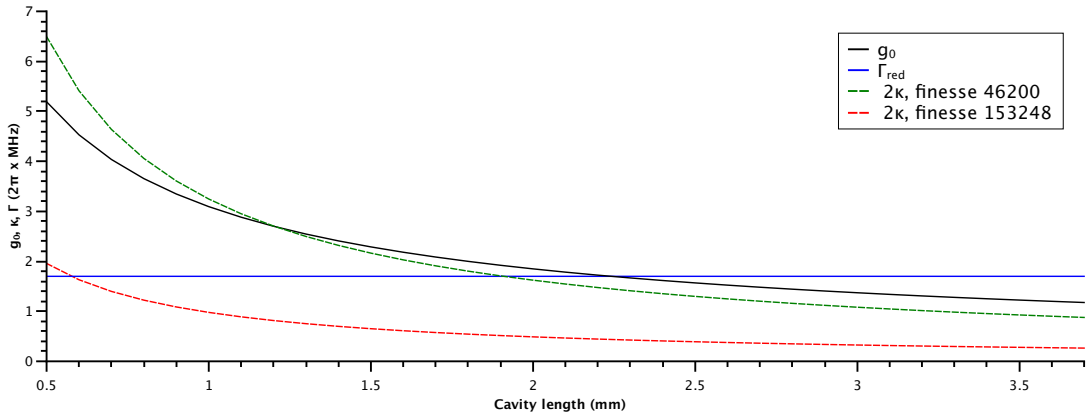


Figure 6.15: The relationship of the ion cavity coupling strength  $g_0$ , the cavity decay  $2\kappa$  and the atomic decay rate  $\Gamma$  with decreasing cavity length for the experimental cavity surrounding the razor trap. The cavity decay is evaluated for two different finesse cavities, one of which is our current set of mirrors. The higher finesse cavity assumes the use of two identical 2 ppm mirrors and similar additional losses due to contamination on the mirror surfaces as currently present. Only the atomic decay rate of the  $P_{1/2} \rightarrow D_{3/2}$  transition is included. The  $P_{1/2} \rightarrow S_{1/2}$  transition even though much more likely to occur is driven by the cooling laser, and so the ion will immediately be re-excited to the  $P_{1/2}$  state if it decayed to the  $S_{1/2}$  state.

state is the sum of the decay rates to the  $S_{1/2}$  or the  $D_{3/2}$  state. For the purpose of evaluating whether we are able to achieve strong coupling with our ion trap cavity system only the  $P_{1/2} \rightarrow D_{3/2}$  decay is relevant. For the case of single photon generation experiment this is based on the presence of the cooling laser driving the  $S_{1/2} \rightarrow P_{1/2}$  transition, so if the ion decays to the  $S_{1/2}$  state it will immediately be repumped to the  $P_{1/2}$  state. For experiments where the cooling laser is not permanently present the arguments still holds as we can always

detect the event of the ion decaying to the ground state and eliminate by post selection. Thus, we can neglect the transition's contribution to the total decay rate here.

## 6.5 Locating the Ions within the Cavity Mode

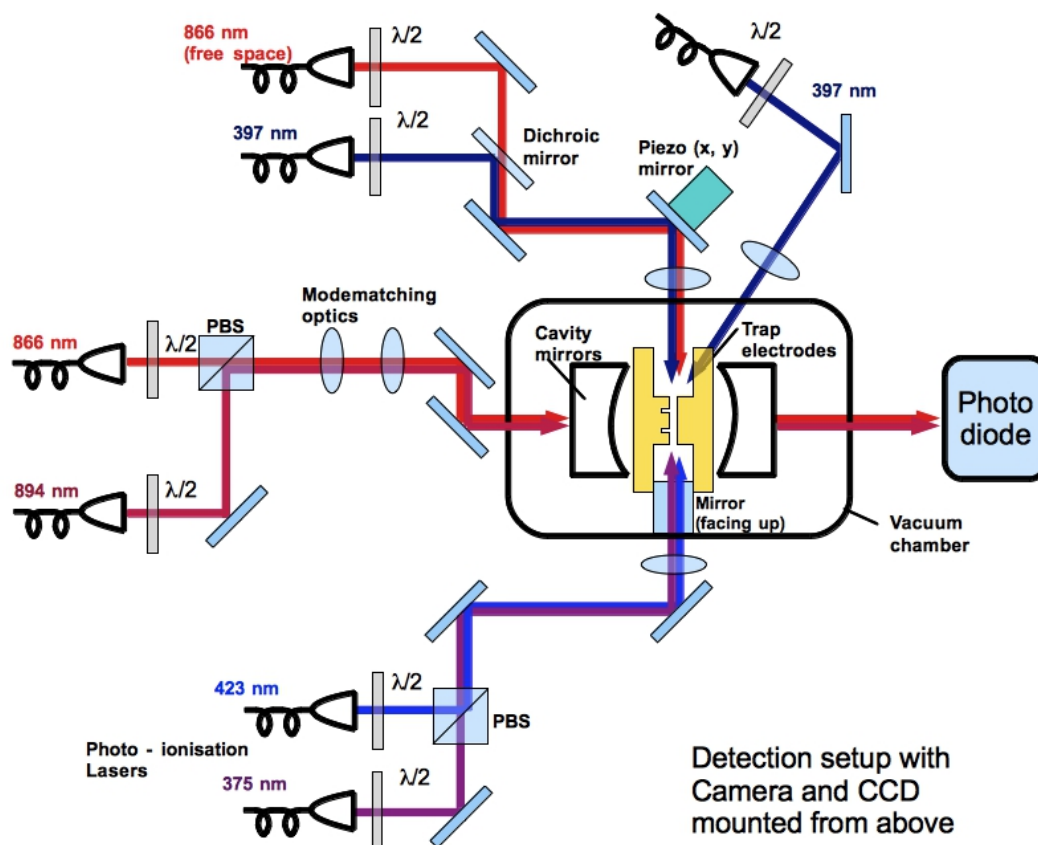


Figure 6.16: A schematic of the experimental setup during the first experiments to place the ions into the cavity mode.

Figure 6.16 shows the setup used for the initial experiments with the cavity. One cooling laser and the free space repumper are overlapped via a dichroic mirror and enter the chamber along the axis of the trap. Just as in the previous setup the final mirror is mounted on a piezo allowing the central region of the trap to be scanned systematically. These two lasers were used to detect the first ion signal in the 'alumina' trap. A second cooling laser enters under an angle from the back of the trap. The combined photo ionisation lasers enter the chamber under an angle in the  $y-z$  plane. Both lasers are reflected by a mirror attached to the side of the trap base structure, its reflective surface facing upwards. This way the ionisation lasers can traverse the trap from diagonally from below and more crucially intercept the stream of

atoms from the oven perpendicularly. This eliminates the velocity selectivity of the ionisation process.

Finally the 894 nm laser for the cavity lock is overlapped with a second repumper beam via a polarising beam splitter. These beams pass two additional lenses to match the beam to the cavity mode, and then enter the cavity through the back of one of the cavity mirrors. A photodiode monitoring the cavity output mirror is used to observe the cavity transmission.

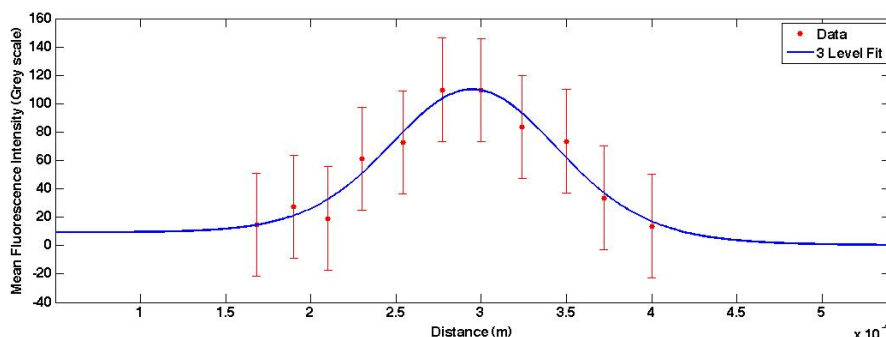
To observe the ion position within the cavity mode an ion string was trapped using the free-space laser beams. The power in the free-space repumper was then reduced, and eventually the beam was blocked completely, while the cavity was kept on resonance by manually adjusting the voltage to one of the shear piezo beneath the mirror mounts. By observing the ion fluorescence with the camera it was possible to see whether the cavity mode coincided with the position of the ions. The initial voltage settings of the axial confinement electrodes was symmetric. With these initial settings there was a small overlap between the ions and the cavity mode already. Several ions at one end of an ion string were fluorescing more brightly as the cavity was scanned through resonance. A small adjustment of the axial confinement voltages moved the ion along the axis into the centre of the mode volume. We then proceeded to move the cavity vertically with respect to the trap electrodes with the piezo underneath the cavity mounting structure ( $\pm 25 \mu\text{m}$ ). No change in fluorescence intensity was observed, indicating good vertical alignment.

### 6.5.1 Preliminary Results

Stills from a movie recorded as the cavity length was tuned are shown in figures 6.17 and 6.18. The power incident on the cavity incoupling mirror was  $150 \mu\text{W}$ . When the cavity starts to approach resonance only the ions in the centre of the mode are visible. As the intensity in the cavity builds up more ions of the string become visible. Eventually the light becomes so intense that a drop in fluorescence becomes visible with increasing repumper intensity at the centre of the cavity mode. For a quantitative analysis of the image data, circular regions of interest (ROI) of equal area at each ion position using imageJ were created. By extracting the mean Grey scale value for these ROIs a measure of the fluorescence intensity at each ion position was obtained. Plots of the fluorescence intensity as a function of ion position are shown below the corresponding images: Figures 6.17b, 6.17d, and 6.18b. The resonant cavity mode during these recordings was the  $\text{TEM}_{00}$  mode as confirmed by observing the cavity transmission with a camera. The detunings of the cooling laser and the laser incident on the cavity were  $2\pi \times 55 \text{ MHz}$  and  $0 \text{ MHz}$ , respectively.



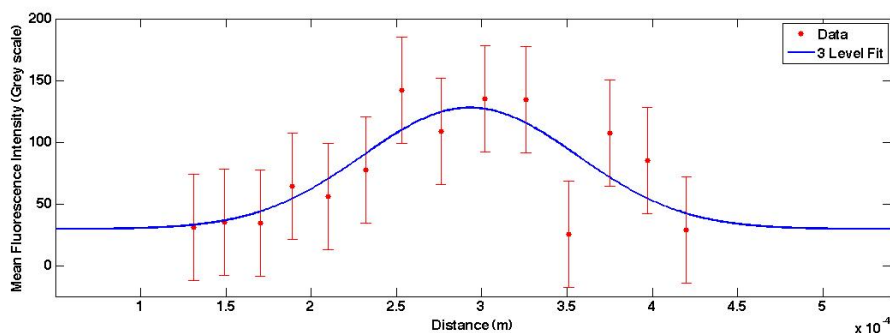
(a) The central ions of the ion string are visible as the cavity approaches resonance



(b) The intensity of the ion fluorescence as a function of ion position



(c) Cooling fluorescence becomes more efficient as the cavity position increases



(d) The intensity of the ion fluorescence as a function of ion position

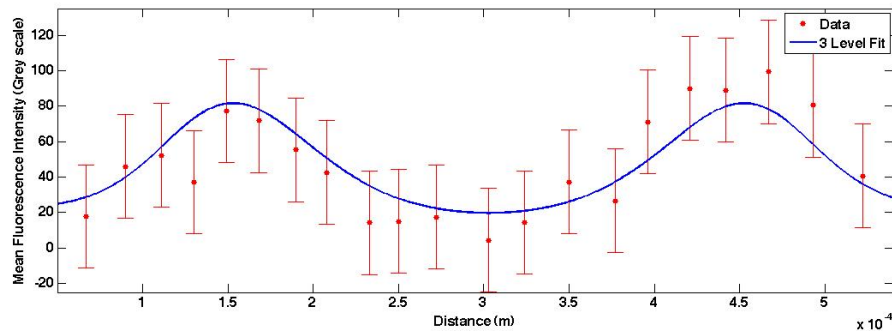
Figure 6.17: The cooling fluorescence of an ion string as the cavity is moved into resonance for the 866 nm laser incident on one of the cavity mirrors. A fit of the three-level model described in section 6.2.3 to the intensity data extracted from the images reveals a simple Gaussian shape, which corresponds to the intensity distribution in the cavity.

Matlab was used to fit the theoretical scattering rate as predicted by the three-level model described in section 6.2.1 to the data (equation 6.6). For the low intensity the fit looks similar to the Gaussian intensity distribution of the intensity across the cavity. In contrast to figure 6.17, figure 6.18 shows significantly reduced fluorescence intensity at the centre of the trap due to the ac Stark shift as discussed previously.

This effect is very useful to map structure of the intensity distribution and improve the overlap of the trap centre and the cavity mode further improving on previous adjustments done by observed count rate alone. For the horizontal adjustment the trap centre has to be moved along the axis by adjusting the dc voltage applied to the axial confinement electrodes. Using a single ion and mapping the fluorescence intensity at different position/dc voltages allows to optimise the the horizontal positioning. In the vertical the cavity is moved with respect to the



(a) The intensity at the centre of the cavity mode is so high that the fluorescence drops as predicted by the Bloch equations for a  $\Lambda$  system. The fluorescence drops at the centre while the ions still appear bright at the edge of the mode where the intensity is lower.



(b) The intensity of the ion fluorescence as a function of ion position.

Figure 6.18: The cooling fluorescence of an ion string as the cavity is moved into resonance for the 866 nm laser incident on one of the cavity mirrors. A dip in the fluorescence is visible when the intensity at the centre of the cavity increases.

trap. This adjustment is best done with an ion string. Compared to the range of movement available with the dc voltages the range of the piezo is small. This makes it difficult to get a precise mapping of the mode in the vertical with a single ion unless the intensity in the cavity is very small. In practise this proved impossible as for any signal large enough to be detected with the camera there was very little variation in the fluorescence intensity across the piezo's scan range. Using an ion string the length of visibility for the string gives an additional measure of the vertical position of the mode relative to the trap centre.

### Calibrating Ion Movement

In order to get a first measure of the precision we have available for locating the ion within the cavity mode, the following data was obtained. A string of seven ions was loaded into the trap. The initial axial confinement voltages were 1.4 V on both electrodes on one side (EC1 and EC4 in figure 6.19) and 0.3 V on the other (EC3 and EC6 in figure 6.19). This saw the string approximately central within the cavity mode. By changing the voltage on one of the axial electrodes (EC1) first to 2.4 V and then to 0.4 V the ions were observed to move. The images obtained from this are shown in figure 6.20. By measuring the ion position (in pixels) of the third ion from the left of the string, we know that the ion moves approximately 37 pixels for every 1 V applied to one axial electrode. For our imaging system (see chapter 3.3) this

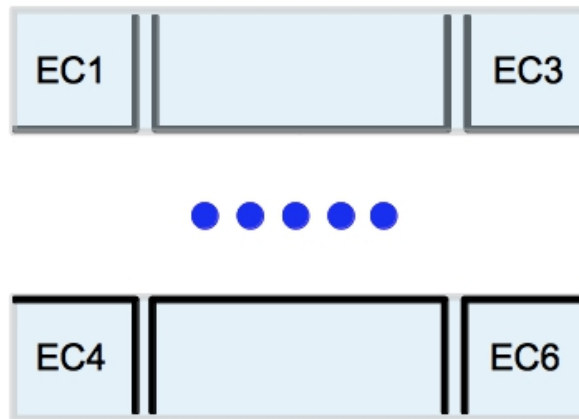


Figure 6.19: The position of the dc electrodes for axial confinement in the 'alumina' trap

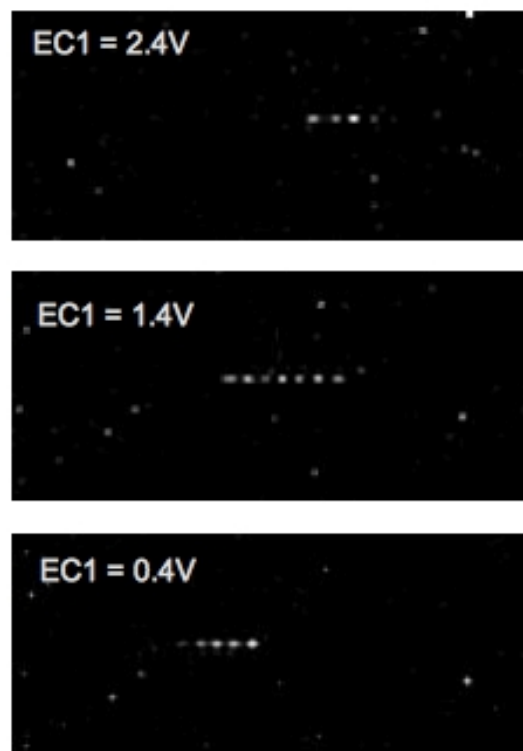


Figure 6.20: With decreasing dc voltage on one of the four axial electrodes the ions move across the cavity mode and only part of the string is visible at the extremes. EC1 is the electrode at the top left hand corner in the images. EC4 (bottom left) was held at 1.4 V and EC3 and EC6 at 0.3 V throughout.

equates to a distance of  $370 \mu\text{m}$ . The positioning of an ion along the axis can therefore be changed on a scale of approximately  $0.37 \mu\text{m}/\text{mV}$ .

## 6.6 Conclusions

The optical cavity used with the 'alumina' trap was introduced and characterised in this chapter. Measurements of cavity parameters show that strong coupling can be achieved in this setup if the mirror substrate are modified to fit between the mirrors.

A scheme for locking the length of the cavity was proposed and discussed in some detail.

The alignment of the trap centre and the cavity mode was established for the 'alumina' trap. The fact that the ion string was initially partly overlapped with the cavity mode, which has a waist of only 43 microns, pays tribute to the great care taken during design and assembly of the trap and cavity. The mirror substrate proximity does not affect the trapping as expected. The preliminary data extracted from the camera pictures was successfully evaluated with respect to the three-level model for the ion fluorescence. The large intensity in the cavity allowed to observe the relationship between cooling fluorescence as proposed by the Bloch equations for a  $\Lambda$  system. The spatial distribution of the intensity combined with a string of ions serves as a useful tool to determine the centre of the cavity mode and to improve the position of the the two with respect to one another.

## Chapter 7

# Conclusions and Outlook

### 7.1 Conclusions

The experimental setup at Sussex follows on from work done by Matthias Keller *et al.* in the field of cavity QED with trapped ions at the Max Planck Institute in Garching. While the first cavity QED experiment investigating strong coupling used neutral atoms [61], the use of a trapped ion was strongly motivated by the quantum computation model presented by Cirac *et al.* [56] in 1997. Experimental work to implement these ideas started in Garching as well as in Rainer Blatt's group in Innsbruck, and in 1998 a first working ion trap that was built with cavity QED in mind was reported [62]. In 2002 Guthörlein *et al.* [29] presented an ion trap cavity system where the ion was used to map the cavity mode. These results gave an indication of how precisely an ion could be located within the cavity mode, which is an important consideration for cavity QED, and one of the largest problems in the use of neutral atoms. In 2003, using this setup the Garching group then demonstrated the deterministic coupling of ions to the cavity mode [28] while similar results were achieved by the Blatt group [63]. A great milestone was the implementation of the single photon source with precisely controlled waveforms and timing in 2004 [64] as this was the first experimental demonstration of a source of single photons that was stable over a long period of time and thus practical for the implementation of more elaborate experimental schemes. Over the following years much work was done to characterise the experimental setups more thoroughly [65] and study the processes within the ion cavity system [66].

More recent results show that experimental setups are edging ever closer to strongly coupling a single ion to a cavity. The 'alumina' trap reported on in this thesis certainly looks a promising candidate for achieving strong coupling, as do the fibre cavity trap developed in the Sussex lab, which uses the electrodes themselves to shield the ion from the mirror substrates (fibres).

Steiner *et al.* [67] very recently reported coupling of an ion to such a cavity achieving an unprecedented coupling strength owing to the small mode volume. While a short cavity is more easily achieved with a fibre cavity, their inherent problem is the quality of the mirrors and hence the cavity finesse makes it difficult to achieve cavity decay times that allow it to reach the strong coupling regime.

Regardless of the approach taken designing and building a system for strongly coupled cavity QED experiments provides unique challenges. The 'sandwich' trap had been developed as a successor to those used during experiments in Garching with the goal that the small cavity size required for strong coupling and thus the proximity of the mirror substrate to the ions would no longer impair the trapping ability of the ion trap. The resulting design introduced a set of new issues to overcome. Firstly, the microscopic size of the trap caused the electrode alignment to be a source of complications, so it had to be revisited before we could successfully trap ions. A further concern due to the size of the trap was the quality of the electrodes themselves. Defects intrinsic to the machining processes employed cause relatively larger changes to the structure on small parts than they do on larger parts. To quantify whether this was justified we conducted measurements of the heating rates of an ion in the trap. The heating rates of the 'sandwich' trap turned out to be not a limiting factor to the use of the trap for our experiments. A slight surprise was that during the measurements and the analysis of the data we had to acknowledge that the radiation pressure from the cooling laser that was being switched on and off during the measurement was causing additional line broadening.

The trap design also required shuttling of the ions from a production region that was subject to a large atom flux from the oven to an experimental region where the cavity was to be positioned. The process had been used successfully in larger traps of similar design but the reduction in size meant that it proved far more difficult to control this in the 'sandwich' trap. During such a shuttling process the axial confinement electrodes separating the two regions are switched to 0 V and back to their original value after a short time. The trapped ion doesn't encounter a potential barrier in one direction when one of the axial electrodes is switched to zero, and will carry on moving in this direction until it encounters the next potential barrier. If this barrier is higher than the ions energy, it will reverse direction. In the meantime the electrode that had been switched to 0 V is returned to its original value intercepting the ion's path. The ion is now trapped inside a different region. With the 'sandwich' trap this process could not be implemented successfully. The reason for this is likely to be found in the irregularities in the trap structure due to the difficult process of its assembly. These irregularities then make the influence of individual electrodes stronger relative to others and as a result the

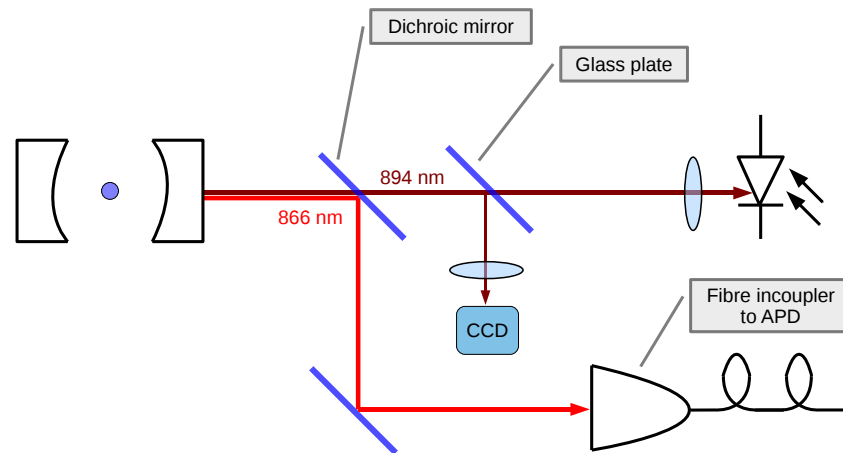


Figure 7.1: Single photon detection setup: The transmitted 894 nm light from the beam used to lock the cavity needs to be extracted from the output. Only the 866 nm photon is directed to the PMT via an optical fibre.

ions gain momentum in directions other than the axial (shuttling) direction enabling them to escape the trap.

The 'alumina' trap was designed as an alternative taking into account the problems encountered with the 'sandwich' trap. The different positioning of the oven rendered a distinction between trapping and experiment region unnecessary. The physical separation of the electrodes into four blades improved the optical access to the trap further, as it is possible to view the ions from above as well as from below due to the integration of mirrors on the side of the trap structure in addition to the side access.

Both trap designs allow mirror spacings that are small enough to reach the strong coupling regime. While some modification is needed to show this experimentally the practicality of overlapping the ions and the cavity mode in the 'alumina' trap setup was tested successfully.

## 7.2 Outlook

This paragraph outlines briefly two possible experiments for the 'alumina' trap setup.

### 7.2.1 Single Photon Source

The next step to progress towards strong cavity QED experiments is to stabilise the cavity length. The proposed scheme for this was discussed briefly in section 6.3.3. One way to test the ion - cavity interaction is by using single photon detection (figure 7.1). Due to the different reflection coefficients of the chosen mirrors any photon leaving the cavity via one of the mirrors has a 98% probability to escape via the 100 ppm mirror, and so we record the cavity emission behind this mirror. The detector used is an avalanche photodiode sensitive enough to detect single photons. Since we only want to detect the light from the cavity - assisted Raman transition of the ion (866 nm) we need to split the light from the 894 nm light used to lock the cavity length by using a dichroic mirror. A photo diode and a CCD camera are used to observe the 894 nm transmission of the cavity for the purpose of optimising the cavity lock. Referring back to the level scheme shown in figure 6.1, an ion prepared in the ground state is subject to a pump pulse on the  $S_{1/2} \rightarrow P_{1/2}$  transition and detuned from the  $P_{1/2}$  level. The cavity length is tuned to be on resonance with the transition from this virtual level and the  $D_{3/2}$  level. When the ion transitions into the  $D_{3/2}$  state it emits at most one 866 nm photon into the cavity mode. With the current setup we are in the weak coupling regime. Therefore the photon is more likely to escape the cavity than to be re-absorbed, and will escape the cavity with a given probability. If the cooling laser remains switched off after the pump pulse and the 866 nm photon escaped the cavity the ion is temporarily trapped in the  $D_{3/2}$  state, which is metastable with a lifetime of 1 s. On the time scale of our experiments this can be assumed as stable. The ion cannot emit another 866 nm photon until it has returned to the ground state and repeated this process.

### 7.2.2 Two Ion Entanglement

Entanglement is a feature of quantum mechanics that has no classical counterpart. A scheme to entangle two ions via a resonant cavity was proposed by Pellizzari *et al.* [53] in 1995. To successfully implement this scheme the ion needs to have a  $\Lambda$  structure for its electronic states. This is necessary as two different stable atomic states need to be available to be used as qubits. This is the case for  $^{40}\text{Ca}^+$ , if we consider the ground state ( $S_{1/2}$ , state  $|S\rangle$  in figure 7.2), and the metastable state ( $D_{3/2}$ , state  $|D\rangle$  in figure 7.2). Furthermore there is a technical restriction to implementing this scheme. We need to ensure that the photon remains in the cavity long enough to be re-absorbed, i.e. we need to achieve strong coupling. Figure 6.15 shows the relationship between the coupling strength  $g_0$ , the atomic decay rate  $\Gamma$ , and the cavity decay rate  $2\kappa$  as a function of the cavity length. From the graph it can be concluded that to reach

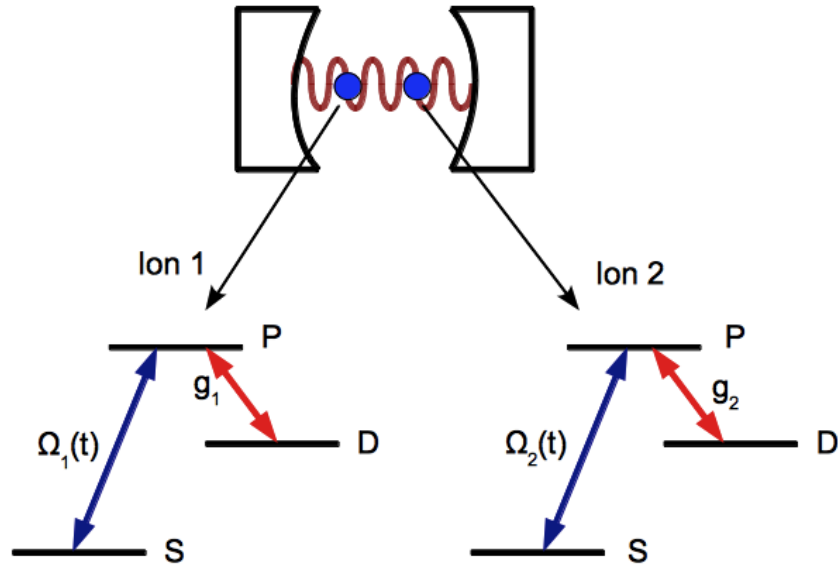


Figure 7.2: Two ions inside an optical cavity

the strong coupling regime we require a shorter cavity such that  $g_0$  exceeds  $\Gamma$ , as well as a higher finesse such that  $g_0$  exceeds  $2\kappa$ . Shortening the cavity requires the use of mirrors with a cone-shaped substrate. Only then will it be possible to move the mirror surfaces closer to the trap centre without making contact with the electrodes. To increase the finesse we will have to replace the mirror with the 100 ppm coating with one of a higher reflectivity. In the graph this step is represented by moving from the green curve to the red curve.

Assuming both ions are coupled to the same mode of the cavity, the system described in figure 7.2 has the Hamiltonian:

$$\begin{aligned}
 H = & \hbar\Omega_1 (|S_1\rangle \langle P_1| + |P_1\rangle \langle S_1|) + \hbar g_1 (|D_1\rangle \langle P_1| a^\dagger + |P_1\rangle \langle D_1| a) \\
 & + \hbar\Omega_2 (|S_2\rangle \langle P_2| + |P_2\rangle \langle S_2|) + \hbar g_2 (|D_2\rangle \langle P_2| a^\dagger + |P_2\rangle \langle D_2| a) . \quad (7.1)
 \end{aligned}$$

The indices refer to ions 1 and 2 respectively, and  $\Omega$  and  $g$  have their usual meanings. The terms involving  $\Omega$  describe the interaction between the ion and the cooling laser, while the terms containing  $g$  describe the interaction between the cavity and the ion. Figure 7.3 describes how the cavity mode can be used to transfer information from one ion to another. To start with ion 1 is in the ground state ( $|S\rangle$ ), while ion 2 is in the excited state ( $|D\rangle$ ). Both ions are coupled to the same mode of the resonator and are subject to the same pump pulse. Ion 1 can absorb a photon from the cooling laser pump pulse and make a Raman transition to state

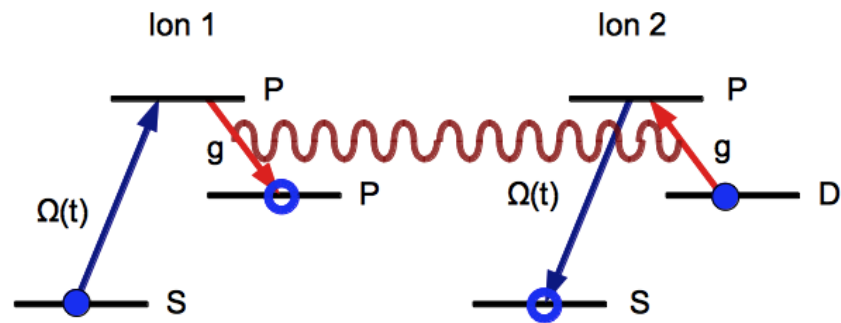


Figure 7.3: A schematic showing the transfer of their respective quantum states from ion 1 to ion 2 and vice versa by means of the cavity excitation

$|D\rangle$  while emitting a photon into the cavity mode. Ion 2 can then absorb this photon, and make a Raman transition to the ground state. By choosing the intensity and the duration of the pump pulse carefully it is possible to control this process in such a way that the two ions are left in an entangled state at the end of the experimental sequence.

### 7.2.3 Quantum Networking

One of the biggest goals in quantum information science is the transfer of quantum information from a stationary qbit, for example an ion in a trap, to a traveling qbit, for example a photon, and vice versa. This would allow to build quantum networks. An ion trap with a cavity can

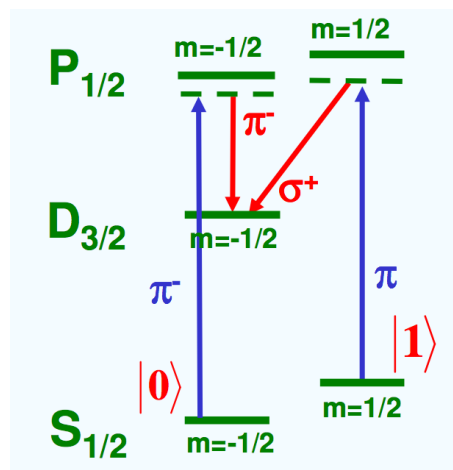


Figure 7.4: A scheme for mapping an ion's qbit state onto a photon

serve as an ion-photon interface. A scheme for mapping the quantum state of the ion is shown in figure 7.4. The Zeeman substates of the ground state are chosen as the qbit states  $|0\rangle$  and  $|1\rangle$ . Different polarisations of the pump pulse ( $\pi^-$ ,  $\pi$ ) address transitions to different Zeeman

---

substates and produce a photon with different polarisation during the cavity assisted Raman transition. Thus, the qbit state information is transferred onto the photon's polarisation state. To expand the idea further one can now imagine extracting the photon and via one of the cavity mirrors, letting it travel to another ion trap, and reversing the process.

# Bibliography

- [1] H. J. Kimble, M. Dagenais, and L. Mandel. Photon antibunching in resonance fluorescence. *Phys. Rev. Lett.*, 39:691–695, Sep 1977. [1](#)
- [2] Wolfgang Paul. Electromagnetic traps for charged and neutral particles. *Rev. Mod. Phys.*, 62(3):531–540, Jul 1990. [1](#), [4](#)
- [3] J. D. Prestage, G. J. Dick, and L. Maleki. New ion trap for frequency standard applications. *Journal of Applied Physics*, 66(3):1013–1017, 1989. [4](#)
- [4] N.W. McLachlan. *Theory and Applications of Mathieu Functions*. Dover Publications Inc., 1965. [7](#)
- [5] Raymond E. March and Richard J. Hughes. *Quadrupole Storage Mass Spectrometry*. John Wiley & Sons, 1989. [7](#)
- [6] Pradip K. Ghosh. *Ion Traps (International Series of Monographs on Physics, 90)*. Oxford University Press, USA, 1996. [8](#), [11](#)
- [7] Gerhard Robert Guthöhrlein. *Einzelne Kalziumionen in einem optischen Resonator*. PhD thesis, Ludwig-Maximilians-Universität München, 2001. [9](#)
- [8] H.G. Dehmelt. Radiofrequency spectroscopy of stored ions i: Storage. In D.R. Bates and Immanuel Estermann, editors, *Advances in Atomic and Molecular Physics*, volume 3 of *Advances in Atomic and Molecular Physics*, pages 53 – 72. Academic Press, 1968. [12](#)
- [9] D. J. Berkeland, J. D. Miller, J. C. Bergquist, W. M. Itano, and D. J. Wineland. Minimization of ion micromotion in a paul trap. *Journal of Applied Physics*, 83(10):5025–5033, 1998. [13](#)
- [10] N. Yu and W. Nagourney. Analysis of paul - straubel trap and its variations. *Journal of Applied Physics*, 77(8):3623–3630, 1995. [14](#)

- 
- [11] R. Alheit, S. Kleineidam, F. Vedel, M. Vedel, and G. Werth. Higher order non-linear resonances in a paul trap. *International Journal of Mass Spectrometry and Ion Processes*, 154(3):155 – 169, 1996. [14](#)
- [12] Matthias Keller. *Quantenoptik mit gespeicherten  $40\text{Ca}^{+}$ -Ionen*. PhD thesis, Ludwig-Maximilians-Universität München, 2004. [14](#), [15](#), [53](#), [92](#)
- [13] H.G. Dehmelt. Radiofrequency spectroscopy of stored ions ii: Spectroscopy. In D.R. Bates and Immanuel Estermann, editors, x, volume 5 of *Advances in Atomic and Molecular Physics*, pages 109 – 154. Academic Press, 1969. [16](#)
- [14] M H Holzscheiter. Cooling of particles stored in electromagnetic traps. *Physica Scripta*, 1988(T22):73, 1988. [16](#)
- [15] N Beverini, V Lagomarsino, G Manuzio, F Scuri, G Testera, and G Torelli. Experimental verification of stochastic cooling in a penning trap. *Physica Scripta*, 1988(T22):238, 1988. [16](#)
- [16] A Alili, J Andr, and F Vedel. Buffer gas cooling of ions stored in an r.f. trap: Computed properties of the ionic cloud. *Physica Scripta*, 1988(T22):325, 1988. [16](#)
- [17] D. J. Larson, J. C. Bergquist, J. J. Bollinger, Wayne M. Itano, and D. J. Wineland. Sympathetic cooling of trapped ions: A laser-cooled two-species nonneutral ion plasma. *Phys. Rev. Lett.*, 57(1):70–73, Jul 1986. [16](#)
- [18] D. J. Wineland, J. Dalibard, and C. Cohen-Tannoudji. Sisyphus cooling of a bound atom. *J. Opt. Soc. Am. B*, 9(1):32–42, Jan 1992. [16](#)
- [19] T.W. Hänsch and A.L. Schawlow. Cooling of gases by laser radiation. *Optics Communications*, 13(1):68 – 69, 1975. [16](#)
- [20] D. J. Wineland and H. Dehmelt. Proposed  $10^{14} \delta\nu < \nu$  laser fluorescence spectroscopy on  $\text{Ti}^{+}$  mono-ion oscillator (III). *Bull. Am. Phys. Soc.*, 20:637, 1975. [16](#)
- [21] D. J. Wineland, R. E. Drullinger, and F. L. Walls. Radiation-pressure cooling of bound resonant absorbers. *Phys. Rev. Lett.*, 40(25):1639–1642, Jun 1978. [16](#)
- [22] W. Neuhauser, M. Hohenstatt, P. Toschek, and H. Dehmelt. Optical-sideband cooling of visible atom cloud confined in parabolic well. *Phys. Rev. Lett.*, 41(4):233–236, Jul 1978. [16](#)

- 
- [23] John Weiner and P.-T. Ho. *Light-Matter Interaction, Fundamentals and Applications (Volume 1)*. Wiley-VCH, 2003. [18](#)
- [24] W. Phillips. Fundamental systems in quantum optics. *Les Houches, Session LIII, 1990*. [24](#)
- [25] D. M. Lucas, A. Ramos, J. P. Home, M. J. McDonnell, S. Nakayama, J.-P. Stacey, S. C. Webster, D. N. Stacey, and A. M. Steane. Isotope-selective photoionization for calcium ion trapping. *Phys. Rev. A*, 69:012711, Jan 2004. [27](#)
- [26] Nicolas Seymour-Smith, Peter Blythe, Matthias Keller, and Wolfgang Lange. Fast scanning cavity offset lock for laser frequency drift stabilization. *Review of Scientific Instruments*, 81(7):075109, 2010. [29](#)
- [27] C. J. Hawthorn, K. P. Weber, and R. E. Scholten. Littrow configuration tunable external cavity diode laser with fixed direction output beam. *Review of Scientific Instruments*, 72(12):4477–4479, 2001. [29](#)
- [28] M. Keller, B. Lange, K. Hayasaka, W. Lange, and H. Walther. Deterministic coupling of single ions to an optical cavity. *Applied Physics B: Lasers and Optics*, 76:125–128, 2003. [10.1007/s00340-003-1114-x](#). [34](#), [113](#)
- [29] G R Guthöhrlein, M Keller, K Hayasaka, W Lange, and H Walther. A single ion as a nanoscopic probe of an optical field. *Nature*, 414(6859):49–51, 2001. [34](#), [113](#)
- [30] M. A. Rowe, A. Ben-Kish, B. Demarco, D. Leibfried, V. Meyer, J. Beall, J. Britton, J. Hughes, W. M. Itano, B. Jelenkovic, C. Langer, T. Rosenband, and D. J. Wineland. Transport of quantum states and separation of ions in a dual rf ion trap. *Quantum Inform. Comput.*, 2(257), 2002. [35](#)
- [31] Johannes Schindler. *Characterization of an Erbium Atomic Beam*. PhD thesis, University of Innsbruck, 2011. [40](#)
- [32] M Harlander, M Brownnutt, W Hnsel, and R Blatt. Trapped-ion probing of light-induced charging effects on dielectrics. *New Journal of Physics*, 12(9):093035, 2010. [56](#)
- [33] R. C. Hilborn. Einstein coefficients, cross sections, f values, dipole moments, and all that. *Am. J. Phys.*, 50, 1982. [60](#)
- [34] A. L. Wolf, S. A. van den Berg, C. Gohle, E. J. Salumbides, W. Ubachs, and K. S. E. Eikema. Frequency metrology on the  $4s [^2S_{1/2}] - 4p [^2P_{1/2}]$  transition

- in  $^{40}\text{Ca}^+$  for a comparison with quasar data. *Physical Review A (Atomic, Molecular, and Optical Physics)*, 78(3):032511, 2008. [65](#)
- [35] Q. A. Turchette, Kielpinski, B. E. King, D. Leibfried, D. M. Meekhof, C. J. Myatt, M. A. Rowe, C. A. Sackett, C. S. Wood, W. M. Itano, C. Monroe, and D. J. Wineland. Heating of trapped ions from the quantum ground state. *Phys. Rev. A*, 61(6):063418, May 2000. [70](#), [82](#)
- [36] L. Deslauriers, S. Olmschenk, D. Stick, W. K. Hensinger, J. Sterk, and C. Monroe. Scaling and suppression of anomalous heating in ion traps. *Phys. Rev. Lett.*, 97(10):103007, Sep 2006. [70](#)
- [37] U G Poschinger, G Huber, F Ziesel, M Dei, M Hettrich, S A Schulz, K Singer, G Poulsen, M Drewsen, R J Hendricks, and F Schmidt-Kaler. Coherent manipulation of a  $^{40}\text{Ca}^+$  spin qubit in a micro ion trap. *Journal of Physics B: Atomic, Molecular and Optical Physics*, 42(15):154013, 2009. [70](#)
- [38] R. J. Epstein, S. Seidelin, D. Leibfried, J. H. Wesenberg, J. J. Bollinger, J. M. Amini, R. B. Blakestad, J. Britton, J. P. Home, W. M. Itano, J. D. Jost, E. Knill, C. Langer, R. Ozeri, N. Shiga, and D. J. Wineland. Simplified motional heating rate measurements of trapped ions. *Phys. Rev. A*, 76(3):033411, Sep 2007. [71](#), [72](#)
- [39] J. H. Wesenberg, R. J. Epstein, D. Leibfried, R. B. Blakestad, J. Britton, J. P. Home, W. M. Itano, J. D. Jost, E. Knill, C. Langer, R. Ozeri, S. Seidelin, and D. J. Wineland. Fluorescence during doppler cooling of a single trapped atom. *Phys. Rev. A*, 76(5):053416, Nov 2007. [72](#), [73](#), [78](#)
- [40] J. A. C. Weideman. Computation of the complex error function. *SIAM Journal on Numerical Analysis*, 31(5):pp. 1497–1518, 1994. [74](#)
- [41] J. M. Amini, J. Britton, D. Leibfried, and D. J. Wineland. *Micro-Fabricated Chip Traps for Ions*, pages 395–420. Wiley-VCH Verlag GmbH & Co. KGaA, 2011. [82](#)
- [42] N Daniilidis, S Narayanan, S A Mller, R Clark, T E Lee, P J Leek, A Wallraff, St Schulz, F Schmidt-Kaler, and H Hffner. Fabrication and heating rate study of microscopic surface electrode ion traps. *New Journal of Physics*, 13(1):013032, 2011. [82](#)
- [43] G. Janik, W. Nagourney, and H. Dehmelt. Doppler-free optical spectroscopy on the  $\text{Ba}^+$  mono-ion oscillator. *J. Opt. Soc. Am. B*, 2(8):1251–1257, Aug 1985. [84](#)

- 
- [44] R. M. Whitley and C. R. Stroud. Double optical resonance. *Phys. Rev. A*, 14:1498–1513, Oct 1976. [85](#)
- [45] C. K. Law and H. J. Kimble. Deterministic generation of a bit-stream of single-photon pulses. *Journal of Modern Optics*, 44(11-12):2067–2074, 1997. [91](#)
- [46] E.T. Jaynes and F.W. Cummings. Comparison of quantum and semiclassical radiation theories with application to the beam maser. *Proceedings of the IEEE*, 51(1):89 – 109, jan. 1963. [92](#)
- [47] Axel Kuhn, Markus Hennrich, and Gerhard Rempe. *Strongly Coupled AtomCavity Systems*, pages 223–236. Wiley-VCH Verlag GmbH Co. KGaA, 2005. [92](#), [93](#), [94](#)
- [48] J. S. Bell. *Speakable and Unspeakable in Quantum Mechanics: Collected Papers on Quantum Philosophy*. Cambridge University Press, 2004. [96](#)
- [49] Bernard D'espagnat. *Veiled Reality: An Analysis of Present-Day Quantum Mechanical Concepts*. Westview Press, 2003. [96](#)
- [50] Heping Zeng and Fucheng Lin. Quantum conversion between the cavity fields and the center-of-mass motion of ions in a quantized trap. *Phys. Rev. A*, 50:R3589–R3592, Nov 1994. [96](#)
- [51] David P. DiVincenzo. Quantum computation. *Science*, 270(5234):255–261, 1995. [96](#)
- [52] Asher Peres. *Quantum Theory: Concepts and Methods (Fundamental Theories of Physics)*. Springer, 1995. [96](#)
- [53] T. Pellizzari, S. A. Gardiner, J. I. Cirac, and P. Zoller. Decoherence, continuous observation, and quantum computing: A cavity qed model. *Phys. Rev. Lett.*, 75:3788–3791, Nov 1995. [96](#), [116](#)
- [54] Almut Beige, Daniel Braun, Ben Tregenna, and Peter L. Knight. Quantum computing using dissipation to remain in a decoherence-free subspace. *Phys. Rev. Lett.*, 85:1762–1765, Aug 2000. [96](#)
- [55] S. J. van Enk, H. J. Kimble, J. I. Cirac, and P. Zoller. Quantum communication with dark photons. *Phys. Rev. A*, 59:2659–2664, Apr 1999. [96](#)
- [56] J. I. Cirac, P. Zoller, H. J. Kimble, and H. Mabuchi. Quantum state transfer and entanglement distribution among distant nodes in a quantum network. *Phys. Rev. Lett.*, 78:3221–3224, Apr 1997. [96](#), [113](#)

- 
- [57] S. Bose, P. L. Knight, M. B. Plenio, and V. Vedral. Proposal for teleportation of an atomic state via cavity decay. *Phys. Rev. Lett.*, 83:5158–5161, Dec 1999. [96](#)
- [58] Anthony E. Siegman. *Lasers*. University Science Books, 1986. [98](#)
- [59] R. W. P. Drever, J. L. Hall, F. V. Kowalski, J. Hough, G. M. Ford, A. J. Munley, and H. Ward. Laser phase and frequency stabilization using an optical resonator. *Applied Physics B: Lasers and Optics*, 31:97–105, 1983. [10.1007/BF00702605](#). [100](#)
- [60] Eric D. Black. An introduction to pound–drever–hall laser frequency stabilization. *American Journal of Physics*, 69(1):79–87, 2001. [102](#)
- [61] R. J. Thompson, G. Rempe, and H. J. Kimble. Observation of normal-mode splitting for an atom in an optical cavity. *Phys. Rev. Lett.*, 68:1132–1135, Feb 1992. [113](#)
- [62] H.C. Ngerl, W. Bechter, J. Eschner, F. Schmidt-Kaler, and R. Blatt. Ion strings for quantum gates. *Applied Physics B*, 66:603–608, 1998. [113](#)
- [63] A.B. Mundt, A. Kreuter, C. Russo, C. Becher, D. Leibfried, J. Eschner, F. Schmidt-Kaler, and R. Blatt. Coherent coupling of a single  $40\text{Ca}^+$  ion to a high-finesse optical cavity. *Applied Physics B*, 76:117–124, 2003. [113](#)
- [64] Matthias Keller, Birgit Lange, Kazuhiro Hayasaka, Wolfgang Lange, and Herbert Walther. Continuous generation of single photons with controlled waveform in an ion-trap cavity system. *Nature*, 432:1075–1078, 2004. [113](#)
- [65] M. Keller, B. Lange, K. Hayasaka, W. Lange, and H. Walther. Long-term stability of continuous-wave emission from an ion-cavity system. *The European Physical Journal D - Atomic, Molecular, Optical and Plasma Physics*, 32:161–166, 2005. [113](#)
- [66] C. Russo, H.G. Barros, A. Stute, F. Dubin, E.S. Phillips, T. Monz, T.E. Northup, C. Becher, T. Salzburger, H. Ritsch, P.O. Schmidt, and R. Blatt. Raman spectroscopy of a single ion coupled to a high-finesse cavity. *Applied Physics B*, 95:205–212, 2009. [113](#)
- [67] Matthias Steiner, Hendrik M. Meyer, Christian Deutsch, Jakob Reichel, and Michael Köhl. Single ion coupled to an optical fiber cavity. *Phys. Rev. Lett.*, 110:043003, Jan 2013. [114](#)